

Numerical simulation and experimental validation of biofilm formation

Von der Fakultät für Maschinenbau
der Gottfried Wilhelm Leibniz Universität Hannover

zur Erlangung des akademischen Grades
Doktor-Ingenieur

genehmigte Dissertation
von

M. Sc. Meisam Soleimani

geboren am 31.12.1984 in Bojnord, Iran

Herausgeber:

Prof. Dr.-Ing. habil. Dr. h.c. mult. Dr.-Ing. E.h. Peter Wriggers

Verwaltung:

Institut für Kontinuumsmechanik
Gottfried Wilhelm Leibniz Universität Hannover
Appelstraße 11
30167 Hannover

Tel: +49 511 762 3220
Fax: +49 511 762 5496
Web: www.ikm.uni-hannover.de

© M. Sc. Meisam Soleimani
Institut für Kontinuumsmechanik
Gottfried Wilhelm Leibniz Universität Hannover
Appelstraße 11
30167 Hannover

Alle Rechte, insbesondere das der Übersetzung in fremde Sprachen, vorbehalten. Ohne Genehmigung des Autors ist es nicht gestattet, dieses Heft ganz oder teilweise auf photomechanischem, elektronischem oder sonstigem Wege zu vervielfältigen.

ISBN 978-3-941302-20-4

1. Referent: Prof. Dr.-Ing. habil. Dr. h.c. mult. Dr.-Ing. E.h. Peter Wriggers
2. Referent: Prof. Dr. Meike Stiesch

Tag der Promotion: 31.01.2017

To my dear wife and parents

Zusammenfassung

Im Rahmen dieser Dissertation wurde ein 3D-Simulationsmodell entwickelt um Biofilme in einem Multi-Physik-Framework durch Smoothed Particle Hydrodynamics (SPH) in einem Kontinuumsansatz zu untersuchen. Biofilme an sich sind Ansammlungen von Mikroorganismen, wie beispielsweise Bakterien. Die Bildung eines Biofilms ist ein komplexer Prozess, da mehrere physikalische Phänomene miteinander in Verbindung stehen, welche auf unterschiedlichen Zeitskalen stattfinden. Einerseits wird das Wachstum von Biofilmen durch biologische Reaktionen sowie Stoffdiffusion vorangetrieben. Andererseits wird der Biofilm durch Fluidströmungen deformiert und an der Grenzschicht finden Erosionsvorgänge statt. Letztere stellen eine Fluid-Struktur-Interaktion (FSI) mit einer deformierbaren Struktur dar. Die geometrische und numerische Komplexität, die aus diesen Phänomenen hervorgeht birgt schwerwiegende numerische Komplikationen und Herausforderungen bei der Lösung mit netzbasierten Verfahren wie den Finiten Volumen (FV) oder Finiten Elementen (FE). Solche Probleme werden im Allgemeinen als Netzverzerrung bezeichnet. In dieser Arbeit wird die Lösung auf Basis von SPH berechnet, einer aktuellen, netzfreien Methode. SPH-basierte Computermodellierung findet in der biologischen Anwendung bisher kaum Erwähnung, obwohl das Verfahren besonders robust bei der Erfassung von grenzschichtbezogenen Prozessen ist. Tatsache ist, dass SPH aufgrund ihrer adaptiven Lagrangeschen Beschreibung von Kontinua ein vielseitiges Werkzeug für Probleme ist, deren Geometrie dynamischen temporären Veränderungen unterliegt. Aufgrund seiner partikelbasierten Natur lassen sich auf einfache Art und Weise komplexe Interaktionen und Ad-hoc-Regeln zwischen den Partikeln implementieren. Dies ist der Fall für Probleme mit gekoppelten Gleichungen in unterschiedlichen Zeit- und Längenskalen. In dieser Arbeit werden alle verschiedenen physikalischen Phänomene, die eine Rolle bei der Bildung von Biofilmen spielen im Rahmen von SPH umgesetzt. Neben der numerischen Simulation wurden Experimente von unserem Partner an der Medizinischen Hochschule Hannover (MHH) durchgeführt. Die erhaltenen numerischen Ergebnisse zeigen gute Übereinstimmungen mit den experimentellen und veröffentlichten Daten. Dies zeigt, dass das Modell die räumliche und zeitliche Entwicklung von Biofilmen korrekt vorhersagen kann. Das entwickelte Modell kann dazu genutzt werden schädliche Biofilme zu kontrollieren sowie gewünschte Biofilme besser nutzbar zu machen.

Schlagworte: Biofilm, Multiphysics, Smoothed Particle Hydrodynamics, Fluid-Solid Interaktion

Abstract

In this dissertation, a state-of-the-art 3D computational model has been developed to investigate biofilms in a multi-physics framework using smoothed particle hydrodynamics (SPH) based on a continuum approach. Biofilms are in fact aggregation of microorganisms such as bacteria. Biofilm formation is a complex process in the sense that several physical phenomena are coupled and consequently different time-scales are involved. On one hand, biofilm growth is driven by biological reaction and nutrient diffusion and on the other hand, it is influenced by the fluid flow causing biofilm deformation and interface erosion in the context of fluid and deformable solid interaction (FSI). The geometrical and numerical complexity arising from these phenomena poses serious complications and challenges in grid-based techniques such as finite element (FE). Such issues are generally referred to as mesh distortion. Here the solution is based on SPH as one of the powerful meshless methods. SPH based computational modeling is quite new in the biological community and the method is uniquely robust in capturing the interface-related processes of biofilm formation especially erosion. The fact is that SPH is a versatile tool owing to its adaptive Lagrangian nature in the problems whose geometry is temporarily dynamic. Moreover, its mesh-less feature is considered to be favorable in interpreting the method as a particle based one. Hence, it is quite straight forward to incorporate complex interactions and ad-hoc rules at the particle level into the method. This is the case for the problems with coupled governing equations with different time and length scale. In this thesis all different physics which account for biofilm formation have been implemented in the framework of SPH and one can say that this tool is purely SPH based. Besides the numerical simulation, experiments were conducted by our partners in the medical school of Hannover. The obtained numerical results show a good agreement with experimental and published data which demonstrates that the model is capable of predicting overall spatial and temporal evolution of the biofilms. The developed tool can be employed in either controlling the detrimental biofilms or harnessing the beneficial ones.

Keywords: Biofilm, Multi-Physics, Smoothed Particle Hydrodynamics, Fluid-Solid Interaction

Acknowledgements

I owe my gratitude to numerous people without whose support I could never complete my PhD. First and foremost, I should express my appreciation and thanks to the distinguished professor Dr.-Ing. habil. Dr. h.c. mult. Dr.-Ing. E.h. Peter Wriggers. I am really privileged to work under his supervision. I have benefited from his deep insight and endless knowledge in computational mechanics not only in my meetings with him but also in the institute seminars where he gave his constructive comments to others. Furthermore, I should admit that I never felt stressed at Institute of Continuum Mechanics (IKM) during my PhD thanks to his fatherly attitude since the first day I met him. Second, my thanks goes to Professor Stiesch as my co-supervisor and also Henryke as my partner in the medical school of Hanover (MHH). They were very supportive and collaborative in the experimental part of my project. Third, I should appreciate my international colleagues at IKM and also Iranian friends whose names I can not write down one-by-one. However I was especially inspired by six of them with lots of creative ideas through helpful discussions with them. Thank you Dr. Löhnert, Dr. Avci, Dr. Weißenfels, Jan-Philipp, Shahab and Hamid. Forth, I can not forget the assistance of IKM technical and administrative staffs especially Jens who helped me patiently with computer related problems some of which were weird. Furthermore, I should name Frau Halfar and Dorit who handled the administrative works at IKM. Fifth, I acknowledge the financial support of my PhD project by the ministry of culture and science of the Niedersachsen in the context of MARIO program. Sixth, I am so grateful to my parents who prayed for me all days and nights. They raised me and taught me and I have always been backed by them. Furthermore, I am thankful to Hassan and Reza, my brothers-in-law who have cheered me and my wife up by their kindness. We have always felt confident by their presence and support in Germany. Seventh, I extend my deepest respect to Dr. Ghahary, my father-in-law, and also Dr. Reihani who are of the most influential mentors in my life. They have provided us with precious lessons. Lastly and the most importantly, I should mention my wife, Rana who deserves the outermost appreciation for her understanding, continuous love and trust in me. She dedicatedly endured my countless working hours in weekends and late nights and encouraged me in both happy and gloomy days.

Hannover, September 2016

Meisam Soleimani

Contents

1	Introduction	1
1.1	Motivation	1
1.2	What are biofilms?	2
1.3	Background and state of the art	4
1.4	Structure of this work	7
2	Mathematical framework and governing equations	9
2.1	Spatial domain and geometry	10
2.2	Overview of the physical processes and the fundamental assumptions	11
2.3	Theory of the volumetric growth for biological tissues	12
2.3.1	Kinematics of growth	13
2.4	On the hypo-elastic approach in solid mechanics	18
2.4.1	Historical background	18
2.4.2	Mathematical framework of hypo-elasticity	18
2.5	Governing equations	20
2.5.1	Mass balance (continuity)	21
2.5.2	Diffusion-advection-reaction	21
2.5.3	Momentum balance	22
2.5.4	Constitutive equations	23
2.5.5	Erosion (detachment)	24
3	Discretization and implementation	27
3.1	Numerical method	27
3.1.1	Eulerian and Lagrangian perspective	27
3.1.2	Mesh-less and mesh based methods	28
3.1.3	SPH method	28
3.2	Discretization	36
3.2.1	Initial particles distribution (meshing)	36
3.2.2	Discretization of the mass balance (continuity) equation	38
3.2.3	Discretization of the momentum balance equation	39
3.2.4	Discretization of the diffusion-advection-reaction equation	39
3.2.5	Discretization of the constitutive equations	39
3.2.6	Particles coalescence and splitting (re-meshing)	40
3.3	Implementation	42
3.3.1	Boundary conditions and fluid-solid interaction implementation	42

3.3.2	Numerical challenges and remedies	49
3.3.3	Integration method	54
3.4	Solution procedure (pseudo-code)	55
3.5	Code optimization and parallelization	57
3.5.1	Neighbor search algorithm	57
3.5.2	OpenMP implementation	58
4	Numerical examples and results	61
4.1	Validation of the code	61
4.1.1	Test case 1: Elastic gate of a water tank	61
4.1.2	Test case 2: Rectangular biofilm deformation in fluid flow	64
4.2	Biofilm deformation and erosion	66
4.2.1	Deformation and erosion 2D	66
4.2.2	Deformation and erosion 3D	70
4.2.3	The impact of the fluid velocity on the erosion rate	73
4.3	Biofilm growth	75
4.3.1	Biofilm growth 2D	75
4.3.2	Biofilm growth 3D	78
5	Conclusions	81
	Bibliography	83
	CURRICULUM VITAE	94

Chapter 1

Introduction

1.1 Motivation

If you were born in 2500 BC and suffered from dental caries, you would definitely believe that the "teeth worm" caused some cavities in your teeth, see GERABEK (1999). If you had the chance to live in 350 BC where Aristotle lived, he might advise you not to eat too much sweets because he had found that the sweaty materials cause decay of teeth, see NEWBRUN (1982). It may be surprising to know that the mystery of dental caries was uncovered until 17th century where Antonie van Leeuwenhoek, a Dutch salesman who became later the father of microbiology, could observe for the first time the tiny living things in the oral cavity. They were swarming in the teeth surface had tenaciously anchored themselves to that. At that time he called them animalcules. Today we know that these microorganisms are in fact the bacteria which form biofilm, see PERCIVAL ET AL. (2011). Such bacteria exist in the oral cavity almost since the moment of passing through the birth. Hundreds of them live there and wait until the teeth erupt. As soon as they find the teeth, they colonize its surface and form a biofilm. If they have sufficient time and good environmental condition, they may convert to a dental plaque and finally contribute to dental caries. The early stages of biofilms formation are reversible, see ROSAN & LAMONT (2000). It means that they can be washed out by the external forces such as brushing and rinsing the teeth or even the natural flow of saliva. However, when they are matured, they turn into a heterogeneous material which adheres to the teeth and need for more serious treatment in order to be removed. The medical infections caused by the biofilms incur billions of dollars every year in the world, see WANG & ZHANG (2010).

The research on biofilms has been motivated by the aim of predicting their development in order to finally either hamper the formation of detrimental ones such as dental plaque or tailor the beneficial ones to employ them in the industrial applications such as water treatment units. It is known qualitatively that the biofilms strongly interact with their environment. Nevertheless researchers have endeavored to simulate their behavior quantitatively by means of mathematical and computational tools. In last three decades, a great deal of the literature has been dedicated to the biofilms modeling. The goal is to understand better the physics behind the biofilms and shed light on complex experimental results.

1.2 What are biofilms?

A simple definition of biofilms is "microorganisms attached to a surface". For a more precise and complete description, one can say that they are "a layer of prokaryotic and eukaryotic cells anchored to a substratum surface and embedded in an organic matrix of biological origin", see BOYLE (1991). Prokaryotes (bacteria and archaea) are estimated to encompass approximately half of the extant biomass in the universe in terms of the numbers. Each human hosts about 100 trillion microbes (bacteria and archaea), ten times more than human cells, see KLAPPER & DOCKERY (2010). It has been estimated that more than 99 percent of all bacteria on the earth live in the "slime city" (biofilm form), see COGHLAN (1996). The biological ground because of which the bacteria tend to grow in clustered populations instead of individually wandering, is that this type of living make them more resistant to the environmental and external threats and consequently increases the chance of survival for them. In fact, Biofilm is a form of life for the bacteria with which they can adjust their needs more easily to accommodate highly diverse environments, see PERCIVAL ET AL. (2011). Nonetheless, such a collective behavior does not necessarily mean altruism and there is always a conflict of interests between the fitness of the individual bacteria and the fitness of a group of them. It leads to a twofold interaction between the bacteria, namely cooperation and competition. This concept has been referred to in KREFT (2004). Such complicated interactions that exist merely among living beings make the simulation of them much more challenging in terms of mathematical modeling. In this work, the focus is mainly on the bacteria which cause biofilm formation in the oral cavity on the surface of the dental implants and teeth.

Biofilm development is a multi-stages process, see PALMER & WHITE (1997), O'TOOLE ET AL. (2000). At least four distinct stages have been identified:

1- Formation of conditioning film

The aqueous solid-fluid interface is coated by the chemical organic agents which are present in the fluid medium. In other words, the surface is conditioned and its chemical properties is prepared to be colonized by the planktonic bacteria. In addition to the chemical composition of the interface, the micro-topography of the surface is important. It has been proven that the more the roughness of a surface is, the more the bacterial adhesion occurs, see CHARACKLIS ET AL. (1999a). The reason is that the tiny crests and valleys at the surface play the role of shields for the attached bacteria and protect them from the fluid flow forces. Furthermore, the effective total area of the surface increases due to the surface roughness and it enhances the mass transport mechanisms, see CHARACKLIS ET AL. (1999b). Besides the surface roughness, the physicochemical characteristics of the surface such as its hydrophobicity, wettability, surface energy and polarity contribute to the attractive forces between the surface and the bacteria. It has been discovered that the surfaces made of hydrophobic and non-polar materials such as Teflon are colonized more quickly by the bacteria, see FLETCHER & LOEB (1979), PRINGLE & FLETCHER (1983). In the oral cavity, the platform of dental plaque is a salivary pellicle covering the tooth enamel surfaces. This comprises mainly of organic molecules such as proteins and is indeed an active conditioned interface which behaves like a receptor for the freely swimming *Streptococcus mutans*, a type of bacteria

in the mouth which is the major etiological agents in dental biofilm, see PALMER ET AL. (2007), DONLAN (2002).

2- Initial reversible attachment of the bacteria to the conditioned surface

It has been found that the initial attachment of the planktonic bacteria is driven by the Van der Waals and electrostatic forces which take place in length scales of order tens of nanometers. It is still a not truly understood phenomenon and rare computational modeling can be found in the literature. Nevertheless some researchers employed theories like DVLO (DerjaguinLandauVerweyOverbeek) incorporating Van der Waals and electrostatic forces to simulate initial adherence of bacteria, see MARSHALL ET AL. (1971), HERMANSSON (1999). This phase is considered to be reversible. It means that there is a weak bond between the bacteria and the surface and hence the bacteria can be removed by even soft rinsing. If repulsive forces are larger than the attractive forces, the bacteria will detach from the surface. This is more likely to happen especially in the case that the conditioning film is not formed completely, see GARRETT ET AL. (2008).

3- Irreversible adhesion and growth

The next stage is so-called irreversible adhesion in which an Extra Polymeric Substance (EPS) is produced by the bacteria and glue them together firmly, see DUNNE (2002). The structure of the microbial agents (bacteria) due to the presence of flagella in their bodies and also the amount and the composition of the EPS has a great impact on the strength of the developed biofilm. EPS may constitute 50 to 90 percent of the total biofilms, see FLEMMING ET AL. (2000). EPS is in fact the medium through which the bacteria not only absorb the diffused nutrient, but also communicate with each other. This intercellular communication is done via a released chemical material conveying a special signal. This mechanism is called "Quorum Sensing" which enables the bacteria to monitor the density in their neighborhoods and control the expression of genes accordingly, see WATERS & BASSLER (2005). The biofilm grows as a result of the EPS generation, bacteria division and growth of the individual bacteria. EPS influences strongly the physical material properties of the biofilm as a heterogeneous material. In this stage, the micro and meso-scale physical phenomena such as diffusion, advection, reaction and mechanical stress distribution become important and play a role in the growth process, see KLAPPER & DOCKERY (2010).

4- Detachment

once the biofilm matures, some parts of it may be detached due to several causes. Some times, external forces such as the induced shear from the surrounding fluid or external intervention lead to the rupture and detachment of the biofilm. In the case that there is a shortage of nutrient in a certain part of the biofilm, detachment is a survival mechanism by which the bacteria migrate with the hope of gaining more food somewhere else. In some cases, the root of detachment is in quorum sensing and in fact it is like a consensus among all bacteria in the biofilm in order to do gene expression. Regardless of the origin of detachment, it is an interfacial process which causes material transfer from the biofilm to the bulk fluid. The detached bacteria floated in the fluid can land on another point of the surface and reattach themselves to it. In such a case, they are like a seed for a new biofilm formation. In general

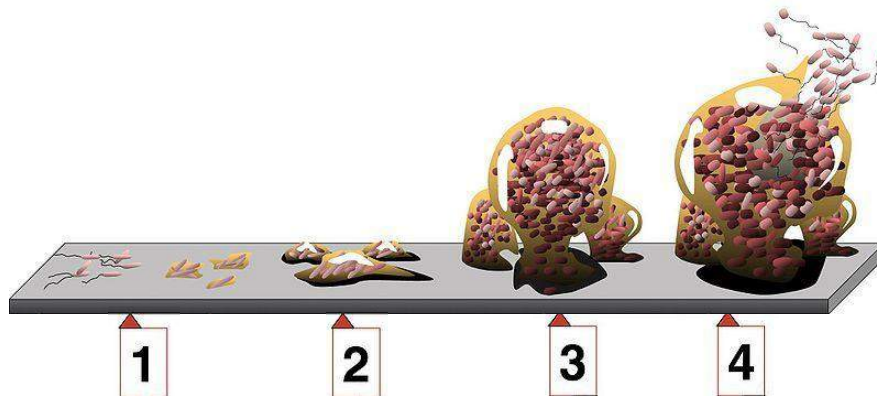


Figure 1.1. Different stages of the biofilm development (from www.boundless.com)

the detachment process takes place in parallel with growth process, see DONLAN (2002). Figure (1.1) illustrates the different stages of biofilm formation schematically.

1.3 Background and state of the art

Although a Biofilm can be simply described as the aggregation of microorganisms, its formation and evolution is quite complex in a mathematical framework due to the fact that it is governed by various physical phenomena. Indeed, the formation of biofilm is a multi-physic and multi scale problem, see WANG & ZHANG (2010). Aside from the experimental study of the biofilms that has an old history (since 17th century as mentioned before), early attempts to mathematically model the biofilms date back to the late 1970s and early 1980s, see WILLIAMSON & MCCARTY (1976), RITTMANN & MCCARTY (1982), WANNER & GUJER (1986). In these works, it was tried to develop a one dimensional system of partial differential equations describing the biofilm growth. Since then, a variety of methods have been proposed to model two and three dimensional biofilm, all of which fall into either continuum-based, see PICIOREANU ET AL. (1999), PICIOREANU ET AL. (2000), PICIOREANU ET AL. (2001a), ALPKVISTA & KLAPPER (2007), DILLON ET AL. (1996) or Hybrid discrete-continuous models that are known as Individual-based methods (IBM), see KREFT ET AL. (1998), KREFT ET AL. (2001), PICIOREANU ET AL. (2004a). There are also some Cellular Automaton (CA) models which are conceptually more or less similar to the IBM in this sense that the overall behavior and spatial structure of the biofilm come out of the biological interactions taking place at the individual level between discrete agents, see TANG & VALOCCHI (2013), PICIOREANU ET AL. (1998), PIZARRO ET AL. (2001), NOGUERA ET AL. (1999). In spite of being simple, such agent based models are capable of reproducing quite complex morphologies such as finger-like and fractal shapes of biofilm in case that biofilm growth is governed by the diffusion-limited aggregation (DLA) models in which the nutrient diffusion is the dominant process, see FUJIKAWA & MATSUSHITA (1989).

It might be noteworthy to mention that agent based methods are more appealing to the biologists because of their inherent simplicity and capacity to incorporate new local ad-hoc rules being inspired from biology such as bacterial binary division, attachment and detachment

of the bacteria. Furthermore, handling multi species biofilm is not a big deal by defining local interactions between different type of agents, see PICIOREANU ET AL. (2004b). Nevertheless drawbacks of these methods are the introduced stochastic effects and geometrical anisotropy due to the arbitrariness of the local rules which make the results less physical. So many parameters challenge predictiveness of such models. Non-trivial error estimation and more aesthetically driven results oppose mathematical and physical predictions, see EBERL ET AL. (2001).

Recalling the different stages of the biofilm development, it should be expressed that there are overwhelming references in the literature in which the third and fourth step of the biofilm formation (growth and detachment) have been computationally tackled, whereas very rare (in fact no) robust computational work can be found relevant to the first and second stages (conditioning film and initial colonization). The reason is that their underlying physics lies in two different frameworks. The first and second stages are phenomena which take place in nano scale, while the third and fourth one are in micro and meso scale. The mathematical framework of the former is at molecular level, while that of the latter is continuum mechanics. From now on, it is assumed that the initial attachment of the biofilm is a priori and we do not discuss it anymore. In practice, the early data collected from the experiment after a very short exposure time (about an hour or less), see FLETCHER & LOEB (1979) and PRINGLE & FLETCHER (1983), can be regarded as the initial condition of the biofilm for numerical simulation. In this thesis the focus is on the third and the fourth stage of biofilm development, namely growth and mechanical response of the biofilm (deformation and detachment) in a continuum-based approach.

To discuss more effectively what has been done with regard to biofilm simulation in the literature, the physics behind the process needs to be deeply understood. This helps us to know the well investigated aspects and also lesser studied ones. Biofilm computational models are based on three principal concepts. First, transport mechanisms (diffusion-advection) which bring nutrients to the biofilm. second, biological consumption and consequently growth mechanisms which directly contribute to the biofilm structural form. Third, biofilm-fluid interface related mechanisms that account for the effect of the surrounding fluid on the biofilm in terms of deformation and detachment.

The first mechanism has been well developed in a continuum-based frame work in all existing previously mentioned references.

The second mechanism is exactly the point where the two different approaches, i.e Individual based and continuum based methods, branch. The main idea of the agent based methods for growth is that discrete elements mimicking bacteria grow and afterward a contact model handles the overlaps between the agents and results in an overall expansion of the system. It is called "shoving mechanism". The most recent open source simulator for biofilms using such individual based methods is called iDynoMiCS (Individual based Dynamics of Microbial communities Simulator) developed in Java language, see LARDON ET AL. (2011). When it comes to a continuum framework for the biofilm growth, almost all researchers assume the biofilm to behaves like a viscous fluid with a mass source term, see CUMSILLE ET AL. (2014), DOCKERY & KLAPPER (2001), COGAN (2007). This assumption is reasonable, although the biofilm is apparently a solid-like material. The fact is that the characteristic time scale of the biofilm growth is so larger than its relaxation time scale. Hence, in practice

no residual stresses remains inside the biofilm after the growth and it is fully relaxed like a viscous fluid, see JONES & CHAPMAN (2012). It should be noted that the residual stresses are generally an inevitable resultant of biological soft tissues growth, if they are assumed to behave like a viscoelastic solid. This has been extensively studied by the researchers in a robust continuum framework, see KROON ET AL. (2008), KUHL & HOLZAPFEL (2007), AMBROSI ET AL. (2011), TABER (1998).

The third and the least understood mechanism is the one occurring at the interface of the fluid and biofilm. The fluid flow exerts forces to the biofilm and erodes or sloughs it which change its architecture significantly. This process is of great importance, since it contributes to the biofilm development in an opposite way in comparison to the biological growth. Thus, it results in the material removal and in some cases a final balance between detachment and growth process is reached. It can keep the overall biofilm architecture more or less constant, see HORN ET AL. (2003). Although the induced stresses and deformation and even triggered small vibrations in the biofilm are not an important factor in its shape, it is necessary to do a stress analysis embedded in a fluid-structure interaction (FSI) analysis in order to correctly capture the failure and detachment process in the biofilm, see PICIOREANU ET AL. (2001b), DUDDU ET AL. (2009). Furthermore, the effect of the detached material forming streamers and also its oscillation characteristics, have been taken into account by some researchers, see STOODLEY ET AL. (1998), STOODLEY ET AL. (1999), TAHERZADEH ET AL. (2010). In EBERL ET AL. (2000) it was argued that the movement of a flexible streamer contributes to an increase in mass transfer of the nutrient from the bulk liquid to the biofilm. The biofilm response to the external forces has been modeled using FEM in conjunction with a fluid flow solver in BÖL ET AL. (2009). In this reference, the geometrical profile of the biofilm is reconstructed from the stacks of Confocal Laser Scanning Microscopy (CLSM) and the stress analysis is done using an FEM software incorporating detachment via the deletion of elements. However, some researchers have preferred to use particle based methods such as discrete breakable spring-damper elements to simulate the biofilm interaction with the fluid flow, see ALPKVIST & KLAPPER (2007), and also Dissipative Particle Dynamics (DPD) as a Lagrangian stochastic approach, see XU ET AL. (2011). Besides these approaches, some models are relied on empirical or semi analytical "detachment functions" inspired from the 1D biofilm modeling in which the detachment rate is proportional to h^2 where h is the local biofilm thickness. Of course, this method introduces some unknown parameters that need to be identified for each problem, see XAVIER ET AL. (2005). It is noteworthy to know that in iDynoMiCS, the fluid flow is not resolved and a constant boundary layer for the nutrient diffusion in the fluid along with such detachment functions has been implemented, instead LARDON ET AL. (2011).

Regardless of the method, the presence of moving and varying boundaries in biofilm-fluid interface and how to handle it, is a complex task, especially in 3D in grid based schemes. It needs to be dealt with in an accurate and efficient way. In DUDDU ET AL. (2008) this issue has been addressed using a level set method in the Extended Finite Element framework (XFEM).

The aim of this work is to develop and present a unified computational approach for the biofilm formation modeling based fully on the Smoothed Particle Hydrodynamic (SPH) method. SPH was firstly introduced in GINGOLD & MONAGHAN (1977) and LUCY (1977)

for astrophysical applications and nowadays has been applied to simulate several physical processes such as diffusion-advection, see CLEARY & MONAGHAN (1999), ZHU & FOX (2001), ARISTODEMO ET AL. (2010), fluid flow, see MONAGHAN (1994) GOMEZ-GESTEIRA ET AL. (2010), hydraulic terrain erosion, see KRIŠTOF ET AL. (2009), reactive transport and precipitation, see TARTAKOVSKY ET AL. (2007), solid deformation, see GRAY (2001), LIBERSKY ET AL. (1993) and FSI analysis, see ANTOCI ET AL. (2007). Although most of these processes are conceptually involved in the biofilm formation, to the best of author's literature surveying, this work is the first one in which the biofilm formation as a multi-physics phenomenon has been modeled using a fully SPH based method.

1.4 Structure of this work

This work contains three main more chapters as follows: In the second chapter, first the basic assumptions behind the mathematical modeling of the physical phenomena behind the biofilm formation are explained. Then, the two concepts of "hypo-elasticity" and "continuum growth theory" are elaborated in more details, since they are the foundations of this work and also lesser-known in comparison to solid deformation using a hyper-elastic approach. For the sake of conciseness and avoiding redundancy, the basic principals of the continuum mechanics and non-practical equations are assumed to be known and hence are not repeated. Instead, the practical governing equations are presented and the readers have been referred to numerous good available textbooks for more details. The third chapter starts with a brief review of the SPH method. In the remainder of this chapter, the SPH method is applied to the governing equations derived in the former chapter in order to discretize them. Moreover, the numerical implementation, solution procedure, numerical difficulties and the associated remedies are discussed in detail. Additionally, an error estimation analysis of the SPH method is presented in this chapter. In the fourth chapter, first some benchmark numerical examples are provided in order to validate the numerical developed code. Then, further 2D and 3D exemplary cases are simulated for the biofilm growth, biofilm deformation and erosion. The achieved results are compared with those of experiments conducted by our partners in the medical school of Hanover and also available data in the literature. At the end, we conclude the dissertation in the fifth chapter with the outcomes of this work. Besides, the possible extensions for the future researches are suggested.

Chapter 2

Mathematical framework and governing equations

In this chapter, first the geometrical description of the problem is presented. Then the underlying physical processes are discussed along with the associated assumptions. Before we proceed with the governing equations, an introductory section is dedicated to the "mechanics of volumetric growth". The reason is that its mathematical framework is rather a new concept in continuum mechanics and not every body is familiar with. Furthermore, hypo-elasticity that is the basis for solid deformation in this work is discussed thoroughly in the following section, because rarely is the hypo-elastic approach used in standard and well-known computational methods such as FEM. To avoid redundancy, no further details on kinematic of deformation and fundamental laws of thermodynamics in continuum mechanics is provided. The readers may refer to several available good books on that, e.g. see HOLZAPFEL (2000). Instead, the final and practical balance equations are taken and the computational aspects of the governing equations based on SPH are more elaborated on.



Figure 2.1. Experimental set-up, Medical school of Hanover (MHH) by Henryke Rath

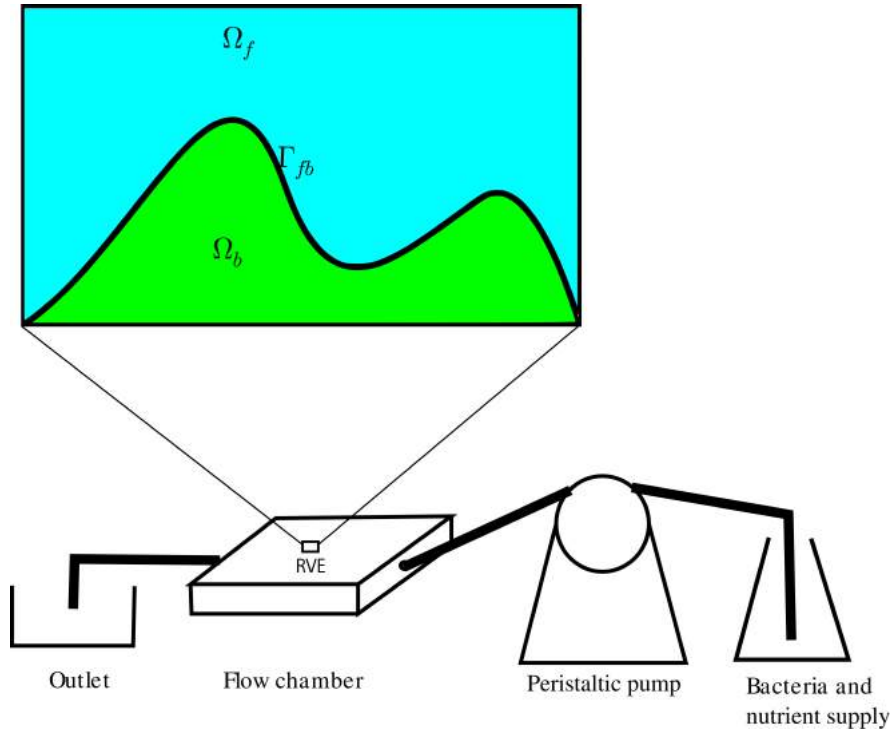


Figure 2.2. Schematics of the experimental set up and sub-domains of the RVE

2.1 Spatial domain and geometry

In this study, The numerical results for the biofilm growth are validated by the experimental data. The main part of the experimental set-up conducted by our colleagues of the medical school is a flow chamber which is fed with a peristaltic pump. At the center of it, there is a Titan plate where the biofilm can form on. The size of the titan plate is $12mm \times 12mm$, see figure (2.1). Due to the computational costs of resolving the full macro scale, the simulation is limited to several tens micron in each spatial direction. This small region can be considered as a Representative Volume Element (RVE) at micro-scale. In practice, the modeled domain is expected to be equal to the zooming area where the experimental data are gathered using Scanning Electron Microscopy (SEM). Figure (2.2) illustrates a schematic view of the whole experimental set-up and also the RVE.

The spatial whole domain in the RVE is divided into two subdomains (compartments) i.e the fluid compartment Ω_f and biofilm compartment Ω_b . The interface between these two Γ_{fb} is the surface where the field variables are coupled. Unknown field variables in Ω_f are the velocity and nutrient concentration and in Ω_b are the advective movement which determines the biofilm geometrical profile due to the growth phenomena and the nutrient concentration. These unknown field variables must be computed using mathematical governing equations in conjunction with appropriate boundary conditions. In the next section, the physical processes and principal assumptions behind the mathematical modeling is explained.

2.2 Overview of the physical processes and the fundamental assumptions

In order to establish an appropriate model for the biofilm development, we need to understand the physics behind it and be fully aware of the associated assumptions. The growth of the biofilm is a biological-mechanical process in which there is a continuous mass generation. This mass expands and leads to biofilm growth. Due to this fact that the overall mass in the whole RVE must conserve, the newly produced biomass is nothing else than the consumed mass which has been dissolved in the fluid (nutrient). The transformation of mass from the nutrient from into living biomass is performed by the bacteria (biofilm) via the growth process. The new configuration of the biofilm results in new interface Γ_{fb} and it creates new geometrical boundary conditions for the fluid. It affects not only the velocity field but also the concentration of the nutrient. Furthermore, the fluid flow has a dual effect on the biofilm. From one hand it provides the biofilm with the nutrient (a positive role in feeding the bacteria) and on the other hand, it applies shear forces on the biofilm and deform it. If the induced stress are sufficiently large, some parts of the biofilm may be removed by the flow (a negative role in destroying the biofilm). So we face a coupled multi-physics problem which encompasses fluid flow, diffusion-reaction-advection, mechanical deformation, growth and erosion. At the first glance, the problem is so complicated and different physical processes are so interwoven that it seems to be unsolvable. However, a closer and deeper look at it, reveals that we have a clear separation of time scales associated to different processes, see PICIOREANU ET AL. (2000), HAUSER & VAFAI (2013). Figure (2.3) shows the typical ranges of characteristic times for processes that take place in a biofilm system. An order of magnitude argument for the time scales helps us to realize that the biofilm behavior is narrowed down to the time period of modeling we are interested in. In other words, depending on the temporal size of "observation window" some physical process might be excluded from the modeling. This leads to the assumption that all fast processes (the ones with smaller time scale) such as fluid flow and nutrient diffusion reach their steady state (temporally homogenized) value when a slower process (the ones with large time scale) such as biofilm growth is taking place. In fact it is the main idea of temporal homogenization YU & FISH (2002) and consequently different processes could be solved efficiently in a staggered and nested manner without scarifying the "accuracy". The key assumptions for the modeling of the biofilm in this work are as follows:

1- In this work the focus is on the dental biofilms. Although it has been found more than 500 different species of bacteria in human oral cavity, the one which mainly contributes to the dental biofilm (plaque), is a bacterium called "Streptococcus mutans", see KOLENBRANDER (2000). There is a straight forward framework for multispecies modeling in the literature, see WANNER & GUJER (1986), PICIOREANU ET AL. (2004a), XAVIER ET AL. (2005). Nevertheless, due to the fact that the primary aim of this work is developing a computational tool from scratch based on SPH, a single species modeling is adopted to avoid such unnecessary complexities.

2- Depending to which category bacteria belong, even if we have a single species, they need several nutritional substrates. For the sake of simplicity it is assumed that the growth process is limited and affected by the concentration of just one type of nutrient and the other

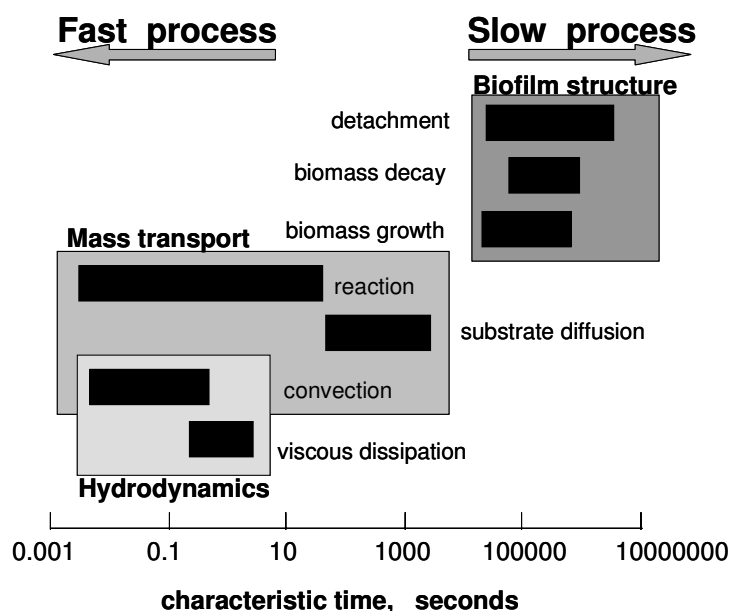


Figure 2.3. Characteristic time scales of processes occurring in the biofilm development, reprinted from PICIOREANU ET AL. (2000)

components are unlimitedly supplied. It implies that there is only one diffusion-advection-reaction equation in the computational method corresponding to this substrate, see PICIOREANU ET AL. (2000), XU ET AL. (2011).

3- Except the nutrient concentration, All other environmental conditions such as PH and temperature are excluded from the modeling and assumed to be constant. In our experiment, the temperature and PH of the bulk fluid are kept constant. Nevertheless, it has been found that the chemical reaction taking place in the biofilm, changes the PH inside it. This will affect the diffusion process consequently, see FLORA ET AL. (1993). Moreover, temperature has a great impact on the biofilm production, see HOŠTACKÁ ET AL. (2010).

4- The biofilm is considered to behave like a homogenous and isotropic elastic material under the mechanical loads. The fluid is taken to be an incompressible Newtonian fluid. The material properties such as elastic modulus, Poisson ratio, etc have been extracted from the literature.

5- Cell-to-cell biological-chemical communication (quorum sensing) is not incorporated in the model, because it make the problem much more complex and introduce several unknown parameters into the modeling. There are some mathematical descriptions for quorum sensing in the literature. For example the reader is referred to CHOPP ET AL. (2002).

2.3 Theory of the volumetric growth for biological tissues

Unlike the structural material, biological tissues are able to change their geometry and internal structure even when they are not subjected to mechanical loads. Such a process is referred

as "growth" and "remodeling". Healing in a cracked bone and development of tumors are examples of biological tissue remodeling and growth, respectively. Soft tissues like tumors, biofilms and arteries experience growth, while hard tissues such as bone and teeth undergo remodeling. Roughly saying, in the growth process the mass generation leads to an increase in the volume, whereas in remodeling the volume remains almost constant and solely the micro structure of the tissue changes, instead. This change in the micro-structure manifests itself in a change in the density and consequently weighting the free energy. In other words, the growth process is a volumetric mass generation but remodeling is in fact a growth occurring at surfaces and interfaces. For remodeling case, the material behavior is characterized by constitutive approach, but in case of growth a kinematic approach in conjunction with a constitutive model is utilized, see HIMPEL ET AL. (2005). Biological tissues undergoing growth and remodeling involve the strong coupling of the physical phenomena. Several distinct types of physics such as mass transport, chemical reactions, mechanics, charge transport and heat transport are governed by the associated equations in a coupled fashion. Here the focus is on the volumetric growth using a combined constitutive-kinematic approach in soft tissues and the objective is to present a mathematical continuum frame work for that.

2.3.1 Kinematics of growth

The key idea for mechanics of volumetric growth has been borrowed from the central idea of finite strain plasticity by decomposing the deformation gradient into an inelastic growth tensor and an elastic tensor. In an analogy with elasto-plastic deformation, a strain energy function is defined based on the elastic part and the growth part is governed by an evolutionary equation translating the mass resorption at a material point. As mentioned in chapter (1), The local nature of the growth-elastic decomposition inherently leads to residual stresses in order to accommodate to the probably incompatible growth-related deformation. This is actually the cost for maintaining the continuity of the solid, see TABER (1998). In the presence of dissipative processes such as viscous effects in large time scales and crack propagation, such residual stresses may be released. That is why a logged tree cracks due to the release of growth stresses.

To start with the mathematical frame work, we consider the well known potato in continuum mechanics as a body, see figure (2.4). Let \mathcal{B}_0 be the initial configuration of the body. \mathbf{F} is the local deformation gradient that relates an infinitesimal material line element from \mathcal{B}_0 to its map in the deformed configuration \mathcal{B}_t at time t . In this formulation, the deformation from \mathcal{B}_0 to \mathcal{B}_t is imaginarily decomposed into two steps. First the material points are mapped into a new, grown, stress-free state. It means that an intermediate auxiliary configuration \mathcal{B}_g is introduced. The collection of these grown states is denoted \mathcal{B}_g and is not necessarily compatible i.e., parts of the body may intersect. The second step applies an elastic deformation to the incompatible state \mathcal{B}_g , obtaining the state \mathcal{B}_t which may now contain residual stresses in order to accommodate the incompatibility of the former state and maintain the continuity of the solid body. In the language of continuum mechanics, the gradient deformation tensor is multiplicatively split as follows

$$\mathbf{F} = \mathbf{F}_e \mathbf{F}_g. \quad (2.1)$$

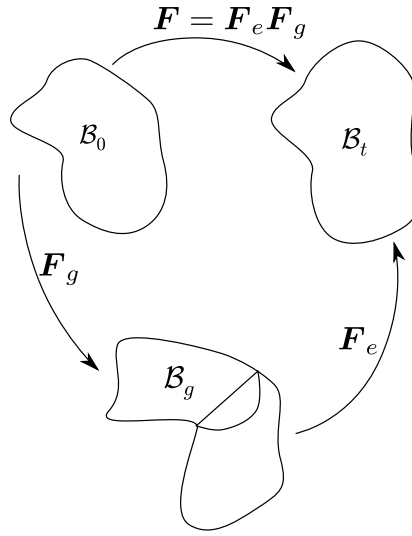


Figure 2.4. Multiplicative decomposition of the gradient deformation in finite growth

This decomposition is formally analogous to the well-known decomposition of elasto-plastic deformation gradient into its elastic and plastic parts and was first introduced in biomechanics by RODRIGUEZ ET AL. (1994). The deformation gradients F_e and F_g are not unique because arbitrary local material rotations can be superposed to the unstressed intermediate configuration \mathcal{B}_g preserving it unstressed. Hence, one can write

$$F = F_e F_g = F'_e F'_g, \quad (2.2)$$

where

$$F'_e = F_e Q^T, \quad F'_g = Q F_g, \quad (2.3)$$

in which Q denotes any rotation tensor. There are undoubtedly fundamental assumptions behind this multiplicative decomposition of deformation. First, the tissue undergoing growth must behave elastically on the timescale of growth or at least relaxation of the stresses must be negligible. Most tissues in practice experience a certain amount of relaxation corresponding to the viscous effect. Second, the elastic timescale associated with elastic wave propagation should be much shorter than the timescale associated with growth. This means that the elastic deformation F_e occurs instantaneously in response to the growth, F_g . Finally, the growth process being modeled needs to be expressible in terms of deformation gradient. This is not always possible. For instance, growth due to the mass generation on a surface is not a bulk process, see JONES & CHAPMAN (2012).

In general, the growth tensor F_g can be defined as a function of stress, position, density, nutrient concentration, or any number of other field variables that may have an effect on the growth rate of the tissue.

While the mass generation is assumed to take place only between the states \mathcal{B}_0 and \mathcal{B}_g , the elastic response occurs only between \mathcal{B}_g and \mathcal{B}_t . In fact the state \mathcal{B}_g is assumed to be stress free. Thus, the elastic strain energy per unit grown unstressed volume W is only a function of the elastic part of F . Then, the second PiolaKirchhoff stress tensor S referred to the state

\mathcal{B}_g is given by

$$\mathbf{S} = \frac{\partial W}{\partial \mathbf{E}_e}, \quad (2.4)$$

in which \mathbf{E}_e represents the Green Lagrange strain tensor as follows

$$\mathbf{E}_e = \frac{1}{2}(\mathbf{F}_e^T \mathbf{F}_e - \mathbf{I}), \quad (2.5)$$

where the subscript "e" refers to the fact that the quantity is formed using the elastic deformation gradient \mathbf{F}_e rather than \mathbf{F} . If the right polar decomposition for \mathbf{F}_g is used, one can write

$$\mathbf{F}_g = \mathbf{R}_g \mathbf{U}_g, \quad (2.6)$$

where \mathbf{R}_g and \mathbf{U}_g are rotation and stretch part of the growth tensor. Without the loss of generality \mathbf{R}_g can always be taken to be equal to the identity tensor. This makes the formulation of growth much more simple. In fact one can assume that the rotation part of the total deformation \mathbf{F} is captured by \mathbf{F}_e . From the mathematical point of view, it can be said that \mathbf{R}_g is absorbed into \mathbf{F}_e , see RODRIGUEZ ET AL. (1994).

Now, one needs to construct the \mathbf{F}_g . It is common to consider two different cases for growth. First, growth in constant density and the second growth in constant volume. In the former, the volume changes to accommodate the newly generated mass and in the latter the density variation reflects the change in mass, see HIMPEL ET AL. (2005). In this work, the first approach is utilized. With the assumption of density preservation, volume change during growth can be specified by

$$J_g = \det(\mathbf{F}_g) = \frac{V}{V_0}, \quad (2.7)$$

with V and V_0 being the local tissue volumes before and after the growth increment, respectively. It is common to assume that the new tissue constituents are deposited in all directions equally (isotropic growth) and hence \mathbf{F}_g has the form

$$\mathbf{F}_g = J_g^{\frac{1}{3}} \mathbf{I} = \left(\frac{V}{V_0}\right)^{\frac{1}{3}} \mathbf{I}, \quad (2.8)$$

in which \mathbf{I} is the identity tensor. This idea of constructing growth tensor can be easily extended to non-isotropic growth. For example, if there is a preferred direction m along which the growth occurs only in longitudinal mode (transversely isotropic growth), one can build the growth tensor as follows

$$\mathbf{F}_g = J_g^{\frac{1}{3}} \mathbf{I} + (J_m - J_g^{\frac{1}{3}}) m \otimes m, \quad (2.9)$$

where J_m is the growth factor in direction m . It is obvious that \mathbf{F}_g has been constructed in such a way that $\mathbf{F}_g m = J_m m$. From the mathematical point of view it means that m and J_m correspond to eigenvector and eigenvalue of \mathbf{F}_g , respectively.

Now we should relate the stimuli of the growth to growth tensor by means of a phenomenological description. As it was mentioned before, several variables can be regarded as the growth stimulus such as stress, concentration field of an agent and so on. The idea is that there is a homeostatic state in which now growth occurs. A supra-homeostatic load will lead

to a net increase of volume (growth), whereas a sub-homeostatic load will lead to a decrease of volume (resorption).

$$\dot{V} = \beta V_0 (s - s_{hom}), \quad (2.10)$$

where β is the rate constant and s and s_{hom} are scalars denoting the stimuli and the homeostatic value of that. Linearization with respect to volume V_0 at the start of the growth increment yields

$$\frac{V}{V_0} = \beta V_0 (s - s_{hom}) \Delta t + 1. \quad (2.11)$$

Finally, plugging equation (2.11) into equation (2.8), the growth deformation tensor reads

$$\mathbf{F}_g = [\beta V_0 (s - s_{hom}) \Delta t + 1]^{\frac{1}{3}} \mathbf{I}. \quad (2.12)$$

The above formulation can be implemented in the context of any numerical method such as FEM or SPH. If the numerical solver is implicit, a tangent modulus needs to be derived for the Newton-Raphson iteration. We obtain the incremental elastic-growth tangent stiffness tensor \mathbb{C} in the intermediate configuration similar to the procedure in elasto-plastic finite deformation. It means that the variables such as Second-Piola stresses should be transformed from the reference configuration \mathcal{B}_0 to intermediate configuration \mathcal{B}_g by appropriate push forward operators. As a convention, the variables in \mathcal{B}_g have a hat. For example $\hat{\mathbf{S}}$ is the stress tensor in the intermediate configuration obtained by applying a push forward operator on the second Piola-Kirchhoff stress tensor as follows

$$\hat{\mathbf{S}} = \mathbf{F}_g \mathbf{S} \mathbf{F}_g^T. \quad (2.13)$$

Using the chain rule for computing the total elasto-growth tangent stiffness tensor $\hat{\mathbb{C}}_{n+1}^{eg}$ gives

$$\hat{\mathbb{C}}_{n+1}^{eg} = 2 \frac{d\hat{\mathbf{S}}_{n+1}}{d\hat{\mathbf{C}}_{n+1}} = 2 \frac{\partial \hat{\mathbf{S}}_{n+1}}{\partial \hat{\mathbf{C}}_{n+1}} + 2 \frac{\partial \hat{\mathbf{S}}_{n+1}}{\partial \vartheta_{n+1}} \otimes \frac{\partial \vartheta_{n+1}}{\partial \hat{\mathbf{C}}_{n+1}}, \quad (2.14)$$

in which $\vartheta = J_g^{\frac{1}{3}}$. It implies that $\mathbf{F}_g = \vartheta \mathbf{I}$.

The first term in the right hand side of equation (2.14) is nothing else than the standard elastic tangent, namely $\hat{\mathbb{C}}^e = 2 \frac{\partial \hat{\mathbf{S}}}{\partial \hat{\mathbf{C}}}$. In order to determine the second term, we apply again the chain rule

$$2 \frac{\partial \hat{\mathbf{S}}_{n+1}}{\partial \vartheta_{n+1}} = 2 \frac{\partial \hat{\mathbf{S}}_{n+1}}{\partial \hat{\mathbf{C}}_{n+1}} : \frac{\partial \hat{\mathbf{C}}_{n+1}}{\partial \vartheta_{n+1}} = -\frac{2}{\vartheta} \hat{\mathbb{C}}^e : \hat{\mathbf{C}}, \quad (2.15)$$

in which $\hat{\mathbf{C}}$ can be calculated by applying an appropriate push forward operator on the right Cauchy-Green tensor \mathbf{C} ($\mathbf{C} = \mathbf{F}^T \mathbf{F}$) using $\hat{\mathbf{C}} = \mathbf{F}_g^{-T} \mathbf{C} \mathbf{F}_g^{-1}$. Besides, the term $\frac{\partial \hat{\mathbf{C}}_{n+1}}{\partial \vartheta_{n+1}}$ is computed as follows

$$\frac{\partial \hat{\mathbf{C}}_{n+1}}{\partial \vartheta_{n+1}} = \frac{\partial (\mathbf{F}_g^{-T} \mathbf{C}_{n+1} \mathbf{F}_g^{-1})}{\partial \vartheta_{n+1}} = -2\vartheta^{-3} \mathbf{C}_{n+1} = -2\vartheta^{-1} \hat{\mathbf{C}}_{n+1}. \quad (2.16)$$

It should be noted that one can easily obtain the inverse of $\mathbf{F}_g = \vartheta \mathbf{I}$ as follows

$$\mathbf{F}_g^{-1} = \frac{1}{\vartheta} \mathbf{I}. \quad (2.17)$$

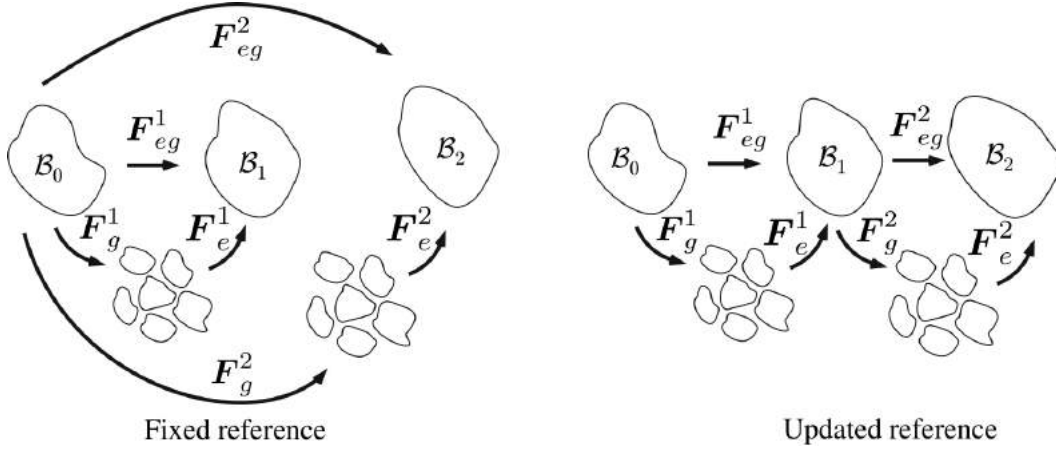


Figure 2.5. Fixed and updated reference configuration for the incremental growth

The computation of the third part of equation (2.14) is not straightforward, since solely the evolution of the ϑ is known, not itself (similar to the plasticity in which the evolutionary equation for the plastic strain gives in fact the incremental value of that not itself). Therefore we apply an implicit Euler backward scheme to obtain the stretch ratio at the spatial time step

$$\vartheta_{n+1} = \vartheta_n + \dot{\vartheta}_{n+1} \Delta t. \quad (2.18)$$

Applying the differentiation gives

$$\frac{\partial \vartheta_{n+1}}{\partial \hat{\mathbf{C}}_{n+1}} = \left(\frac{\partial \dot{\vartheta}_{n+1}}{\partial \hat{\mathbf{C}}_{n+1}} + \frac{\partial \dot{\vartheta}_{n+1}}{\partial \vartheta_{n+1}} \frac{\partial \vartheta_{n+1}}{\partial \hat{\mathbf{C}}_{n+1}} \right) \Delta t. \quad (2.19)$$

Solving equation (2.19) for $\frac{\partial \vartheta_{n+1}}{\partial \hat{\mathbf{C}}_{n+1}}$, one can obtain

$$\frac{\partial \vartheta_{n+1}}{\partial \hat{\mathbf{C}}_{n+1}} = \frac{1}{K} \frac{\partial \dot{\vartheta}_{n+1}}{\partial \hat{\mathbf{C}}_{n+1}} \Delta t, \quad (2.20)$$

in which $K = 1 - \frac{\partial \dot{\vartheta}_{n+1}}{\partial \vartheta_{n+1}} \Delta t$. It should be stressed that the term $\frac{\partial \dot{\vartheta}_{n+1}}{\partial \hat{\mathbf{C}}_{n+1}}$ is computed using the constitutive equation relating the growth to deformation. In this work, this term is zero because the evolutionary equation for the ϑ is solely a function of concentration field. It means that the growth stimulus is solely the concentration field, see equation (2.11).

Finally it is worthwhile to know that the incremental growth can be handled using either a fixed reference configuration or an updated one. The former is usually referred to as "total Lagrangian formulation" and the latter is called "updated Lagrangian formulation". Figure (2.5) illustrates these two possible reference configurations for the incremental growth kinematics. The readers seeking more details can refer to KROON ET AL. (2008).

2.4 On the hypo-elastic approach in solid mechanics

2.4.1 Historical background

Hypo-elasticity was proposed firstly by TRUESDELL (1955) in 1955. Since then, there had been some misunderstanding and misconception among some researchers about it. All the discussions were about the bridges between hypo-elasticity and hyper-elasticity. In the following years, Bernstein in communication with Truesdell addressed this question if any hypo-elastic material is elastic or not, see BERNSTEIN (1960). Then, Truesdell himself shed light on some gray aspects of hypo-elasticity in 1963, see TRUESDELL (1963). He clearly criticized some researchers, saying: "When I proposed the theory of hypo-elasticity, I sought a new concept of elastic behavior, mutually exclusive with the theory of finite elastic strain except in the linearized case, and I was surprised, although indeed groundlessly, when Noll, see NOLL (1955), proved that every isotropic elastic material with invertible stress-strain relation is hypo-elastic. Misled, apparently, by Noll's theorem, Hill and Prager HILL (1959) have asserted that every elastic material is hypo-elastic, making hypo-elasticity appear to be a generalization of the classical theory of finite elastic strain. This, certainly, it is not". Anyway, hypo-elastic approach was utilized as a constitutive model in the computational mechanics. There was still the question of whether such constitutive models are equivalent to hyper-elastic based ones or not? For example in a simple case, does the constant tensor which relates the stress to strain in small deformation theory (Hook's law) can be employed if one uses a proper objective stress rate and strain rate? The final word was delivered by Simo in 1984, see SIMO & PISTER (1984). It is worth re quoting some sentences from his paper. He says: "The purpose of this paper is to show that rate constitutive models of this type widely employed in computational mechanics are in fact, not only incompatible with the notion of hyper-elasticity, in the sense that a stored energy function does not exist, but even fail to define an elastic material in nonlinear range." He mathematically proved that the rate based relations are integrable to construct a strain energy under certain condition. It means that, If the hypo-elastic constitutive equation meet some requirements, then it is equivalent to hyper-elasticity.

2.4.2 Mathematical framework of hypo-elasticity

Using the incremental formulation for solving large deformation problem necessitates the developing of incremental constitutive equation which relates the stress increment (rate) to strain increment (rate). Such constitutive equations are finally translated into so-called "material stiffness tangent". In hyper-elastic approach the existence of a free energy is postulated and then the stress and stress increment is mathematically derived from that. For more details on different free energy form and the associated constitutive equations the interested readers are referred to HOLZAPFEL (2000). In hypo-elasticity unlike hyper-elastic approach, the constitutive equation connecting the increments of stress and strain is not derived from a free energy function. Rather, the start point is an explicit spatial relation between an objective stress rate and strain. Of objective stress rates, one can mention the Jaumann rate, GreenNaghdi rate, Oldroyd rate and Truesdell rate. So the general form of a hypo-elastic

constitutive equation is as follow

$$\overset{\Delta}{\boldsymbol{\tau}} = \boldsymbol{c} : \boldsymbol{d}, \quad (2.21)$$

in which $\overset{\Delta}{\boldsymbol{\tau}}$ is an objective rate of Kirchhoff (or Cauchy) stress tensor and \boldsymbol{d} is the rate of deformation tensor. Lack of experimental evidence to construct a variable function for \boldsymbol{c} often leads to the assumption of a constant isotropic elasticity tensor of the linear theory. In practice, It means that the constant elasticity tensor relating the stress and strain in small deformation theory is used as \boldsymbol{c} that relates the stress rate to strain rate, as well. But the fact is that different objective stress rates may result in different elastic deformations, unless elastic moduli \boldsymbol{c} are properly defined. As mentioned in the previous section, it was mathematically proved by SIMO & PISTER (1984) that a nonlinear elastic material can not have a spatial, constant and isotropic tensor. This finding actually ruins the applicability of hypo elastic approach for large deformation problem. In fact if a large deformation problem for an elastic solid is solved using a constant modulus and hypo-elastic approach, the results are not accurate and actually the simulated response is not elastic. Simply speaking, the net work produced in a closed cycle is not zero, see SIMO & PISTER (1984).

To summarize this introduction with a key message and go to the mathematical framework, it can be said that the constitutive equations based on the hypo-elasticity are equivalent to those based on hyper-elasticity with the assumption of small deformation. It does not matter if large displacement or rotation takes place. Especially in the cases in which severe volume change occurs (determinant of deformation gradient deviates significantly from unity), the results of the hyper elastic approach differ from hypo-elastic one drastically, see SIMO & PISTER (1984).

It can be said that all objective rates are a particular case of the Lie derivative. To calculate the Lie derivative, a quantity is transformed to the reference configuration using a pull back operator and the derivation is taken there. Then, the derivation is transformed back to the spatial current configuration using a push forward operator. In the below subsections, this concept is clarified more. For more detail see WRIGGERS (2008). The reason why objective rates are needed for constitutive equations is that such rates are frame invariant and the rigid body motion has been considered in their formulation. In other words, if a stressed body undergoes a rigid body motion one expects that no further stress is induced in it. Objective rates meet this requirement while the normal stress rate does not. In this section, the application of different objective rates is briefly discussed. Finally the adopted one for this work is introduced.

Oldroyd rate

If one wishes to take the Lie derivative of Kirchhoff stress $\mathcal{L}\boldsymbol{\tau}$, first it is transformed to the reference configuration using an appropriate operator for contravariant tensors (\boldsymbol{F}^{-1} and \boldsymbol{F}^{-T} are pre and post multiplied by the tensor). Once the derivation is done, it is transformed again to the current configuration (\boldsymbol{F} and \boldsymbol{F}^T are pre and post multiplied by the tensor).

$$\mathcal{L}\boldsymbol{\tau} = \boldsymbol{F} \frac{\partial}{\partial t} [\boldsymbol{F}^{-1} \boldsymbol{\tau} \boldsymbol{F}^{-T}] \boldsymbol{F}^T, \quad (2.22)$$

with $\dot{\mathbf{F}}^{-1} = \mathbf{F}^{-1}\mathbf{F}\mathbf{F}^{-1}$ and $\dot{\mathbf{F}} = \mathbf{l}\mathbf{F}$ and some algebraic manipulation one can find that

$$\mathcal{L}\boldsymbol{\tau} = \dot{\boldsymbol{\tau}} - \mathbf{l}\boldsymbol{\tau} - \boldsymbol{\tau}\mathbf{l} = \overset{\Delta}{\boldsymbol{\tau}}, \quad (2.23)$$

in which \mathbf{l} is the spatial velocity gradient ($\mathbf{l} = \frac{\partial \mathbf{v}}{\partial \mathbf{x}}$). One can see that the Oldroyd rate is in fact the Lie derivative of the Kirchhoff stress.

Green Naghdi rate

In equation (2.23), if \mathbf{l} is replaced by $\boldsymbol{\Omega} = \dot{\mathbf{R}}\mathbf{R}^T$ the Green-Naghdi $\overset{\Delta G}{\boldsymbol{\tau}}$ rate is obtained. \mathbf{R} is the rotation part of the gradient deformation ($\mathbf{F} = \mathbf{R}\mathbf{U}$). Actually the Green-Naghdi rate is the Lie derivative of Kirchhoff stress transformed by \mathbf{R} instead of \mathbf{F} . This transformation has been shown using the notation $\mathcal{L}^{\mathbf{R}}\boldsymbol{\tau}$ as follows

$$\mathcal{L}^{\mathbf{R}}\boldsymbol{\tau} = \dot{\boldsymbol{\tau}} - \boldsymbol{\Omega}\boldsymbol{\tau} + \boldsymbol{\tau}\boldsymbol{\Omega} = \overset{\Delta G}{\boldsymbol{\tau}}. \quad (2.24)$$

Jaumann rate

If one uses the antisymmetric part of the velocity gradient $\mathbf{W} = \frac{1}{2}[\mathbf{l} - \mathbf{l}^T]$ as the transformation operator in Lie derivative ($\mathcal{L}^{\mathbf{W}}\boldsymbol{\tau}$), the Jaumann rate of Kirchhoff stress $\overset{\Delta J}{\boldsymbol{\tau}}$ is obtained as follows

$$\mathcal{L}^{\mathbf{W}}\boldsymbol{\tau} = \dot{\boldsymbol{\tau}} - \mathbf{W}\boldsymbol{\tau} + \boldsymbol{\tau}\mathbf{W} = \overset{\Delta J}{\boldsymbol{\tau}}. \quad (2.25)$$

It is worth noting that the Jaumann rate is a special case of Green-Naghdi rate if $\mathbf{W} = \boldsymbol{\Omega}$. This happens if the symmetric part of the velocity gradient is zero ($\mathbf{d} = \frac{1}{2}[\mathbf{l} + \mathbf{l}^T] = 0$).

Due to the simplicity in the implementation and lower computational cost (one does not need to perform a polar decomposition of gradient deformation \mathbf{F}), the Jaumann rate is adopted in this work.

Remark: the aforementioned objective rates give the identical results if a pre-stresses material point is solely subjected to rigid body motion. However, it has been shown that they result in different outcomes if the same material modulus is used for general cases. Especially in a simple shear problem, the results vary dramatically in large time periods. For more detail, the interested readers may refer to BELYTSCHKO ET AL. (2002). Besides, a comparative study of hypo-elastic and hyper-elastic material models for large deformation has been presented in KIM (2016).

2.5 Governing equations

In this section, the governing equations of a biofilm system are presented in a continuum-based framework.

2.5.1 Mass balance (continuity)

Recalling from the continuum mechanics, the local form of the mass balance equation of a regular body not undergoing growth is

$$\frac{\partial \rho}{\partial t} + \nabla \cdot (\rho \mathbf{v}) = 0, \quad (2.26)$$

where ρ and \mathbf{v} are the density and the velocity field, respectively. This equation is applicable for the fluid compartment (Ω_f). But when it comes to a biological body which may experience growth, the mass balance equation needs to be modified and indeed the right hand side of equation (2.26) is replaced by a source term γ accounting for the mass generation due to the growth JONES & CHAPMAN (2012) as follows

$$\frac{\partial \rho}{\partial t} + \nabla \cdot (\rho \mathbf{v}) = \gamma. \quad (2.27)$$

γ can be in general a function of other field variables. For example the reciprocal connection between growth and stress is interesting. It is obvious that from one hand tissues undergoing non-uniform growth will experience residual stresses, see CHEN & HOGER (2000), and on the other hand, the stresses will affect further growth, see JONES & CHAPMAN (2012), RODRIGUEZ ET AL. (1994). Here it is assumed that the growth function γ is only a function of the nutrient concentration according to the Monod kinematic RITTMANN & MCCARTY (1982). The Monod law is

$$\gamma = Y \frac{K_1 C}{K_2 + C}, \quad (2.28)$$

where Y is the true yield of bacterial mass per unit mass of the nutrient consumption, K_1 and K_2 are biological constants related to the type of bacteria species and C is the concentration of nutrient.

It is noteworthy to mention that the right-hand side of equation (2.27) is like a chain which couples diffusion-reaction equation for nutrient concentration in the biofilm and its mechanical response.

In general adding a scalar source term into the continuity equation is not sufficient to capture the inhomogeneous growth which generally results in residual stresses. Rather, it is required to start from a multiplicative decomposition of the deformation in a tensorial sense as discussed in section (2.3.1). But here, due to the fact, that the focus is on the time periods whose order of magnitude is larger than the biological growth time scale, the biofilm behaves like a homogeneous viscous fluid and all internal stresses are released JONES & CHAPMAN (2012)-KROON ET AL. (2008) and hence the scalar source term in the continuity equation is sufficient (homogeneous growth).

2.5.2 Diffusion-advection-reaction

In the biofilm domain (Ω_b) the nutrient concentration C is an unknown field variable and is computed using the diffusion-advection-reaction equation, as follows

$$\frac{\partial C}{\partial t} + \nabla C \cdot \mathbf{v} = D \nabla^2 C - \frac{\gamma}{Y}, \quad (2.29)$$

where D is the diffusivity coefficient and $\frac{\gamma}{Y}$ is the consumption term expressed in equation (2.27). It should be stressed that \boldsymbol{v} is the advective velocity of the biofilm as the result of the growth process. Recalling the discussion in section (2.2), the advection term for the nutrient concentration in the biofilm is neglected because the order of the growth velocity is $10^{-5}mm/s$. It means that the dominant transport mechanism in the biofilm is diffusion, see DUDDU ET AL. (2009). Hence the final nutrient concentration equation which is going to be solved is

$$\frac{\partial C}{\partial t} = D\nabla^2 C - \frac{\gamma}{Y}. \quad (2.30)$$

It is a common assumption that the fluid compartment (Ω_f) is well mixed due to the dominance of advection transport mechanism and the nutrient concentration is a prescribed variable in the bulk fluid, but it is computed in the biofilm using the diffusion-consumption equation. In our experiment, the bulk fluid is continuously pumped into the system (see figure (2.2)) and in fact the fluid phase is continuously enriched with the fresh nutrient so that the concentration of the nutrient in the bulk fluid remains constant.

Boundary conditions

The boundary conditions for equation (2.30) are as follows

$$C = C_{bulk} \quad \text{on } \Gamma_{fb}, \quad (2.31a)$$

$$\frac{\partial C}{\partial \boldsymbol{n}} = 0 \quad \text{on impermeable substratum}. \quad (2.31b)$$

Equation (2.31a) insures the continuity of the concentration field at the biofilm-fluid interface. C_{bulk} is the externally prescribed concentration in the bulk fluid phase and \boldsymbol{n} denotes the unit normal vector to Γ_{fb} . Equation (2.31b) says that the substratum plate is impermeable and in fact no flux of concentration is transported from there.

2.5.3 Momentum balance

In general, every mass source due to the growth phenomena is an inherent momentum source as well. This makes both the linear and angular momentum equations complicated. In such a case, the Cauchy stress tensor is not symmetric anymore owing to a source term in the angular momentum equation, see EPSTEIN & MAUGIN (2000). However, under certain assumptions these effects could be neglected and introducing the growth effect in the continuity equation suffices. The fundamental assumption is that the velocity, specific energy and specific entropy of the newly deposited material is "miraculously" equal to those of the existing material and this is the case for biological slow growth VOLOKH (2006) and hence the linear momentum equation has the regular and well-known structure.

$$\rho \dot{\boldsymbol{v}} = \nabla \cdot \boldsymbol{\sigma} + \rho \boldsymbol{b}, \quad (2.32)$$

in which $\boldsymbol{\sigma}$ and \boldsymbol{b} are the Cauchy stress and body force, respectively. The angular momentum leads to the symmetricity of the Cauchy stress.

Boundary conditions

The biofilm is subjected to mechanical loads due to its interaction with the surrounding fluid. In other words, the traction is transmitted from the fluid to the biofilm through the interface Γ_{fb} (see Figure (2.2)). It is as a result of the kinematic and dynamic compatibility conditions which need to be enforced at the interface as follows

$$\mathbf{v}_f = \mathbf{v}_b \quad \text{on } \Gamma_{fb}, \quad (2.33a)$$

$$\boldsymbol{\sigma}_f \cdot \mathbf{n} = \boldsymbol{\sigma}_b \cdot \mathbf{n} \quad \text{on } \Gamma_{fb}, \quad (2.33b)$$

$$\mathbf{v}_b = 0 \quad \text{on impermeable substratum}, \quad (2.33c)$$

where $\boldsymbol{\sigma}_f$ and $\boldsymbol{\sigma}_b$ denote the stress in the fluid and biofilm, respectively. Furthermore \mathbf{v}_f is the fluid velocity and \mathbf{v}_b stands for the biofilm velocity. \mathbf{n} is the normal vector to the Γ_{fb} . Equation (2.33a) ensures the equality of the velocities and equation (2.33b) accounts for the continuity of the traction at the interface. The numerical treatment and implementation strategies will be discussed in chapter (3). Equation (2.33c) is a Dirichlet's boundary condition for the biofilm compartment. It reflects the the status of the biofilm at its base where it is attached to a rigid and impermeable substratum.

2.5.4 Constitutive equations

In this section the material behavior of the system, including the biofilm and surrounding fluid, is presented.

Fluid compartment

It is common that the stress tensor can be decomposed into isotropic (pressure) p and deviatoric s parts according to the following equation

$$\sigma_{ij} = -p\delta_{ij} + s_{ij}, \quad (2.34)$$

where δ_{ij} is the Kronecker tensor. Assuming a Newtonian fluid, the deviatoric stress is proportional to the deviatoric strain rate ($\dot{\epsilon}_{ij}$).

$$s_{ij} = 2\mu_f \dot{\epsilon}_{ij}, \quad (2.35)$$

where μ_f is the fluid dynamic viscosity and ϵ_{ij} is computed using

$$\dot{\epsilon}_{ij} = \frac{1}{2} \left(\frac{\partial v_i}{\partial x_j} + \frac{\partial v_j}{\partial x_i} \right) - \frac{1}{3} \frac{\partial v_k}{\partial x_k} \delta_{ij}, \quad (2.36)$$

in which the Einstein's summation rule has been applied for the index k . \mathbf{v} is the velocity field.

Biofilm compartment (elastic solid)

As mentioned before, biofilm behaves like a fluid in the growth process, but in short time scales it acts like a solid ALPKVIST & KLAPPER (2007). In other words, it is necessary to model the biofilm as a deformable solid, if its interaction with the surrounding fluid is the objective.

Due to the nature of SPH, it is more convenient to use a hypo-elastic approach instead of a hyper-elastic one for deformable solid. As discussed in section (2.4), rate constitutive equations are used to reflect the material behavior. Such constitutive laws are similar to equations (2.34)-(2.36) with the modification that the stress rate is proportional to the strain rate and μ_f is replaced by μ_s representing the shear modulus of the solid. The Jaumann rate is the most widely adopted in SPH, see LIBERSKY ET AL. (1993), GRAY (2001)

$$\dot{s}_{ij} - s_{ik}\omega_{jk} - \omega_{ik}s_{kj} = 2\mu_s\dot{\epsilon}_{ij}. \quad (2.37)$$

Recalling Einstein's summation notation and material time derivative ($\dot{}$), the whole left hand side of equation (2.37) is indeed the Jaumann stress rate and the tensor ω_{ij} is called the "spin tensor" and it is calculated using

$$\omega_{ij} = \frac{1}{2} \left(\frac{\partial v_i}{\partial x_j} - \frac{\partial v_j}{\partial x_i} \right). \quad (2.38)$$

As discussed in the section 2.4.1 the application of such rate constitutive equations while assuming spatially constant coefficient, is quite questionable and in fact incompatible with elasticity when large deformation and especially severe volume change takes place. Nevertheless, in this work with the assumption of moderate deformations, this effect has been neglected.

2.5.5 Erosion (detachment)

The detachment process in the biofilm formation has different mechanisms such as erosion, sloughing, abrasion, predator grazing and human intervention, see BRYERS (1988). The ones which have a hydrodynamical root are erosion and sloughing. In this work, the focus is on the interface erosion in which the bacteria (particles) are gradually washed away because of the shear forces of the flow. To avoid any ambiguity, some important aspects of biofilm detachment need to be clarified here.

First, the process is local and takes place at the micro-scale and hence it is almost impossible to have a real-time experimental measurement from which a macroscopic balance of mass could be deduced, see DUDDU ET AL. (2009). In practice, most experiments on biofilm are solely measurement of the average height in some points of interests during large time scales of order hours and days. In such a large time scales, the outcome is indeed the resultant of all processes contributing to the biofilm formation (growth, erosion, sloughing etc.) and decomposing the real portion of impact for each of these processes is not possible. In other words, the numerical erosion model of the biofilm could not be quantitatively verified through experiments that have been conducted in this research. Nevertheless, it is still a powerful tool to understand qualitatively the physics behind the erosion process in biofilms.

Second, it has been assumed that the erosion occurs at the fluid-biofilm interface in the form of a single particle removal when the shear stress induced by the fluid exceeds the biofilm strength, as follows

$$\tau_{interface} > \tau_y. \quad (2.39)$$

Here $\tau_{interface}$ represents the shear stress induced by the fluid flow and τ_y is the shear yield stress in biofilm. τ_y is a material parameter that reflects the strength of the biofilm prior to detachment. Similar to the Young modulus, no unique value has been reported in the literature for the strength of biofilms and it lies in a range from a few tenth of 1 Pa to tens of Pascals, see BÖL ET AL. (2009).

Third, It is well known that the biofilm is a heterogeneous material and its cohesion strength varies from the order of 10 Pa in the base where it is attached to the substratum to the order of 0.1 Pa near the interface, see DUDDU ET AL. (2009). Unfortunately, measuring the mechanical properties of a biofilm which govern its response is a very challenging issue and there is no unique reference value for the mechanical properties in the literature. Thus a wide range of values has been reported. On the other hand, it is obvious that the mechanical stress in the biofilm must be higher at the substratum where it is cantilevered, see BÖL ET AL. (2009). It means it is likely that sloughing, as another failure mode in which a bunch of bacteria as a whole are detached, occurs in addition to the surface erosion. This may happen especially in high Reynolds flow. However, in this study the flow conditions are such that the dominant detachment process is surface erosion and the stresses near the substratum are less than the biofilm strength there. Definitely, a continuum damage or an explicit crack propagation model is required to be incorporated for capturing bulky failure modes within the biofilm and it could be the matter of further future research.

Fourth, capturing the dynamically changing interface accurately is of great importance because this is the region where the biofilm-fluid coupling is taking place. If the interface is not recognized properly several artifacts might appear and finally lead to the crash of the numerical method. Penetration of the fluid into the biofilm, local non-physical tearing of the biofilm due to an abrupt change in the interface geometry and forces, are two common issues in the case that the interface geometry is naively tackled. In this work an algorithm so-called "Alpha shape" has been employed. This has proved to be a robust method especially in case of a general irregular set of particles. This algorithm is based on the Delaunay triangulation of a point cloud and circumscribed rolling circles. It is available in MATLAB software. The input is an arbitrary point cloud and a value corresponding to a rolling circle on the boundary points. The out put is the set of the boundary particles. Figure (2.6) illustrates how the algorithm works.

Finally, the fact that the minimum size of detached material at the interface is equal to the size of the particle might be physically arguable. This is the case not only in mesh-less methods but also in element based methods when the damage and failure phenomena are modeled using "death" of elements. In a general term, it can be said that capturing the strain softening using classical local damage theory suffers from mesh dependence, see BE-LYTSCHKO ET AL. (1986). In other words, the size of the micro-structure plays an important role in the size of damaged (detached) zone. Generally such mesh dependency of material response, which is undesirable, is a matter of discussion when the equations are transformed from continuum to discretization level. Nonetheless, here it can be argued that the biofilm

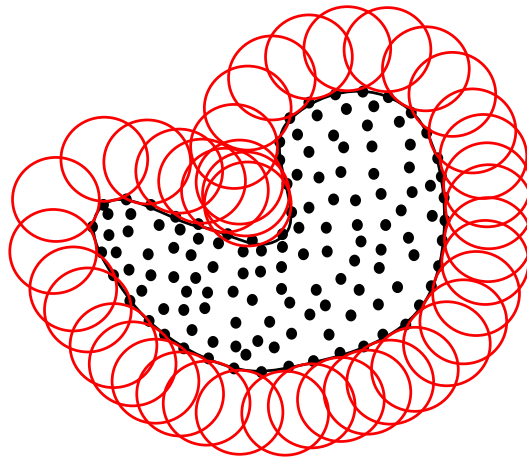


Figure 2.6. Recognizing boundary particles using alpha shape algorithm

micro structure in reality is a composite made of the bacteria as the inclusions being glued together with EPS as a matrix. The damage always happens in the weaker compartment of this composite which is the matrix. It is implied that a single bacteria is not torn apart, but it is detached as a whole. Consequently the minimum size of material removal is confined to the size of a single bacteria. Since here the size of the mesh (particles) is the same as a single bacteria, this modeling of material erosion is justifiable.

Chapter 3

Discretization and implementation

In this chapter, first a brief introductory discussion is presented regarding the different approaches and methods in numerical continuum mechanics in order to know where SPH falls in terms of numerical methods classification. Afterward, the mathematical description of the SPH method is provided. Then some important points regarding the mesh generation is discussed and the governing equations derived in chapter (2) are discretized based on SPH. Furthermore solution procedure, numerical challenges and remedies are discussed in detail.

3.1 Numerical method

3.1.1 Eulerian and Lagrangian perspective

When a physical problem is translated into a mathematical model, it is a common way to distinguish between Lagrangian and Eulerian description of it. In the Lagrangian approach the mesh or grid is attached to the material and moves with it, but in the Eulerian one the mesh or grid is fixed in the space. Of course either of the approaches has its own advantages and drawbacks. While handling the moving or geometrically complex boundaries is a serious challenge in the Eulerian framework, they are easily treated using the Lagrangian description. However, very large deformation in Lagrangian approach entails mesh distortion and needs for the re-meshing procedures which are costly. on the contrary, Eulerian description does not suffer from mesh distortion. Tracking the time history of a variable associated to a material point is quite straight forward in Lagrangian perspective due to the fact that the the material points themselves carry the field variables, whereas in the Eulerian perspective, the variables are associated to a point in spatial domain not a material point. For more comparison and understanding of these two approaches, the readers are referred to LIU & LIU (2003). Considering the characteristics of the two approaches, one can realize why Lagrangian methods such as finite element methods (FEM) are favored in modeling solids, while Eulerian methods such as finite volume methods (FVM) are preferred for computational fluid dynamics (CFD). In the problems in which both fluid and solid are present, For example fluid-solid interactions (FSI), the merits of both description are combined in the context of a method called arbitrary Lagrangian Eulerian (ALE) method, see HUGHES ET AL. (1981). Figure (3.1) illustrates the two different view points for modeling a fluid.

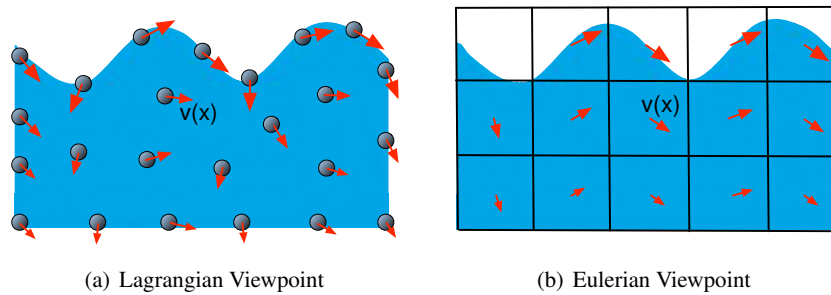


Figure 3.1. Lagrangian vs. Eulerian description

3.1.2 Mesh-less and mesh based methods

While Eulerian perspective is implemented using the mesh based methods, the implementation of the Lagrangian approach may be either mesh based or mesh-less. Although mesh based method have dominated the computational world so far, a great deal of attention has been drawn to mesh-less methods in recent decades. More information about the history and different mesh-less methods can be found in LIU & LIU (2003). Mesh-less methods are less expensive in terms of mesh generation costs. Meshing a complex geometry using specific elements with certain characteristics is not always straight forward. Contrarily, in mesh-less methods the body is represented by a set of arbitrarily distributed points (nodes). Furthermore, mesh-less methods facilitate the treatment of very large deformation which results in so called "mesh distortion" in grid based methods. The readers are referred to LIU (2003) for a comprehensive discussion about mesh-less methods in comparison to finite element.

3.1.3 SPH method

As a fully Lagrangian mesh-less method, Smoothed Particle Hydrodynamics (SPH) has been successfully applied to various physical problems. Reminding the explanations in sections (3.1.1) and (3.1.2), it enjoys both appealing features of being Lagrangian and mesh-less. Its first appearance as a computational method, goes back to 1977 where it was used for computational research in astrophysics, see GINGOLD & MONAGHAN (1977) and LUCY (1977). Since then, it has been proved to be robust and applicable to a variety of fields mentioned in chapter (1). Unlike what is misleadingly inferred from its name, SPH is not a particle-based method such as DEM (Discrete Element Method), rather it is a continuum-based one. However, the discretized governing equations at the mathematical point (nodes) can be interpreted as interactions between them which resembles the particle methods. In other words, due to the Lagrangian nature, the mathematical nodes at which the field variables are to be computed, move with material points and hence it is like that the material points carrying field variables with themselves.

Mathematical framework of SPH

SPH starts with an integral interpolation of a function f using the Delta Dirac function $\delta(\mathbf{r} - \mathbf{r}')$, as follows

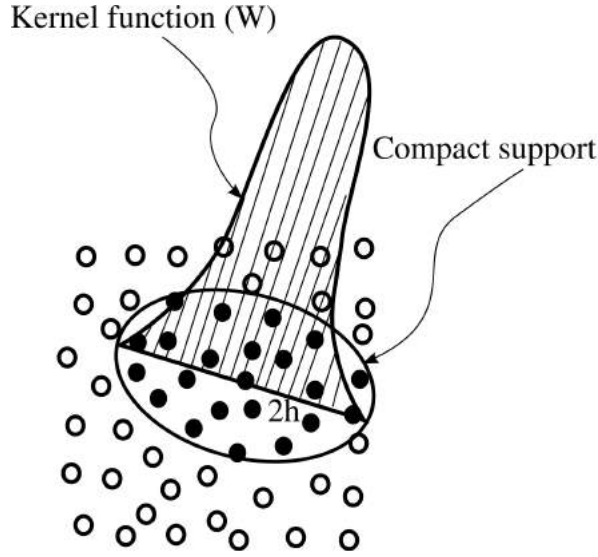


Figure 3.2. Kernel function and the compact support

$$f(\mathbf{r}) = \int f(\mathbf{r}')\delta(\mathbf{r}' - \mathbf{r})d\mathbf{r}', \quad (3.1)$$

where Ω is the domain corresponding to the continuous medium. It should be stressed that equation (3.1) is exact from the mathematical point of view. Nevertheless, the nature of the Delta function renders equation (3.1) unsuitable for numerical implementation. Hence, the Delta function is approximated by a "kernel function", W , whose support is compact. It means that W has a bounded maximum at $\mathbf{r} = \mathbf{r}'$ and gradually goes to zero within a "compact support". By the compact support it is meant that W is equal to zero outside a finite and closed region which is called the domain of influence, see figure (3.2).

Replacing the Delta function by the kernel function, one can write

$$f(\mathbf{r}) \approx \int_{\Omega} f(\mathbf{r}')W(\mathbf{r}' - \mathbf{r})d\mathbf{r}'. \quad (3.2)$$

The discrete notation of the above integral leads to the following expression

$$f(\mathbf{r}_a) = \sum_b \frac{m_b}{\rho_b} f(\mathbf{r}_b)W(\mathbf{r}_b - \mathbf{r}_a, h), \quad (3.3)$$

in which m_b and ρ_b represent the mass and density at point b , respectively. h is the kernel support length which determines the maximum neighborhood radius. Consequently, it describes if two particles interact with each other or not. In general h must be slightly larger but in the order of the particles average distance for convergence purposes, see MONAGHAN (2005). In this work it is taken to be 1.5 times the average particles distance ($h = 1.5\Delta$). It must be noted that in equation (3.3) the $\frac{m_b}{\rho_b}$ has replaced $d\mathbf{r}'$ in the integral (equation (3.2)) which is nothing else than the volume element. In fact the value of f at point a is estimated using the values of its neighborhood. To find a similarity with FEM, one can imagine that the expression $\frac{m_b}{\rho_b}W(\mathbf{r}_b - \mathbf{r}_a, h)$ is like a "shape function" which is multiplied by the nodal

value $f(\mathbf{r}_b)$ and the summation is over all the nodes within the kernel support which looks like the element. Just like shape function, the kernel function has special properties in order to be able to reproduce the function f , properly. To know them let's start with the Taylor series of the function f around the point $\mathbf{r} = \mathbf{r}'$

$$f(\mathbf{r}) = f(\mathbf{r}') + (\mathbf{r} - \mathbf{r}') \frac{df}{dr} \Big|_{\mathbf{r}=\mathbf{r}'} + O(|\mathbf{r} - \mathbf{r}'|^2). \quad (3.4)$$

Multiplying the both sides of equation (3.4) by the kernel function W and integrating over Ω , it is easily deduced that the below condition must hold to have a first order accurate approximation of f

$$\int_{\Omega} W(\mathbf{r} - \mathbf{r}') d\mathbf{r} = 1, \quad (3.5a)$$

$$\int_{\Omega} (\mathbf{r} - \mathbf{r}') W(\mathbf{r} - \mathbf{r}') d\mathbf{r} = 0. \quad (3.5b)$$

Equation (3.5a) is in fact the "partition of unity" condition. In this case W is said to be "normalized". It can be shown that if the kernel function is "symmetric", ie $W(\mathbf{r} - \mathbf{r}') = W(\mathbf{r}' - \mathbf{r})$, then equation (3.5b) holds true. Additionally, since the W is to mimic the Delta function, it must be positive and approaches to Delta function in the limit as follows

$$W(\mathbf{r} - \mathbf{r}') \geq 0, \quad (3.6a)$$

$$\lim_{h \rightarrow 0} W(\mathbf{r} - \mathbf{r}', h) = \delta(\mathbf{r} - \mathbf{r}'). \quad (3.6b)$$

Now, similar steps need to be taken to make an approximation for the derivatives of the function f . Similar to equation (3.2) an approximation for the first derivative of f is

$$\nabla f(\mathbf{r}) \approx \int_{\Omega} \nabla f(\mathbf{r}') W(\mathbf{r}' - \mathbf{r}) d\mathbf{r}'. \quad (3.7)$$

Applying the integration-by-part rule and also the divergence theorem to convert the volume integral into a surface one, it is obtained

$$\int_{\Omega} \nabla f(\mathbf{r}') W(\mathbf{r}' - \mathbf{r}) d\mathbf{r}' = \int_{\partial\Omega} f(\mathbf{r}') W(\mathbf{r}' - \mathbf{r}) \mathbf{n} d\Gamma - \int_{\Omega} f(\mathbf{r}') \nabla W(\mathbf{r}' - \mathbf{r}) d\mathbf{r}'. \quad (3.8)$$

The first term in the right hand side vanishes, because W has a compact support and in fact it is equal to zero on $\partial\Omega$. Recalling the symmetricity of W which results in the identity $\nabla W(\mathbf{r} - \mathbf{r}') = -\nabla W(\mathbf{r}' - \mathbf{r})$, the final expression for the gradient approximation is as follows

$$\nabla f(\mathbf{r}) \approx \int_{\Omega} f(\mathbf{r}') \nabla W(\mathbf{r} - \mathbf{r}') d\mathbf{r}'. \quad (3.9)$$

Comparing equations (3.8) and (3.9), an important result needs to be stressed out that the key assumption for dropping the surface integral is either f or W must be zero on $\partial\Omega$. For example, if the continuum body (Ω_B) is finite (Ω_B and the $\partial\Omega$ is truncated by the body boundaries ($\Omega \cap \partial\Omega_B \neq \emptyset$), the surface integral must be taken into account. Figure (3.3) depicts such a situation.

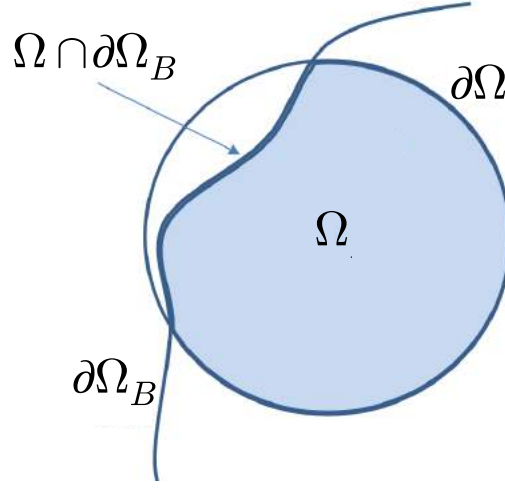


Figure 3.3. Kernel support Ω truncated by the body boundaries $\partial\Omega_B$

The discretized form of equation (3.9) is

$$\nabla f(\mathbf{r}_a) = \sum_b \frac{m_b}{\rho_b} f(\mathbf{r}_b) \nabla W(\mathbf{r}_a - \mathbf{r}_b, h). \quad (3.10)$$

Loosely speaking, one can say that equation (3.10) can be achieved from equation (3.3) by applying the gradient operator on the kernel function. Following the similar mathematical manipulation performed in equations (3.4)-(3.5a) and (3.5b) one can find that below conditions must hold true in order that the gradient of a function be approximated properly by the kernel gradient

$$\int_{\Omega} \nabla W(\mathbf{r} - \mathbf{r}') d\mathbf{r} = \mathbf{0}, \quad (3.11a)$$

$$\int_{\Omega} (\mathbf{r} - \mathbf{r}') \otimes \nabla W(\mathbf{r} - \mathbf{r}') d\mathbf{r} = \mathbf{I}, \quad (3.11b)$$

where \mathbf{I} denotes the identity tensor. It should be noted that equations (3.11a) and (3.11b) do not impose extra new conditions on W . As long as equations (3.5a) and (3.5b) hold true, it can be shown that equations (3.11a) and (3.11b) are inherently satisfied. To give more tangible interpretation, one can say that equations (3.11a) and (3.11b) account for having a consistency of the order C^0 and C^1 , respectively. It means that the gradient of a constant or linear function is interpolated properly. (The gradient of a constant function must be zero and that of a linear one is constant). For more discussion, the interested readers can refer to LIU (2003).

For the second derivative of f , instead of twice differentiating the integral interpolant, a much better approach was proposed by CLEARY & MONAGHAN (1999). The idea behind it is that an approximation for the second derivative is built similar to finite difference scheme, as follows

$$\nabla^2 f(\mathbf{r}_a) = \sum_b 2 \frac{m_b}{\rho_b} (f(\mathbf{r}_b) - f(\mathbf{r}_a)) \frac{(\mathbf{r}_b - \mathbf{r}_a) \cdot \nabla W(\mathbf{r}_a - \mathbf{r}_b, h)}{|\mathbf{r}_b - \mathbf{r}_a|^2 + \epsilon}, \quad (3.12)$$

in which ϵ is a small parameter to avoid singularity.

Considering that the maximum order of the derivative in most governing equations of physical phenomena is two, higher order derivatives are not required in practice.

Symmetrization of the discretized mathematical operators in SPH

The SPH expression for the first derivative of a function is first order accurate in its continuum form, see equation (3.9). Nevertheless in its discretized form, (equation (3.10)) it loses even the zero order consistency near the boundaries and also if the distribution of the particle is irregular, see VIGNJEVIC & CAMPBELL (2009). It means that equation (3.10) can not reproduce the derivative of a constant field, which must be equal to zero, exactly. Furthermore, the equation is not symmetric. This point is important from the physical point of view. The SPH discretized equations are translated finally into the inter-particle interactions. If it is intended to model a system of particles, any interaction between two particles must not violate the third law of Newton. Otherwise, the total angular or linear momentum is not conserved, see MONAGHAN (2005). In order to make the derivative operator symmetrized and exactly zero order consistent, one can use a differentiable test function ϕ in constructing the first derivative of the function f . Starting with the identity

$$\nabla f = \frac{1}{\phi}(\nabla(\phi f) - f\nabla\phi). \quad (3.13)$$

If now equation (3.10) is applied to the both terms of the right hand side of equation (3.13), one can obtain

$$\nabla f(\mathbf{r}_a) = \frac{1}{\phi_a} \sum_b \frac{m_b}{\rho_b} \phi_b (f(\mathbf{r}_b) - f(\mathbf{r}_a)) \nabla_a W(\mathbf{r}_a - \mathbf{r}_b, h). \quad (3.14)$$

Equation (3.14) vanishes if f is a constant function. Choosing $\phi = 1$ gives

$$\nabla f(\mathbf{r}_a) = \sum_b \frac{m_b}{\rho_b} (f(\mathbf{r}_b) - f(\mathbf{r}_a)) \nabla_a W(\mathbf{r}_a - \mathbf{r}_b, h). \quad (3.15)$$

Equation (3.15) is the practical and final version of the first derivative which is symmetric and exactly zero order consistent. It is obvious that in this equation, the effect of particle a on b is the same as that of b on a , but in the opposite direction. In the section (3.2) this equation is applied to discretize the continuity equation. In this case $f := v$.

Assuming $\phi = \frac{1}{\rho}$, one can write

$$\frac{\nabla f(\mathbf{r}_a)}{\rho_a} = \sum_b m_b \left(\frac{f(\mathbf{r}_b)}{\rho_b^2} + \frac{f(\mathbf{r}_a)}{\rho_a^2} \right) \nabla_a W(\mathbf{r}_a - \mathbf{r}_b, h). \quad (3.16)$$

This equation is utilized in section (3.2) for discretization of momentum equation in which the aim is to discretize the expression $\frac{\nabla \cdot \sigma}{\rho}$.

Kernel and kernel gradient renormalization

Recalling equations (3.5a) and (3.11.b), they hold true if and only if the support of the kernel function is complete. Near the boundaries of a finite body the condition of compact support fails. Hence the value achieved from the SPH interpolation is inaccurate. In such a condition, the kernel function and also its derivatives need to be re-normalized, see BONET (1999). In this work, for the reason which will be explained later in section 3.3.1, the corrective formula are not implemented in the code in simulating the solid and fluid phase. However, they are utilized just at the interface of the fluid and solid in order to calculate the coupling traction between the solid and fluid more precisely. It is worthwhile to know that such a corrective formula recovers the consistency of SPH up to first order. The corrected kernel \tilde{W} can be computed as follows

$$\tilde{W}(\mathbf{r}_a - \mathbf{r}_b, h) = \frac{W(\mathbf{r}_a - \mathbf{r}_b, h)}{\sum_b \frac{m_b}{\rho_b} W(\mathbf{r}_a - \mathbf{r}_b, h)}. \quad (3.17)$$

In equation (3.17) the denominator is equal to unity if the support is complete. The corrected kernel gradient can be derived in such a way that equation (3.11.b) is enforced as follows

$$\tilde{\nabla}W(\mathbf{r}_a - \mathbf{r}_b, h) = \mathbf{M}^{-1} \nabla W(\mathbf{r}_a - \mathbf{r}_b, h), \quad \mathbf{M} = \sum_b \frac{m_b}{\rho_b} \nabla W(\mathbf{r}_a - \mathbf{r}_b, h) \otimes (\mathbf{r}_a - \mathbf{r}_b). \quad (3.18)$$

The dimension of the matrix \mathbf{M} is 2 and 3 in 2D and 3D, respectively. A corrective formula has been proposed by FATEHI & MANZARI (2011) for the second derivative of kernel which is not applicable in this work.

Kernel function

A great amount of the literature has been dedicated to different types of kernels and their effect on the stability and accuracy of the solution. In MONAGHAN (2005) it has been discussed that how the error in the approximation depends on the Fourier transformation of the kernel. SWEGLE ET AL. (1995) related the tensile instability to a combination of the sign of the pressure and second derivative of the kernel. This instability will be discussed later in section (3.3.2). Numerous possibilities for kernel function exist in the literature ranging from polynomial to Gaussian. In spite of different mathematical description, they are all bell-shaped and meet the required condition discussed in section (3.2). In LIU & LIU (2010) a review about different kernels has been presented. According to MORRIS (1996) the general formula for the kernel function is

$$W(\mathbf{r}_a - \mathbf{r}_b, h) = \frac{1}{h^n} f\left(\frac{|\mathbf{r}_a - \mathbf{r}_b|}{h}\right), \quad (3.19)$$

where n is the dimension of the problem and h is smoothing length which is proportional to the particles average distance. In this thesis, the cubic spline proposed by MONAGHAN & LATTANZIO (1985) has been adopted, because it closely resembles the Gaussian kernel

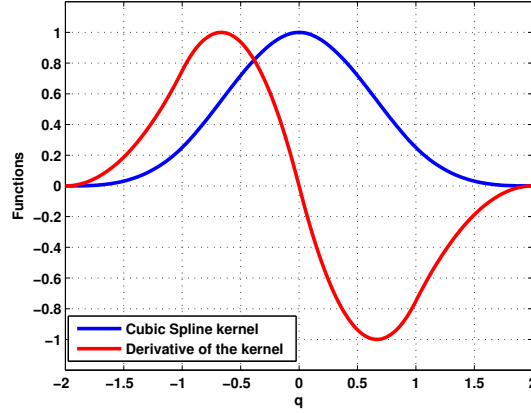


Figure 3.4. Cubic spline kernel and its first derivative divided by the factor α

while having a narrow support. The equation of the cubic spline is as follows

$$W(q, h) = \alpha \times \begin{cases} 1 - \frac{3}{2}q^2 + \frac{3}{4}q^3 & 0 \leq q < 1 \\ \frac{1}{4}(2 - q)^3 & 1 \leq q < 2, \\ 0 & q \geq 2 \end{cases} \quad (3.20)$$

where $q = \frac{|r_a - r_b|}{h}$ and α is equal to $\frac{10}{7\pi h^2}$ and $\frac{1}{\pi h^3}$ in 2D and 3D, respectively. Figure (3.4) demonstrates the plots of spline kernel and its first derivative.

Error estimation in SPH

It is not that straightforward to do an error estimation for the SPH method similar to that performed for grid-based method such as FEM. The reason is that the particles are always being disordered. However, it is important to know that the particles are not disordered randomly. In fact they get disordered based on the dynamics of the problem. This is a positive feature of SPH which ensures that the error is much more smaller than that is expected from probabilistic analysis such as Mont Carlo estimate. The reason is that in Mont-Carlo estimate the fluctuations are allowed to be completely random (even inconsistent with dynamics), while in SPH the particles movement is governed by dynamics, see MONAGHAN (2005). Nevertheless, assuming a regular distribution of the particles, one can make an acceptable error estimation.

There are several sources of error in SPH. Here we confine our attention to two significant roots of error, namely the ones arisen due to the integral interpolation and also those induced because of the discretization of integral in the form of a summation. The interested readers can refer to MONAGHAN (2005), FATEHI & MANZARI (2011) and VAUGHAN ET AL. (2008) for more details.

Error in the integral interpolant

For the sake of simplicity and without losing the generality, we focus on a 1D case. Starting

from the integral interpolation of a quantity A_I and using a kernel function W one can write

$$A_I(x) = \int A(\acute{x})W(x - \acute{x}, h)d\acute{x} = A(x) + \int (A(x) - A(\acute{x}))W(x - \acute{x}, h)d\acute{x}. \quad (3.21)$$

Now, the error can be estimated by a Taylor series expansion of $A(\acute{x})$ around x as follows

$$A(\acute{x}) = A(x) + (x - \acute{x})\frac{dA(\acute{x})}{d\acute{x}} + \frac{1}{2}(x - \acute{x})^2\frac{d^2A(\acute{x})}{d\acute{x}^2} + \dots \quad (3.22)$$

Since the kernel function $W(q, h)$ is an even function of q , by substituting equation (3.22) in (3.21) one can obtain

$$A_I(x) = A(x) + \frac{\sigma h^2}{2} \frac{d^2A(\acute{x})}{d\acute{x}^2} + \dots, \quad (3.23)$$

where σ is a constant depending on the kernel. It should be noted that the the integral term containing the first derivative of A vanishes, because the expression $(x - \acute{x})W(x - \acute{x}, h)$ is an odd function under the integral. The interpolation gets better if σ is zero and in such a case, a higher order term in the Taylor series appears. It is interesting that due to the symmetry of the kernel function (because, W is an even function of q), all the terms having odd order vanish. It means that if one uses a kernel as a result of which $\sigma = 0$ then the interpolation is accurate up to forth order. However, one needs to keep in mind that the error is larger near the boundaries, because the support of the kernel is not fully contained and the Taylor expansion is not valid anymore. To conclude, one can say that the SPH interpolation is at least second order accurate far from the boundaries.

Error in the summation interpolant

To evaluate mathematically the discretization error, the kernel function is assumed to be of the 1D Gaussian type with an infinite support, as follows

$$W(x, h) = \frac{1}{h\sqrt{\pi}} \left(\frac{3}{2} - \frac{x^2}{h^2} \right) e^{-\frac{x^2}{h^2}}. \quad (3.24)$$

All other types of kernels are similar to this, but they have a compact (finite) support. It means that for the Gaussian kernel the summation of SPH discretization are extended to infinity. A discretized summation can be converted into an integral form using the Poisson formula

$$\sum_{j=-\infty}^{\infty} f(j) = \int_{-\infty}^{\infty} f(j)dj + 2 \sum_{r=1}^{\infty} \cos(2\pi r j) f(j) dj, \quad (3.25)$$

where i is treated as a continuous quantity on the right hand side. To do an error estimation analysis of 1D SPH discretization, a linear function $g(x) = \alpha + \beta x$ is considered. The domain has been represented with a regular quasi-spaced array of particles with spacing parameter Δ along an infinite line. If the density is taken $\rho = 1$ the mass of each particle will be $m = \Delta$. Now the value of the function $g(x)$ at the sampling points $x_a = a/\Delta$ is computed using the SPH summation. One can write the following expression

$$\Delta \sum_{j=-\infty}^{\infty} (\alpha + \beta j \Delta) W(a\Delta - j\Delta). \quad (3.26)$$

If a change of variable is applied by shifting the origin to the point $x = a/\Delta$ and then the Poisson formulation is utilized, equation (3.26) reads

$$(\alpha + \beta\Delta)\left(\int_{-\infty}^{\infty} W(q, h)dq + 2 \int_{-\infty}^{\infty} \cos\left(\frac{2\pi q}{\Delta}\right)W(q, h)dq + \dots\right). \quad (3.27)$$

An interesting point can be inferred from equation (3.27). The error depends of the "Fourier transform" of the kernel. If the Gaussian kernel (see equation (3.24)) is used, equation (3.27) reads

$$(\alpha + \beta\Delta)\left(1 - 2e^{-\frac{\pi^2 h^2}{\Delta^2}} + \dots\right). \quad (3.28)$$

Equation (3.28) shows that, the SPH summation is not able to reproduce even a constant function ($\beta = 0$), exactly. However the error is exponentially small and is negligible if $h > \Delta$. If a cubic spline kernel is used instead of the Gaussian one, the discretized interpolated value of g is

$$(\alpha + \beta\Delta)\left(1 + 2\left(\frac{\sin\pi h/\Delta}{\pi h/\Delta}\right)^4 + \dots\right). \quad (3.29)$$

Equation (3.29) reveals that in case of cubic spline, the dominant error term vanishes exactly if $h = \Delta$ and small if $h > \Delta$.

Of the greater interest is the error in the derivative. It is obvious that $\frac{dg}{dx} = \beta$. If the SPH approximation of the derivative of $g(x)$ is calculated using equation (3.15) and then the variable shifting and Poisson formula are applied similar to the procedure which was followed in equation (3.27), one can obtain

$$\frac{dg}{dx} = \beta\left(1 - \int_{-\infty}^{\infty} q \frac{\partial W}{\partial q} \cos\left(\frac{2\pi q}{\Delta}\right) dq + \dots\right). \quad (3.30)$$

It can be realized from equation (3.30) that the error in the derivative evaluation depends on the Fourier transformation of the kernel gradient. In case of Gaussian kernel the error is again exponentially small for $h < \Delta$.

To sum up this section, it is concluded that the error estimation of SPH approximation can be done provided that the particles are regularly positioned in an infinite space. The extension of this analysis to two and three dimensions is quite straightforward. However, a general error estimation in case of disordered particles is still missing in the literature and needs more investigation. The reason is that the disorder depends on the dynamics in SPH and hence the traditional probabilistic error estimation procedures can not be applied to that. In practice, the accuracy of SPH is validated against benchmark known solutions or experiments.

3.2 Discretization

3.2.1 Initial particles distribution (meshing)

Unlike the grid-based methods such as FEM for which robust mesh generator tools has been developed, such tools are missing in SPH. Although a simple geometry can be represented easily using particles (point clouds), it is not the case for complex geometries. In other words, creating the initial particles distribution is generally a challenge in SPH. One may

think about employing mesh generator tools in order to create initial points. For example, the generated nodes by an FEM mesh generator can be regarded as the initial points for SPH. Another choice can be the centroid of the generated elements, see for example GANZENMULLER (2015). Such methods result in an irregular point distribution in general and this can be problematic in SPH. The fact is that an irregularly distributed point may be used, but with extreme carefulness. The reason is that in SPH, a volume and finally a mass is assigned to each particle. The volume occupied by each particle is indeed a function of the average particles distance at the point of interest. If the volume of the particles are not accurate the normality condition is not fulfilled properly, see equation (3.3). This deteriorates the SPH results. That is why most SPH codes uses a regularly placed particles as the initial particle condition. In such a lattice the initial volume for all the particles is the same and a function of the lattice cell length.

An important point that needs to be clarified is that, even an initially regular particle distribution becomes irregular as the SPH solver proceeds. The question is that what is the difference between such irregularity and the initial irregular particle distribution. Maybe the most beautiful answer to this question is a quote from MONAGHAN (2005) saying "in SPH particles are disordered but orderly!". The reason is that the density and consequently the volume of the SPH particles change through time in such a way that they are in compatibility with the particles distribution. Because, the particles position is updated by the velocity which is governed by the mass and momentum balance.

Now the question is that among several possible regular lattice, which ones are optimal. Here it is not intended to go through this subject in detail and a concise discussion is provided to give an insight to it. The readers seeking more details may refer to DIEHL ET AL. (2008). The simplest and most favored method for initial particle generation is the so-called simple cubic lattice. In this method the particles are placed in a rectangular arrangement in each direction. This lattice has proven to be "unstable" if a perturbation is applied to the equilibrium state. Furthermore it has strong "preferred directions", see LOMBARDI ET AL. (1999). Other lattice types such as hexagonal closed pack are stable in the presence of a perturbation. However, the neighbors number for each particle is relatively larger in these lattices and this leads to more computational effort. In DIEHL ET AL. (2008) a comparative study on different lattices has been done. Figure (3.5) illustrates the simple cubic lattice and hexagonal closed pack arrangement.

In this work, the hexagonal closed packing lattice has been adopted due to its satisfactory properties. It is geometrically more homogenous (no preferred direction) and also uniform enough to reduce the noise level while possessing acceptable accuracy in the interpolation. Furthermore, implementing the associated algorithm is straight forward even it needs more effort in comparison to simple cubic lattice. In this work the pre-processor unit which creates the initial point cloud has been implemented in MATLAB.

Assuming that the problem geometry has been represented using an appropriate lattice, we can proceed with discretizing the governing equations derived in chapter (2).

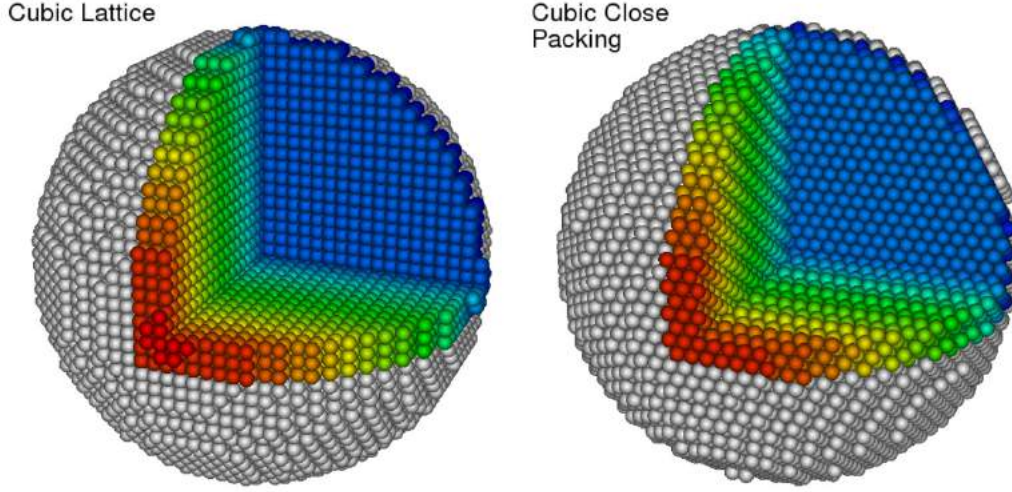


Figure 3.5. simple cubic vs. hexagonal closed pack lattice, from DIEHL ET AL. (2008)

3.2.2 Discretization of the mass balance (continuity) equation

Taking the source term into account and recalling equation (3.15), SPH discretization of mass balance equation follows

$$\frac{\partial \rho_a}{\partial t} = \sum_b m_b (\mathbf{v}_a - \mathbf{v}_b) \cdot \nabla_a W(\mathbf{r}_a - \mathbf{r}_b, h) + \gamma_a, \quad (3.31)$$

where ∇_a is an abbreviation for $\frac{\partial}{\partial \mathbf{r}_a}$. Equation (3.31) has been implemented for the fluid flow. Nevertheless, another version of the continuity equation which is equivalent to equation (3.31) has been employed for the biofilm compartment in which the growth process occurs, see LIBERSKY ET AL. (1993). This version of the mass balance equation is as follows

$$\rho_a = \sum_b m_b W(\mathbf{r}_a - \mathbf{r}_b, h). \quad (3.32)$$

The reason behind this adoption is that the growth process is driven in fact by the internal local density accumulation rather than external forces. Both equations, (3.31) and (3.32), theoretically must give identical results except at boundaries, see LIBERSKY ET AL. (1993). It was found by the authors that equation (3.32) is much more suitable for the numerical scheme utilized here to handle the growth process. In this thesis the growth process is in fact a density relaxation taking place once the new mass is generated due to the reaction term leading to a local density accumulation. As a result, the biofilm expands and this expansion in particles distribution is reflected in more relative distances between the particles and that is exactly the spirit of equation (3.32) which is explicitly a function of particle distribution rather than particles velocity. It should be highlighted that this approach was inspired by a seemingly irrelevant work to this research, see BOFFIN & ANZER (1994), in which astrophysical gravitational wind accretion has been simulated using the SPH method with particles whose masses are varying.

3.2.3 Discretization of the momentum balance equation

The SPH approximation of equation (2.32) is obtained using equation (3.16) as follows

$$\frac{D\mathbf{v}_a}{Dt} = \sum_b m_b \left(\frac{\boldsymbol{\sigma}_a}{\rho_a^2} + \frac{\boldsymbol{\sigma}_b}{\rho_b^2} - \Pi_{ab}\mathbf{I} + \mathbf{R}_{ab} \right) \nabla_a W(\mathbf{r}_a - \mathbf{r}_b, h) + \mathbf{f}_a, \quad (3.33)$$

where $\Pi_{ab}\mathbf{I}$ (with \mathbf{I} being the identity tensor) and \mathbf{R}_{ab} are tensors corresponding to the artificial viscosity and artificial stress terms, respectively. They are intentionally introduced to the momentum equation for stability reasons. They will be discussed in section (3.3) in detail. \mathbf{f}_a denotes the external force (body or surface) applied to the particle "a". The computation of \mathbf{f}_a will be discussed in section (3.3).

3.2.4 Discretization of the diffusion-advection-reaction equation

The discretized form of equation (2.29) is represented as follows using equation (3.12).

$$\frac{DC_a}{Dt} = \sum_b 2D \frac{m_b}{\rho_b} (C_b - C_a) \frac{(\mathbf{r}_b - \mathbf{r}_a) \cdot \nabla W(\mathbf{r}_a - \mathbf{r}_b, h)}{|\mathbf{r}_b - \mathbf{r}_a|^2 + \epsilon} + \frac{\gamma_a}{Y}. \quad (3.34)$$

3.2.5 Discretization of the constitutive equations

Referring to equations (2.9)-(2.13), in order to calculate the stress (for fluid) or stress rate (for the solid) tensor, one needs to compute two values. First, the strain rate tensor (equation (2.37)) and spin tensor (equation (2.38)). Second, the pressure. The formers are functions of velocity gradients which can be evaluated as follows

$$\left(\frac{\partial v_i}{\partial x_j} \right)_a = \sum_b \frac{m_b}{\rho_b} ((v_i)_b - (v_i)_a) \cdot \frac{\partial W(\mathbf{r}_a - \mathbf{r}_b, h)}{\partial x_j}. \quad (3.35)$$

In the standard SPH which is also called weakly compressible SPH (WCSPH), the pressure is computed from the density using a thermodynamically consistent equation of state. Such an approach enjoys the benefit of decoupled pressure and velocity field, but suffers from a small time step that is conversely proportional to the sound velocity in the material due to the CFL (Courant, Friedrichs and Levy 1928) stability condition. Here the following equation for the pressure is used

$$p_a = \frac{c_0^2 \rho_0}{\gamma} \left(\left(\frac{\rho_a}{\rho_0} \right)^\gamma - 1 \right), \quad (3.36)$$

where c_s and ρ_0 are sound velocity and rest density of the bulk material. The parameter γ is set to be "7" for the fluid and "1" for the solid. It should be emphasized that the value of c_0 for the fluid is in fact a penalty parameter rather than a true physical sound speed and hence it can be selected in a way that is large enough to insure density fluctuation less than 0.01 and keep the Mach number less than 0.1, and small enough to avoid unnecessary small time steps, see MONAGHAN (2005). In practice, if c_0 is taken at least 10 times the maximum

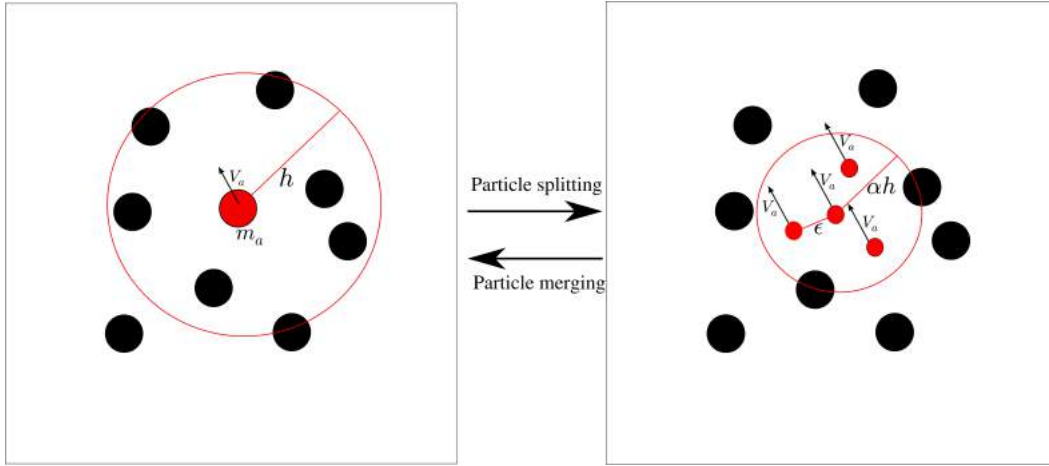


Figure 3.6. Particle refinement (spitting) and coalescence (merging) pattern

velocity, it is sufficient, see ADAMI ET AL. (2012). Nevertheless, for the solid it is a real material constant related to the bulk modulus(K) and density(ρ) according to

$$c_0 = \sqrt{\frac{K}{\rho}}. \quad (3.37)$$

3.2.6 Particles coalescence and splitting (re-meshing)

The concept of variable resolution in mesh based methods, especially the Eulerian ones, has been developed successfully. It is known as the non-uniform meshing and re-meshing techniques. Different resolution in the domain of interest is significantly advantageous. One can increase the accuracy wherever it is really necessary. This is more efficient in terms of computational cost. Nevertheless, extending this concept to Lagrangian mesh-less methods such as SPH is in the early stages of development. One important reason which hinders its progress is that any intervention in the particle arrangement influences the governing equations strongly. Because, the particles themselves are carrying important quantities like mass, momentum and energy. It means that any change in the particle pattern must be in such a way that insure the 'minimum possible change' in important physical quantities. Of course, this issue exists in the Eulerian methods as well, when one projects the quantities from one mesh to the new one. So, the objective is to find systematic algorithms by which one can benefit from variable resolution while conserving the fundamental properties of the system. It means that any ad-hoc procedure like new particle insertion, particle removal, particle coalescence and splitting, needs to be carefully pondered and it has something more than solely "particles manipulation".

The motivation for employing such adaptive re-meshing techniques is to reduce the computational cost by using a rough mesh in the regions where the gradient of the quantities are relatively small. Such regions are normally of less interests. To make it more clear, two examples are provided. First in a fluid solid interaction problem, the fields variables such as pressure and velocities must be accurate enough at the interface through which the solid and fluid interact. But in the regions far away from the interface where the fluid flow has a simple

stream pattern, a rough mesh (more distance between the particles) is sufficient. Another example, is relevant to the growth process. As the biofilm grows, the material expands and it is reflected in more distance between the particles. In this case, the more the growth proceeds, the more rough the mesh becomes and the less accurate the results are. In other words, one needs to increase the number of particles in order to keep the accuracy of the method.

To the best of the author's knowledge, the algorithm introduced in VACONDIO ET AL. (2013) is the most matured and robust. The basic idea is that a dynamic refinement is realized by replacing a "mother particle" with several "daughter particles" in the regions where one wants to refine the mesh. This can be regarded as a "particle splitting". Conversely, several particles are substituted with a single particle in order to obtain a region with a more rough mesh. This process is also referred as "particle coalescence (merging)" in the literature. Figure (3.6) shows schematically the refinement pattern in 2D. It is important to know that daughter particles have the same velocity as their mother particle. The mass of the mother particle is divided equally among the daughters. Additionally the arrangement of the daughter particles are symmetric with respect to the original position of their mother. These assumptions, ensure the conservation of mass and both linear and angular momentum, see VACONDIO ET AL. (2013). One can intuitively understand that. Nevertheless, an error occurs in local density evaluation due to the introduced perturbation in the particle configuration, see equation (3.3). The main idea is to find the two parameters α and ϵ in such a way that the error in density estimation is minimized. α and ϵ correspond to the scaling parameters for the new smoothing length and particles separation, see figure (3.7).

It should be noted that there are several possibilities for particles arrangement while maintaining the symmetry. For example in 2D, a mother particle can be replaced by 4 particles in a rectangular arrangement or 7 in a hexagonal lattice, see figure (3.7).

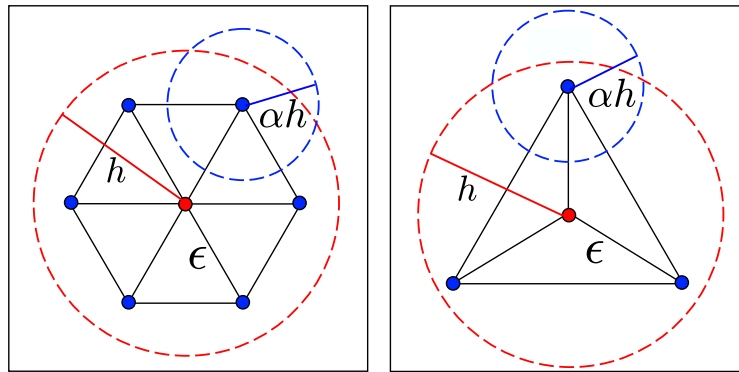


Figure 3.7. Two different daughter particles patterns in 2D, right: triangle pattern, left: hexagonal pattern

In FELDMAN (2006) a comprehensive comparative study has been performed for finding the optimum parameters α and ϵ in 2D and 3D cases using different possible particles arrangement. It was reported that $\alpha = \epsilon = 0.6$ with hexagonal lattice arrangement (7 and 13 daughter particles in 2D and 3D, respectively) results in a minimum error less than 5 percent.

3.3 Implementation

In this section, some practical discussions for handling the coupling between the fluid and biofilm, interface treating and numerical stabilization are provided. Furthermore, the numerical time integration method is introduced.

3.3.1 Boundary conditions and fluid-solid interaction implementation

Fluid phase

The treatment of the boundary conditions in SPH is still a controversial issue and not fully solved. It is still defined as one of the four grand challenges of the SPHERIC (SPH European Research Interest Community). The reason stems from the nature of SPH as a collocation method based on the strong form of the governing equations, see LIU (2003), LI & LIU (2002). The completeness condition which means consistency of the method fails at boundaries where the kernel of smoothing function is truncated, see LIU & LIU (2003). The objective of any treatment is to provide an accurate boundary interaction between the fluid and solid to avoid non-physical penetration. Several techniques have been proposed which are based on one of three basic concepts. First, to use some imaginary particles at the boundaries. This method is called "dynamic boundary condition" or "Dalrymple boundary condition", see DALRYMPLE & KNIO. These particles are forced to satisfy all equations as fluid particles but their movement is externally prescribed. Another version of such "auxiliary particles" is called image particles. This approach has more geometrical complexity in terms of that the generation of these particles is performed dynamically by mirroring the fluid particles with respect to the wall boundary, see MORRIS ET AL. (1997). Second, introducing predefined repulsive forces, see MONAGHAN & KAJTAR (2009), into the fluid particles near the boundaries in order to prevent them from penetrating into the solid wall. The third method is to derive corrective formula for the kernel and kernel gradient at free boundaries where the kernel support does not have sufficient neighbors, see BONET (1999). It should be stressed that in this thesis the corrective formula for kernel gradient near free boundaries are not implemented because such a formula fail to meet the requirements accounting for conservation of the linear and angular momentum even they provide more accurate results in short terms, see VAUGHAN ET AL. (2008).

It should be expressed that the method presented in ADAMI ET AL. (2012) has been employed in this work. This method has been appreciated as a plausible, accurate and stable method by Monaghan, one of the first developers and pioneers of SPH, see VALIZADEH & MONAGHAN (2015). The main essence of this approach is to consider three layers of solid particle to be dummy (wall) particles through which the pressure and velocity fields of the fluid are extrapolated. Presence of such dummy particles not only removes the issue of truncated kernel support but also provides consistent repulsive force avoiding unphysical penetration. Figure (3.8) depicts the arrangement of dummy wall particles at the boundary of the fluid. At first glance, the method introduced in ADAMI ET AL. (2012) is apparently similar to Dalrymple method in that they both use dummy particles replacing the solid boundaries. However, it has been found that the Dalrymple boundary condition results in oscillatory pressure field near the boundaries, although it can address the penetration issue well. In the new

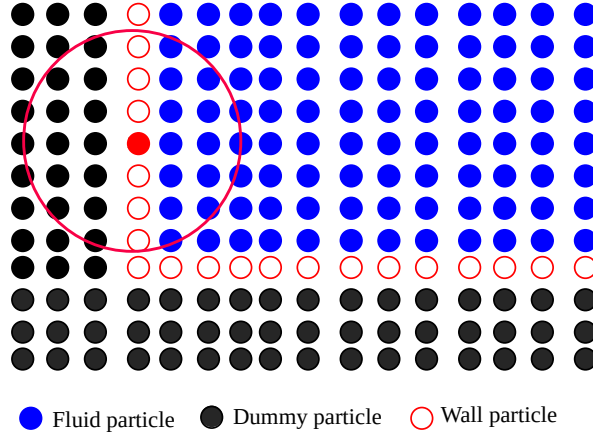


Figure 3.8. Dummy particles for boundary treatment

method, the way that the field variables for the dummy particles are calculated is based on a local force balance near the boundary. Hence, the field variables at the boundary particles are consistent with those of internal fluid particles and the solution is stable without unphysical oscillations. To introduce the method, we start with the Navier Stokes equation for the fluid close to the solid boundaries (dummy particles), neglecting the viscous term

$$\mathbf{a}_f = \frac{d\mathbf{v}_f}{dt} = -\frac{\nabla p}{\rho} + \mathbf{g}, \quad (3.38)$$

in which the index "f" refers to the fluid phase and \mathbf{a}_f is the acceleration of fluid particles near the wall. The key assumption is that we have a no-slip boundary condition and it entails the continuity of the acceleration at the boundary ($\mathbf{a}_f = \mathbf{a}_w$). Rearranging equation (3.38) and integrating along a line connecting the fluid particle to a wall particle, yields

$$\int \nabla p \cdot d\mathbf{l} = \rho_f \int (\mathbf{g} - \mathbf{a}_w) \cdot d\mathbf{l}. \quad (3.39)$$

The novelty of this method is the incorporation of the wall acceleration into the pressure calculation of the dummy particles. The point is that It is not an ad-hoc formula, but rather it comes from the momentum balance at the boundaries. Expressing equation (3.38) using SPH discretization, one can find the final formula for computing the pressure in dummy particles

$$p_w = \frac{\sum_b \frac{m_b}{\rho_b^f} p_b^f W_{ab} + (\mathbf{g} - \mathbf{a}_w) \cdot \sum_b \frac{m_b}{\rho_b^f} \rho_b^f \mathbf{r}_{ab} W_{ab}}{\sum_b \frac{m_b}{\rho_b^f} W_{ab}}. \quad (3.40)$$

Here p_w and p_b^f are wall (dummy) and fluid pressure, respectively. Besides, W_{ab} and \mathbf{r}_{ab} are short notations for $W(\mathbf{r}_a - \mathbf{r}_b, h)$ and $\mathbf{r}_a - \mathbf{r}_b$, respectively. Pondering on equation (3.40), one can say that the body force and solid wall acceleration play important roles in the pressure value of the dummy particles. The effect of these two is added to the value which is calculated using a simple extrapolation of pressure field.

The density of the dummy particles are computed using the inverse of equation of the state

(equation (3.36)) as follows

$$\rho_w = \left(\frac{p_w}{\rho_0 c_0^2} + 1 \right)^{\frac{1}{\gamma}}. \quad (3.41)$$

In addition to the pressure, the velocity of the dummy particles are needed to be determined. Again, with the assumption of no-slip condition, one can write

$$\mathbf{v}_w = 2\mathbf{v}_s - \frac{\sum_b \frac{m_b}{\rho_b^f} \mathbf{v}_b^f W_{ab}}{\sum_b \frac{m_b}{\rho_b^f} W_{ab}}, \quad (3.42)$$

where \mathbf{v}_w , \mathbf{v}_b^f and \mathbf{v}_s are wall (dummy), fluid and solid particle velocities, respectively. Comparing to the method presented in MORRIS ET AL. (1997), this approximation is less accurate than that. The advantage is that the geometrical computation of the tangent of interface profile is not involved in it and hence the implementation, especially for complex geometry, is straight forward. Equation (3.42) has been defined in such a way that insures the impermeability of the solid boundary. Indeed, the assigned velocity to the dummy particles is a mirrored velocity of the fluid around the boundary. To examine the validity of this equation intuitively, one may consider to special cases. In the case that the solid boundary

is stationary ($\mathbf{v}_s = 0$) equation (3.42) is reduced to $\mathbf{v}_w = -\frac{\sum_b \frac{m_b}{\rho_b^f} \mathbf{v}_b^f W_{ab}}{\sum_b \frac{m_b}{\rho_b^f} W_{ab}}$ which means that the velocities of dummy particles are equal to those achieved from an extrapolation using fluid particles, but in an opposite direction (mirror). In the case that both fluid and solid move with the same velocity ($\mathbf{v}_s = \mathbf{v}_b^f$) equation (3.42) gives the expectable results meaning $\mathbf{v}_w = \mathbf{v}_s$.

Important remark: Knowing the value of the pressure and velocity of the dummy particles, they are taken into account in equations (3.31) and (3.33) for fluid phase. But one must be careful that the dummy particles in reality are 3 layers of solid particles and it means that they move according to the governing equations of the solid phase. In other words the summation of SPH in fluid phase is extended to the solid particles which play the role of dummy particles. Furthermore, one should keep in mind that the solid particles with dummy identity contribute in equations (3.31) and (3.33) with their "dummy value" of pressure and velocity, not their real value which comes from solid phase.

Solid phase

In the previous section, the effect of the solid on the fluid and the way how to numerically treat it, was discussed. Now we intend to incorporate the effect of the fluid on solid phase. Recalling equations (2.33b), a solid will experience an effective traction from the fluid around. Such a traction serves as a Neumann boundary condition for the solid phase. From equations (2.34)-(2.36) and neglecting the divergence of velocity due to incompressibility, one can obtain an expression for the traction applied to the solid from fluid side, as follows

$$\mathbf{t}_s = \boldsymbol{\sigma}_f \cdot \mathbf{n} = (-p\mathbf{I} + \frac{1}{2}\mu_f(\nabla\mathbf{v} + \nabla^T\mathbf{v})) \cdot \mathbf{n}, \quad (3.43)$$

in which \mathbf{n} is the normal vector to the current configuration of the solid boundary. Here an amazing superiority of SPH shows up. Due to its updated and Lagrangian features no mapping of equation (3.43) is needed. If an ALE approach were employed, a mapping between Eulerian description of the right hand side (fluid phase) and Lagrangian description of left hand side (solid phase) would be required, see HUGHES ET AL. (1981). Furthermore, due to the explicit nature of SPH, no linearization of interface relations is involved. The interface force due to the pressure is always normal to deformed surface of biofilm (it is so-called follower load). Such a deformation dependent traction at the boundaries, in methods like FEM poses numerical challenges and makes the stiffness matrix non-symmetric WRIGGERS (2008).

The discretized form of each part of equation (3.43) is

$$p_a^s = \sum_{b \in \Omega_f} \frac{m_b^f}{\rho_b^f} p_b^f \tilde{W}_{ab} \approx 2 \sum_{b \in \Omega_f} \frac{m_b^f}{\rho_b^f} p_b^f W_{ab}, \quad (3.44a)$$

$$\mu_f (\nabla \mathbf{v} + \nabla^T \mathbf{v})|_{for\ a} = \sum_{b \in \Omega_f} \mu_f \frac{m_b^f}{\rho_b^f} (\mathbf{v}_b^f - \mathbf{v}_a^s) \tilde{\nabla}_a W_{ab}, \quad (3.44b)$$

$$\mathbf{n} = \frac{\mathbf{N}}{\|\mathbf{N}\|}, \quad \mathbf{N} = \sum_{b \in \Omega_s} \frac{m_b^f}{\rho_b^f} \nabla_a W_{ab}. \quad (3.44c)$$

In equations (3.44a)-(3.44c) the index "f" and "s" refer to the fluid and solid phase, respectively. It should be notified that the SPH summation is applied to the fluid particle at the interface. This is the reason why the computation is performed using the corrected kernel (\tilde{W}) and corrected kernel gradient ($\tilde{\nabla}W$). It has been found that equation (3.44a) works better if the denominator of equation (3.17) is replaced by 0.5 for all configuration of truncated kernel, see ANTOCI ET AL. (2007). The reason is that this approximation introduces a smoothed transient region from maximum value to zero at the interface. In other words, dummy particles which are positioned in three layer, are subjected to the traction, smoothly. The outermost layer experience the maximum value and the traction on the innermost one tends to zero. The vector \mathbf{n} is calculated using the updated (current) configuration of the solid particles. Equation (3.44c) is in fact a fantastic property of the kernel gradient in computing the normal direction of the surface constructed by an assembly of the nodes. To examine This property more deeply, see figure (3.9). As discussed in section (3.2), if the support of a particle is fully contained by solid neighbors, the expression $\sum_{b \in \Omega_s} \frac{m_b^f}{\rho_b^f} \nabla W_{ab}$ is equal to zero. But in the case that the Ω is truncated by the boundary, using the divergence theorem one can write

$$\int_{\Omega \cap \Omega_s} \nabla W dv = \int_{\partial \Omega \cap \Omega_s} W \mathbf{n} ds + \int_{\partial \Omega_s \cap \Omega} W \mathbf{n} ds. \quad (3.45)$$

The first term in the right hand side of equation (3.45) is zero, because $W = 0$ on $\partial \Omega$. The second term of the right hand side is nothing else than an average of normals of solid boundary particles around the point of interest which lie within the support.

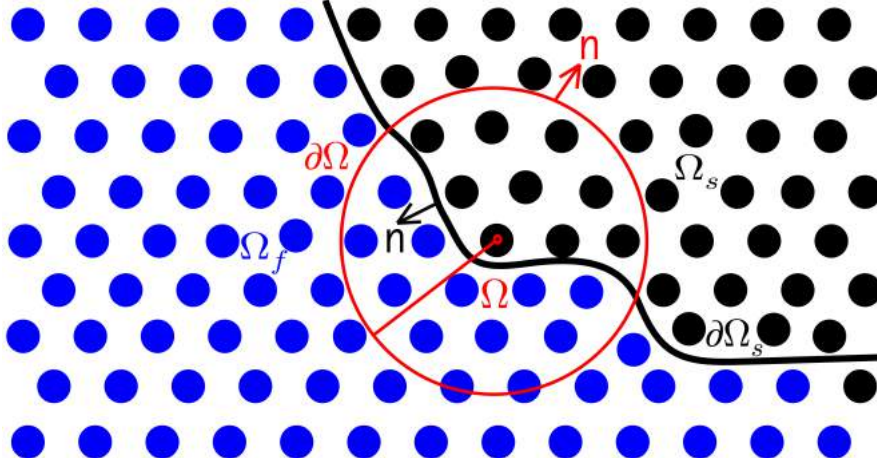


Figure 3.9. Boundary condition for the solid phase

Now, the total forces per unit mass exerted on a solid particle from the fluid side, $\mathbf{F}_{f \rightarrow s}$ can be computed

$$\mathbf{F}_{f \rightarrow s} = \frac{\mathbf{t}_a^s \left(\frac{m_a^s}{\rho_a^s} \right)^\beta}{m_s^a}, \quad (3.46)$$

where the $\left(\frac{m_a^s}{\rho_a^s} \right)^\beta$ is in fact the area associated to a particle. β is taken $\frac{1}{2}$ and $\frac{2}{3}$ for 2D and 3D, respectively to give an estimation of the area of each particle. Note that in the solid phase, the force calculated using equation (3.46) is added explicitly to the right hand side of momentum equation (equation (3.33)), and the SPH summation is extended only to the solid particles, whereas in the fluid phase the SPH summation includes dummy wall particles and no such explicit term is added to the momentum equation. In fact, the velocity and pressure of dummy particles, which in reality belong to the solid phase, contribute to the reaction force applied to the fluid from the solid.

Fluid-solid coupling procedure

It is true to say that interface modeling plays a crucial role in an FSI problem (fluid-solid interaction). It can affect the output significantly. The more accurate the interface quantities are computed, the more correct the fluid-solid coupling is modeled and consequently more realistic and physically sound results are achieved. In this work, it is not intended to go through all different methods and approaches proposed to tackle the FSI problems. The interested readers may refer to the literature. But some basic concepts need to be known to understand the procedure which has been implemented in this work. Generally speaking, there are two categories for the methods applied to FSI. First, monolithic approach in which the fluid and solid are advanced simultaneously in a fully coupled fashion. The interfacial conditions are treated implicitly in the solution procedure. Second, partitioned (staggered) method in which the fluid and solids are stepped separately and successively. In this case coupling is realized through "data communication" in the context of prediction, substitution and synchronization techniques. It should be noted that depending on whether the solver of the fluid or solid is explicit or implicit, there are different combinations each of which

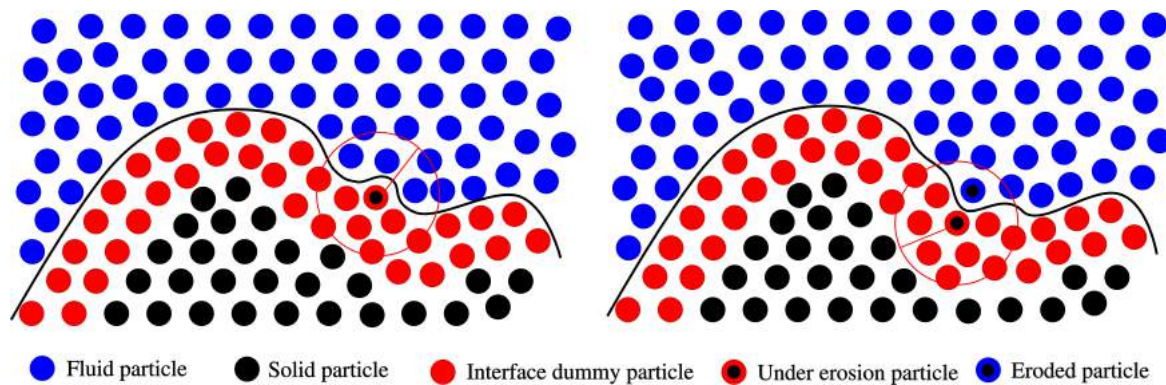


Figure 3.10. Interface modification due to erosion, left) before erosion, right) after erosion

has its own merits, see BELYTSCHKO (1977). The staggered method has the advantage of using existing robust solver for fluids as well as solids. Making the whole system partitioned adds a flavor of explicit into the system although each of the fluid or solid is handled implicitly. That is why such methods, especially when there is not enough sub-iteration, have stability issues. For example it has been found that the simulation of very "light" structure surrounded by "heavy" fluids are problematic, see BAZILEVS ET AL. (2008). As another example, the problems in which the "added mass effect" is significant due to the incompressibility of the fluid, are more likely prone to instabilities, see CAUSIN ET AL. (2005). The interested readers are referred to FELIPPA ET AL. (2001) for a comprehensive overview about the advantages and drawbacks of partitioned method. The most important point in the interface of the fluid and solid, aside from the method chosen, is that the interface modeling must be "energy conservative". It means that neither artificial energy should be injected into the system nor unphysical damping should dissipate the energy, see PIPERNO & FARHAT (2001), PIPERNO ET AL. (1995). It has been found that partitioned methods are inherently non-conservative, see VAN BRUMMELEN ET AL. (2003).

It should be reminded that SPH is naturally an explicit method for both fluids and solids. As an explicit method, the time step is governed by Courant condition. In this work, the coupling of the fluid and solid has been implemented in a monolithic way in order to have a strong two way coupling. In terms of computational cost, using a monolithic SPH based (explicit) method for FSI problems is justified, if the elastic modulus of the solid is in the order of the fluid bulk modulus (It is assumed that they have similar densities). It means that applying SPH to FSI problems is computationally efficient, if the characterized time scale of fluid and solid are of the same order, otherwise use of SPH is not recommended because a much smaller time step is associated with the stiff solid and hence it rules the whole process. In this Thesis, fortunately the biofilm is a soft material with elastic modulus in the order of several Pa and Poisson ratio not close to 0.5 BÖL ET AL. (2009). In case of a fully incompressible solid (for example rubber like materials) whose Poisson ratio approaches the limit 0.5, the bulk modulus tends to infinity and using this approach is unjustifiable. Some authors have shown that an artificial decrease in the bulk modulus (or Poisson ratio) can be a remedy for this issue, while not affecting the results that much. In this case, the material is allowed to behave nearly incompressible, see ANTOCI ET AL. (2007).

Erosion and interface up-dating

In section (2.3.5), the mathematical modeling and fundamental assumptions of the erosion process were discussed. To implement the erosion process, first we need to calculate the shear stress applied by the fluid to the solid particles at the interface, as follows

$$\boldsymbol{\tau}_{interface} = \sum_{b \in \Omega_f} \mu_f \frac{m_b^f}{\rho_b^f} (\mathbf{v}_b^f - \mathbf{v}_a^s) \nabla_a W_{ab}. \quad (3.47)$$

The particle is detached if the shear stress exceeds the strength of the material according to equation (2.39). Once the particle is removed from the solid phase, it is converted to a free (planktonic) one floating in the fluid and moves with the fluid. In planktonic state, the particle is subjected to its own weight and drag forces applied from the fluid. It should be noted that the movement of a planktonic particle is governed by the rigid body equations of motion for a mass point. In other words, the deformation of a single particle (mass point) is irrelevant and meaningless in planktonic state. If one wishes to capture the deformation of a single particle, it entails resolving the fluid solid interaction in a smaller length scale. As a Lagrangian method, SPH can handle the interface of a solid automatically and no interface tracer method, for example level set method, is needed to be employed. However, when the material removal occurs and consequently some parts of the material belonging to the interface are excluded, one should modify the interface. It should be reminded that the interface is in fact up to 3 layers of boundary solid particles which play the role of dummy particles for the fluid. If the detached particle from the interface is not replaced properly by the inner particles, the kernel support of the fluid particles near the boundary will be incomplete. This results in poor estimation of the interfacial forces, unphysical penetration and finally crash of the numerical scheme. An effective algorithm has been embedded in the code whose task is to modify the interface layers, once the erosion takes place. Figure (3.10) illustrates the concept behind that.

Periodic boundary condition

In this work, it is assumed that the boundary condition is periodic on the lateral sides of the RVE (see figure (2.1)). This means that the RVE repeats itself infinite number of times and the geometrical and physical condition of the opposite lateral sides are the same. The assumption of periodicity has the advantage of being computationally efficient. Because as soon as a particle leaves the RVE from one side, it enters the opposite side and there is no need for having a pool of particles to feed continuously the inlet of the RVE. Furthermore, the implementation of periodic boundary condition in SPH is much more straight forward than inlet/outlet boundary condition, see ARISTODEMO ET AL. (2015). Figure (3.11) reveals the simple idea behind the periodic boundary condition concept in SPH. In fact the particles near the lateral side interact with the complementary particles near the opposite side. In other words, in a periodic boundary a truncated kernel support is completed using the particles of the opposite side. This makes both inlet and outlet have the same physical condition such as velocity, stress and pressure.

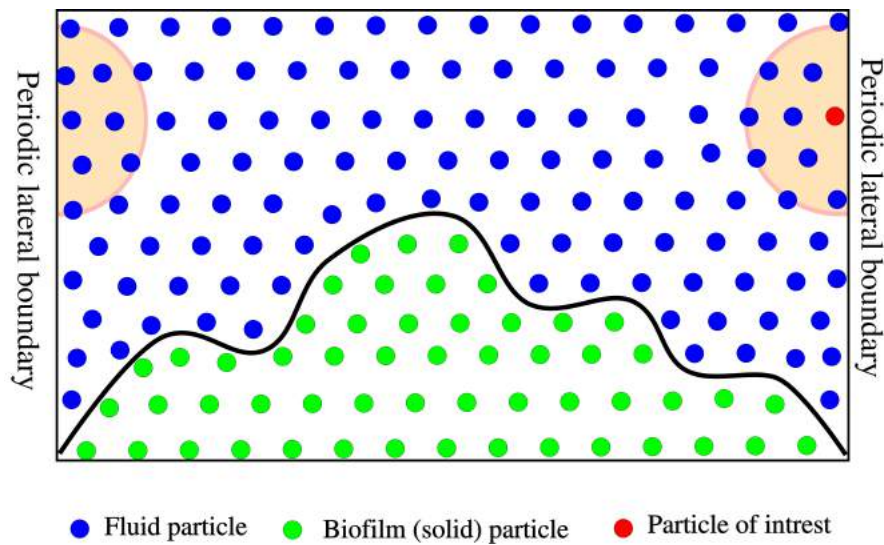


Figure 3.11. Periodic boundary condition

3.3.2 Numerical challenges and remedies

In spite of its robustness and simple appearance, SPH like any other computational method has some shortcomings. A great deal of literature has been dedicated to identify and remedy such issues. Some problems like "zero energy modes" are common in all numerical methods. For example in FEM this issue manifests itself in "hour-glassing". Such numerical pathologies originate from the "rank deficiency" in the linear algebraic equations corresponding to the discretized system and results in the non-uniqueness of the solution from the mathematical point of view, see GANZENMLLER (2015). Another weakness from which SPH suffers is the "tensile instability", see SWEGLE ET AL. (1995). It is unique to co-locational meshless methods such as SPH. Furthermore, some issues like "completeness" influence strongly the convergence. Completeness in SPH is equivalent to "consistency" in finite difference approximation, see BELYTCHKO ET AL. (1998). Another important numerical point is introducing "artificial viscosity" into SPH in order to stabilize the solution. Furthermore, "penetration" in Lagrangian particle based methods is inevitable even in low Mach numbers. In this section, the items which were mentioned here are discussed in more detail.

Artificial viscosity

in SPH an artificial viscosity term must be added to the momentum equation in order to suppress unphysical oscillations and stabilize the numerical scheme. In MONAGHAN & GINGOLD (1983) it was motivated in an effort to find a better alternative for the artificial bulk and Von Neumann Richtmyer viscosity in the shock tube problem, because they did not give satisfactory results in SPH. Although they were suitable for finite difference methods, they fail to capture the post shock front accurately in the SPH framework. The shock front was either excessively oscillatory or excessively smeared. The presented artificial viscosity in MONAGHAN & GINGOLD (1983), MONAGHAN & PONGRACIC (1985) is equivalent to bulk viscosity in 1D. However, it has been found that it is much more effective in suppressing

the unwanted oscillations in smaller length scales than the smoothing length, h , see BENZ (1990). Aside from the shock related phenomena, in the fluid phase the intrinsic real viscosity of the fluid is enough to stabilize the solution. In solid phase an artificial viscosity has to be introduced.

Artificial viscosity can be evaluated, see MONAGHAN (2005), by

$$\Pi_{ab} = \begin{cases} \frac{-\alpha c_{ab} \mu_{ab}}{\rho_{ab}} & \mathbf{v}_{ab} \cdot \mathbf{r}_{ab} \leq 0 \\ 0 & \mathbf{v}_{ab} \cdot \mathbf{r}_{ab} > 0 \end{cases}, \quad (3.48)$$

$$\mu_{ab} = \frac{h \mathbf{v}_{ab} \cdot \mathbf{r}_{ab}}{|\mathbf{r}_{ab}|^2 + 0.01 h^2},$$

where $\mathbf{r}_{ab} = \mathbf{r}_a - \mathbf{r}_b$, $\mathbf{v}_{ab} = \mathbf{v}_a - \mathbf{v}_b$, $c_{ab} = \frac{1}{2}(c_a + c_b)$, $\rho_{ab} = \frac{1}{2}(\rho_a + \rho_b)$ and α is a parameter in the order of unity. Having a closer look at the expression for the artificial viscosity, one can notice that it is symmetric with respect to a pair of particles "a" and "b". Hence the angular and linear momentum remain conserved. It should be noted that it is turned on for approaching particles while it is turned off for receding ones. This ensures that the modeled dissipation is positive and increase the entropy of the system, see BENZ (1990).

It is noteworthy to add two complementary points about the artificial viscosity. First, in case of high Mach number an extra quadratic term in the artificial viscosity is required to effectively control the penetration of the particles. This term is analogous to Von Neumann Richtmyer viscosity applied in finite difference scheme that produces a pressure force proportional to $|\nabla \cdot \mathbf{v}|^2$, see LATTANZIO ET AL. (1986). In this work, such a quadratic term in the artificial viscosity is not needed to be introduced due to the slow motion of the fluid. Second, although the artificial viscosity works well for capturing the discontinuity in a field variable, it may produce excessive dissipation in pure shear regimes. BALSARA (1995) proposed a factor f_{ab} that should be multiplied by the Π_{ab} to reduce the effect of artificial viscosity in the regions where the curl of velocity is considerable (shear flow). This factor can be calculated using

$$f_{ab} = \frac{f_a + f_b}{2} \quad f_{\zeta} = \frac{|\nabla \cdot \mathbf{v}|}{|\nabla \cdot \mathbf{v}| + |\nabla \times \mathbf{v}| + 0.0001 \frac{c}{h}} \Big|_{for \zeta} \quad \zeta := a \text{ or } b, \quad (3.49)$$

in which c is the sound velocity and $\nabla \cdot \mathbf{v}$ and $\nabla \times \mathbf{v}$ represent the divergence and curl of the velocity field, respectively. They are finally translated into the components of velocity gradient. Hence one can use equation (3.35) to compute the numerical value of them using SPH. This factor has been constructed in such a way that leads to correct limit value. It means that for purely compressional flows ($|\nabla \cdot \mathbf{v}| \gg |\nabla \times \mathbf{v}|$), it is identical to one and it goes to zero for purely shear flow ($|\nabla \cdot \mathbf{v}| \ll |\nabla \times \mathbf{v}|$), see BENZ (1990).

Tensile instability

One of the most cumbersome instabilities in SPH is called "tensile instability". It manifests itself in particle clumping and void generation in the domain, when a body is in tension state of stress. A Von Neumann stability analysis was firstly done by SWEGLE ET AL. (1995) to study tensile instability. Referring to figure (3.12), a rectangular configuration of stationary

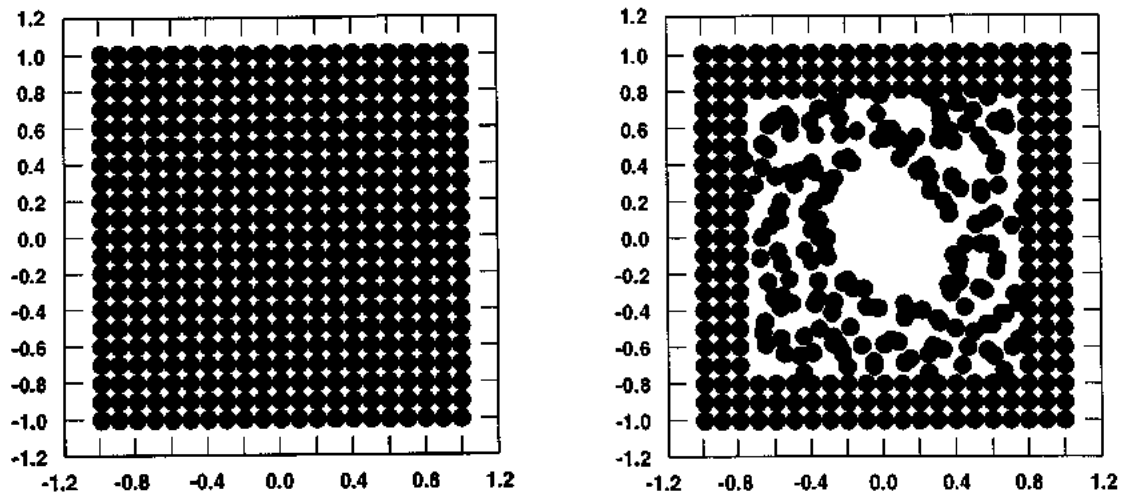


Figure 3.12. Tensile instability, from SWEGLE ET AL. (1995) (left) under compression right) under tension

particles were examined in two cases. In the first case, the whole domain was subjected to a hydrostatic positive pressure and in the second one the hydrostatic pressure was negative. In the first case if a very small perturbation is applied to the velocity of a single particle positioned at the center, the disturbance will travel in the whole domain for a long time as expected. In other words, all particles have small oscillatory movement around their equilibrium state. But in the second case, the instability starts to growing and finally leads to a catastrophic change in the particles configuration. Some particles fall onto each other and consequently several voids form. All these phenomena are not physical, but rather they are artifacts. A stability criterion was found assuming a 1D problem in terms of the stress and second derivative of the kernel. It was discovered that the solution is stable if $\sigma W'' > 0$, see SWEGLE ET AL. (1995). σ and W'' denote the stress and the second derivative of the kernel function, respectively. Figure (3.13) shows the stable region of a cubic spline kernel. Assuming h is approximately equal to the average particles distance, the method is unstable in tension. Because, the nearest neighbor of a particle locates in the region where the second derivative is positive.

Several techniques have been proposed to circumvent this instability. Due to the fact that this instability has a root in the kernel function, some researchers followed the idea of using special kernel functions. This remedy is not successful in all cases, see MORRIS (1996). In WEN ET AL. (1994) it was found that although the artificial viscosity is a dissipative term in SPH, it can not remove the tensile instability. Hence, another dissipative term in the context of conservative smoothing was introduced to suppress this instability for 1D. Later on, This idea was extended to higher order dimensions, see RANDES & LIBERSKY (1996). Another approach was to utilize the non-collocated spatial discretization of the stress and velocity, see DYKA & INGEL (1995). The main essence of the idea was to compute the constitutive laws at the points other than those in which the kinematic variables such as velocity and displacements are calculated. Such a points called "stress points" play the role of Gauss points in

FEM and the regular SPH points correspond to the nodes of an FE model. This idea proved to be promising and was developed further by other researchers, see RANGLES & LIBERSKY (2000) and VIGNJEVIC ET AL. (2000). Nevertheless, generating and dealing with a new set of points detracts from the attractiveness of this method. In CHEN ET AL. (1999) a new approach based on corrective formula for the kernel and kernel gradient has been presented and the results are encouraging for 1D and 2D cases. Belytschko BELYTSCHKO ET AL. (2000) was the first who diagnosed this problem in a general framework and found the root and cure of this disorder, although it had been already identified by the earlier researchers. It was discovered that the Eulerian nature of the SPH kernel (in current configuration) is the main cause of this instability. So, if one uses a Lagrangian kernel (in reference configuration), this instability is significantly cured. If the stress points are utilized in conjunction with Lagrangian kernel, the instability is completely eliminated.

In this work, the method of using "artificial stress" developed by Monaghan MONAGHAN (2000) has been employed to address the tensile instability. The main idea is to introduce a certain amount of artificial stress into the momentum equation in the direction of principal stress whose amount is positive. This kind of stress perturbation removes or at least alleviates this instability, while not changing the physical behavior too much. In this method, the mechanism by which the instability is treated is indeed a strong short range repulsive force that prevent the particles from clustering. Before we proceed with the description of this method, it should be notified that any method which is based on introducing new terms in the governing equations must be applied with cautious, because they affect the strength of material (material behavior). It means that one should be sure that their effect is negligible in reality. This is the case for the methods based on artificial repulsive force or dissipation.

Recalling equation (3.33) the artificial stress term can be calculated as follows

$$R_{ab}^{\alpha\beta} = R_a^{\alpha\beta} + R_b^{\alpha\beta},$$

$$R_{\xi}^{\alpha\beta} = \begin{cases} -e \frac{\sigma_{\xi}^{\alpha\beta}}{\rho_{\xi}^2} & \sigma_{\xi}^{\alpha\beta} > 0 \\ 0 & \sigma_{\xi}^{\alpha\beta} < 0 \end{cases}, \quad \xi := a \text{ or } b. \quad (3.50)$$

Unlike in equation (3.33), the superscripts i, j, α, β have been used in this equation for the components of the artificial stress tensor. The reason is that the artificial stress tensor is computed using the value of the principal stresses and the associated basis (α, β) . Afterwards, it is returned to the regular basis (i, j) by a transformation tensor \mathbf{Q} . It is obvious that the columns of tensor \mathbf{Q} are the eigen vectors of the stress tensor which corresponds to the principal directions.

$$R_{ab}^{ij} = (Q_{ab}^{i\alpha} R_{ab}^{\alpha\beta} Q_{ab}^{j\beta}) \left(\frac{W(|\mathbf{r}_b - \mathbf{r}_a|, h)}{W(\Delta)} \right)^n. \quad (3.51)$$

The parameter $e = 0.3$ and $n = 4$ were taken. Δ denotes the average particles spacing in the neighborhood of particle a . These parameters have been found in an optimized way. The repulsive force arising from the artificial stress term increases rapidly, by factor 23, when the distance between the two particles approaches zero. On the other hand if the particles distance is normal, the influence of this term is less than 0.5%. The reason is that the tensile instability is in fact a short wave length instability and the artificial stress term targets the

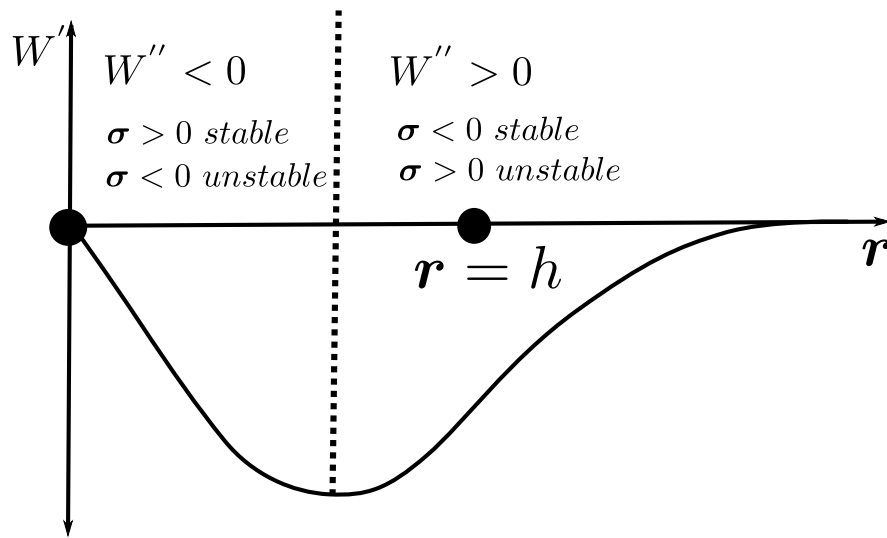


Figure 3.13. Stability regime for cubic spline

dispersion relation for short wave length perturbations while having a negligible effect on the long wavelength ones, see MONAGHAN (2000).

Zero energy mode

Zero energy modes are special modes of deformation which does not produce strain energy. It means that even though there are displacement (velocity) on the nodes, the evaluation of the gradient of displacement (velocity) gives zero and consequently no strain and stress is generated. one should distinguish between rigid body modes and zero energy modes. The former does not induce any stress (strain energy) in the body at continuum level, whereas the latter does. The fact is that the stress (strain energy) is not captured at discretization level for zero energy modes. From the mathematical point of view, zero energy modes appear due to the rank deficiency of the stiffness matrix. In FEM such spurious modes emerge as "hour-glassing" of elements in case of reduced integration, see WRIGGERS (2008). This also happens in Element Free Galerkin Method (EFGM) if the integration over an element is done using the nodal values, see BEISSEL & BELYTSCHKO (1996). The zero energy modes can freely grow due to numerical inevitable errors and finally dominate the solution and lead to the crash of the computational method. In SPH, the root of this rank deficiency lies in the colocal computation of kinematic variables and their gradient, see VIGNJEVIC & CAMPBELL (2009). It means that the idea of stress point, which was already explained as a treatment for tensile instability, can be utilized to eliminate such spurious modes, see VIGNJEVIC ET AL. (2000). Another idea is introducing a stabilizer term based on the penalization of the spurious modes, see GANZENMLLER (2015). This method has been inspired by the method of hour-glassing control in under integrated element in FEM.

In this work, it was tried to avoid abrupt loading which triggers the high frequency spurious modes. Furthermore, the boundary condition were well established. Hopefully, any symptom of zero energy modes was not observed.

Treating penetration using the XSPH variant

As discussed before, artificial viscosity mitigates the particles penetration to an acceptable degree, since it is activated for approaching particles and produces a repulsive force. However, penetration occurs even in low Mach numbers. The reason is that in SPH there is not a strong barrier preventing two particles from occupying the same position. The fact is that the kernel gradient is zero at the center of kernel support where the particle of interest lies (see figure (3.4)). So if another particle coincides with this one, it does not contribute to the gradient computation (see equation (3.10)). The idea to remedy this difficulty is to move the particles with a velocity other than that obtained from the momentum equation. This idea is the basis of so called XSPH variant developed by MONAGHAN (1989). In this modification, the position of a particle is updated using the modified velocity \bar{v} as follows

$$\frac{d\mathbf{r}_a}{dt} = \bar{\mathbf{v}}_a = \mathbf{v}_a + \epsilon \sum_b \frac{m_b}{\rho_{ab}} (\mathbf{v}_b - \mathbf{v}_a) W(|\mathbf{r}_a - \mathbf{r}_b|, h), \quad (3.52)$$

where $\rho_{ab} = (\rho_a + \rho_b)/2$ and ϵ is a parameter between zero and one. Using equation (3.52) for the movement of a particle ensures that the particle moves with the velocity which is close to the average velocity in its neighborhood. Surprisingly, it has been mathematically proved that this averaging procedure neither affects the momentum conservation, nor generates extra "dissipation". In dead, this procedure leads to extra "dispersion", see MONAGHAN (1989). In this work ϵ is taken to be 0.5. This technique is like a spatial filtering which prevents completely any type of penetration. Of course, this modification incurs computational overload because a smoothing procedure needs to be done once the velocities are computed from the momentum equation and prior to updating the positions.

3.3.3 Integration method

By applying the spatial discretization based on the SPH method to the continuum partial differential equation, one ends up with a set of ordinary differential equations in time. Any stable time integrator can be utilized to advance the particles in time. In SPH, explicit time-stepping methods are preferred over the implicit ones in terms of computational costs. It is well known that the explicit integrators are susceptible to the instabilities and consequently the maximum allowable time step is determined by the CFL condition. It is noticeable to stress that the symplecticness and reversibility of the integration method is as important as (or maybe more important than) its accuracy, see MONAGHAN (2005). In fact the long term behavior (after thousands of time steps) of a time integrator, depends on whether the important quantities such as energy and momentum are conserved or not. The SPH approach in simulating Lagrangian material points looks like molecular dynamics (MD) in which the trajectory of an ensemble of the molecules are modeled. The interested readers can see LEIMKUEHLER ET AL. (1996) for more discussion about the importance of symplectic time integrators. For SPH, several time integration methods have been proposed such as leap frog, velocity Verlet and predictor-corrector, see GESTEIRA ET AL. (2010). In this work, a velocity verlet proposed by ADAMI ET AL. (2012) was selected and implemented. This integrator is explicit, second order accurate (hence consistent with the SPH nature), symplectic and

efficient due to just one time force calculation per time step.

$$\mathbf{v}_a^{n+\frac{1}{2}} = \mathbf{v}_a^n + \frac{\Delta t}{2} \left(\frac{D\mathbf{v}_a}{Dt} \right)^n, \quad (3.53a)$$

$$\mathbf{r}_a^{n+\frac{1}{2}} = \mathbf{r}_a^n + \frac{\Delta t}{2} \mathbf{v}_a^{n+\frac{1}{2}}, \quad (3.53b)$$

$$\rho_a^{n+1} = \rho_a^n + \Delta t \left(\frac{D\rho_a}{Dt} \right)^{n+\frac{1}{2}}, \quad (3.53c)$$

$$\mathbf{r}_a^{n+1} = \mathbf{r}_a^{n+\frac{1}{2}} + \frac{\Delta t}{2} \mathbf{v}_a^{n+\frac{1}{2}}, \quad (3.53d)$$

$$\mathbf{v}_a^{n+1} = \mathbf{v}_a^{n+\frac{1}{2}} + \frac{\Delta t}{2} \left(\frac{D\mathbf{v}_a}{Dt} \right)^{n+1}. \quad (3.53e)$$

As mentioned earlier, to guarantee the stability of the computational method, the time step is governed by the CFL stability condition in conjunction with extra viscous and force conditions, see ADAMI ET AL. (2012).

$$\Delta t = \min \left\{ 0.25 \frac{h}{c_{max} + |\mathbf{v}|_{max}}, 0.125 \frac{h^2}{\nu}, 0.25 \left(\frac{h}{|\frac{D\mathbf{v}}{Dt}|_{max}} \right)^{\frac{1}{2}} \right\}. \quad (3.54)$$

Here, ν is the kinematic viscosity of the fluid. It should be noted that in case of the diffusion equation, the time step is similar to the viscous term above and is evaluated as follows

$$\Delta t = 0.125 \frac{h^2}{D}, \quad (3.55)$$

in which D is diffusivity coefficient.

3.4 Solution procedure (pseudo-code)

To provide the readers with a clear insight to the implemented numerical code, all of the algorithm steps have been described in two distinct pseudo-codes corresponding to the growth and biofilm-fluid interaction. In the growth process, the diffusion-reaction equation is solved along with advective movement of the biofilm due to the growth process. This process takes place in large time scales of the order hours. In fluid-solid interaction, two phenomena are modeled: the deformation of the biofilm in the presence of fluid flow and also the biofilm erosion. Such processes have relatively small time scales in the order of a fraction of seconds. Table (3.1) shows the implemented solution algorithm for the growth process and table (3.2) presents the steps employed in handling the biofilm-fluid interaction.

Remark: In all pseudo-codes, "TOL" is a user defined value (tolerance) for convergence.

Table 3.1. Pseudo-code for the growth process

```

DO for all time increments
  DO WHILE the diffusion-reaction equation reaches its steady state value ( $|\frac{dC}{dt}| < TOL$ )
    Solve the diffusion-reaction equation (equation (3.34))
  END DO
  DO WHILE the total biofilm relaxation condition is reached ( $|\frac{dv}{dt}| < TOL$ )
    Solve biofilm advection equations (equations (3.33), (3.32))
  END DO
END DO

```

Table 3.2. Pseudo-code of biofilm-fluid interaction (deformation and erosion)

```

DO for all time steps
  DO in predictor/corrector sub-steps
    Solve the fluid equations (equations (3.33), (3.31) for fluid)
    Compute the forces at the fluid-solid interface particles (equation (3.46))
    Solve the solid equations (equations (3.33), (3.31) for solid)
    Update the position of all particles simultaneously (equation (3.53))
  END DO
  DO WHILE no erosion occurs (equation (3.47))
    Apply erosion process if it occurs
    Update the list of eroded planktonic particles
    Update the interface geometry after the erosion process (refer to figure (3.10))
  END DO
END DO

```

Finally, the pseudo SPH based code for solving the governing equations (biofilm growth/deformation, fluid flow and diffusion-reaction) are provided. It should be noted that such pseudo-codes mimic the subroutines which are invoked within the main pseudo-code described in tables (3.1) and (3.2). To avoid redundancy, the pseudo code of the solid deformation is solely provided without a separate pseudo-code for the fluid flow. This is due to the fact that the rate-based hypo-elastic approach adopted for the solid deformation, is really similar to the common constitutive equations for the fluid flow. Tables (3.4) and (3.3) depict the implemented algorithms for the solid deformation and diffusion-reaction, respectively.

Table 3.3. Pseudo SPH code of diffusion-reaction

```

DO for all solid particles
  Apply the boundary condition on the interface particles
  Find neighbor particles using linked-list (refer to figure (3.14))
  Solve the diffusion equation (equation (3.34))
END DO

```

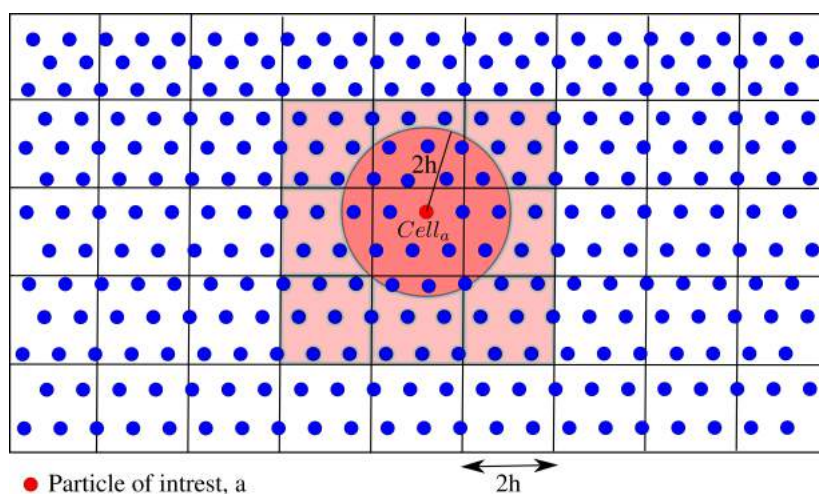
Table 3.4. Pseudo SPH code of solid deformation

DO for all solid particles
Update the pressure field using the equation of state (equation (3.36))
Compute the external forces on interface particles (equation (3.46))
(Remark: in case of fluid, apply the ghost value for the velocity and pressure of interface particle (equations (3.40), (3.42))
Find neighbor particles using linked-list (refer to figure (3.14))
Solve continuity and momentum equations (calculate the density change and acceleration using the neighbor particles (equations (3.31), (3.33))
END DO

3.5 Code optimization and parallelization

3.5.1 Neighbor search algorithm

In mesh-less methods, one needs to recognize the neighbors of a particle in order to be able to calculate the inter-particle interactions. Neighbors of a particle are defined as those lie in the compact support with radius $2h$. This information about a particle neighbors is more or less similar to the concept of "connectivity" in FEM. To find a particle neighbors, one need to use a search algorithm. In fluid simulation or solids undergoing large deformations, the neighbors of a particle may change in time and it means that the search algorithm must be efficient so that one can dynamically update the list of neighbors while solving the equations without too much computational costs. If a crude search algorithm is applied the number of operations for finding the neighbors of all particles is proportional to N^2 in which N is the total number of particles. In this work, a linked list based algorithm has been implemented which reduces the order of search operations to $N \log N$, see GESTEIRA ET AL. (2010). The difference is really considerable in terms of computational cost, when the number of particles is large.

**Figure 3.14.** Linked list for search algorithm

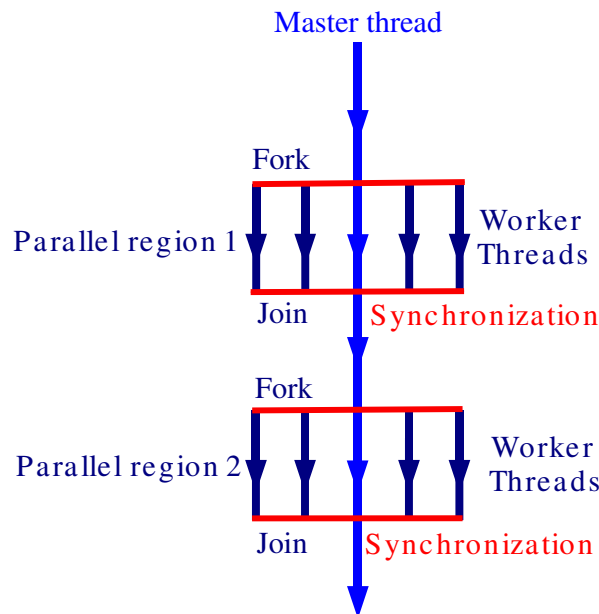


Figure 3.15. Illustration of a fork-join model for OpenMP

The main idea of the linked list is to map the particles on a grid. It means that there is a virtual grid in the background in which the particles are positioned. All particles have a unique tag and there is a data structure which stores the information of all grids. This information is nothing else than the tags of all particles which are within a certain grid. Now, one can take the advantage of this data structure. If the neighbors of a particle is needed, first one should know to which cell this particle belongs ($Cell_a$) and then one can search just the particles being in the cells attached to $Cell_a$. In other words, the search is confined to a small region of the domain instead of the entire domain. Figure (3.14) illustrates this algorithm. The size of the grid cell is equal to the radius of the kernel support which here is $2h$.

3.5.2 OpenMP implementation

In this work, the order of particles number in 2D is 10,000 and in 3D it reaches 500,000. Due to the explicit and co-local features of SPH, parallel implementation is motivated. It can accelerate the computation significantly. In this work, the parallelization has been performed using OpenMP "directives" within the code. The interested readers can find more information about the parallelization using OpenMP in HERMANN (2002). OpenMP is based on "shared memory architecture". It means that the parallel region of the code is distributed among several threads. The data communication between these threads is not explicitly controlled by the programmer, but rather it is accomplished implicitly by the compiler. That is the reason why OpenMP based programming is less complicated in comparison to the parallelization concepts that are based on "distributed-memory architecture" such as MPI. OpenMP uses a "fork-join" model of parallel execution, see figure (3.15). Initially, the application starts with a single thread (the "master thread" shown as a solid blue line). When the application hits a parallel region in the code, the master thread creates a team of parallel

threads. This is the "fork" phase. The portion of the code which lies in the parallel region, is then executed in parallel. In figure (3.15), the threads other than the master thread have been shown in dark blue. When the threads in the parallel region finish their task, they synchronize, terminate and go back to a single thread (the master thread). This is the "join" phase. Execution of the application then proceeds, possibly going through several parallelization stages.

There is a misconception about parallelization, especially by the ones who are not familiar with parallelization, that there might be a magic compiler option which automatically converts a serial code to a parallel one. The fact is that a code should be designed in a parallel style by the programmer. The compiler task is just to execute the designed program. It means that the logic behind the parallelization is created by the programmer. One should carefully think which parts of the code are so called "concurrent" or parallelizable. For example, some loops can be broken into several sub loops each of which is handled by a thread. In this work the main loop over particle is parallelized, see equations (3.31)-(3.34). For instance, if the number of particles is 10000 and the number of threads is 4, each thread computes the field variables for 2500 particles. In addition to "PARALLEL DO LOOP", some parts of the code have been parallelized using "WORK-SHARE" construct. For example, equations (3.53c) and (3.53.d) are independent. It means that two threads can work on them simultaneously. This is not the case for equations (3.53a) and (3.53b) because one can not start the computation on (3.53b) unless the (3.53a) is already solved. It means that if there is an inevitable hierarchy in the code, one should think about the "synchronization" as well. Furthermore, since the FSI modeling is fully explicit and monolithic, one can handle the fluid and solid phases at the same time using different threads. In this work the parallelized code was run on a node with 32 threads in HRZ cluster (Hybridrechenzentrum) at the Leibniz university of Hanover and the simulation was found to be almost 15 time faster than the serial version. It is obvious that all parts of the code is not parallelizable. Moreover, parallelization has some overhead due to synchronization and data communication. Hence exploiting 32 nodes does not necessarily mean a speed-up by factor 32.

Chapter 4

Numerical examples and results

In this chapter, some numerical examples are provided. In order to validate the developed code, first two available test cases in the literature are simulated to make sure about the correctness and accuracy of the developed numerical scheme. Then the numerical tool is applied to model the growth, deformation and erosion of biofilms. The computational results for the growth process are compared with those gathered in the experiments conducted by our colleagues in the medical school of Hannover.

4.1 Validation of the code

4.1.1 Test case 1: Elastic gate of a water tank

This example was firstly introduced in ANTOCI ET AL. (2007). In this work the interaction of an elastic gate with the fluid flow is simulated using a unified SPH-based numerical scheme in the context of a fluid-solid interaction (FSI) problem. Moreover, the results have been verified by the laboratory experiments. So, this is a pretty good and reliable example which one can consider as a benchmark. Figure (4.1) represents the initial configuration of the problem. The geometrical dimension of the system and also the material properties of the elastic gate is reported in Table (4.1).

Table 4.1. Geometrical dimensions and the material properties, see ANTOCI ET AL. (2007)

Parameter	Symbol	Value	unit
Dimensions			
Water level	H	140.0	<i>mm</i>
Tank width	W	100.0	<i>mm</i>
Elastic gate length	L	79	<i>mm</i>
Elastic gate thickness	S	5	<i>mm</i>
Elastic gate material properties			
Poisson ratio	ν	0.4	-
Young modulus	E	10	<i>MPa</i>

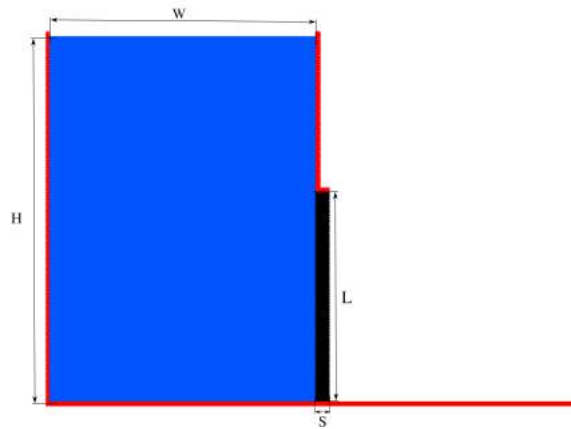


Figure 4.1. Initial configuration of the water tank and the elastic gate

The elastic gate is assumed to be clamped at one end and free at the other one. At the beginning, the free end is prevented from moving so that a hydrostatic equilibrium is reached. Then it is released and the water starts to flow under the gravity. The exerted force on the elastic gate from the fluid, make it to deform. Consequently, the gate opens and the water exit the tank bottom. The more the water accelerates, the more the gate deflects until a maximum deformation is reached. It is obvious that the decrease in the water level results in smaller interface forces which drives the gate. That is why the elastic gate returns back gradually. If The tank water were fed continuously with water in order to keep the water height constant, a steady state configuration for the elastic gate could be reached. In such a situation, the elastic gate would have a final deformation in which the elastic internal forces are in equilibrium with the external forces applied from the fluid side.

In figure (4.2) the deformed shape of the elastic gate has been plotted at $t = 0.20s$. The contours show the velocity field in the fluid and deformation of the elastic gate.

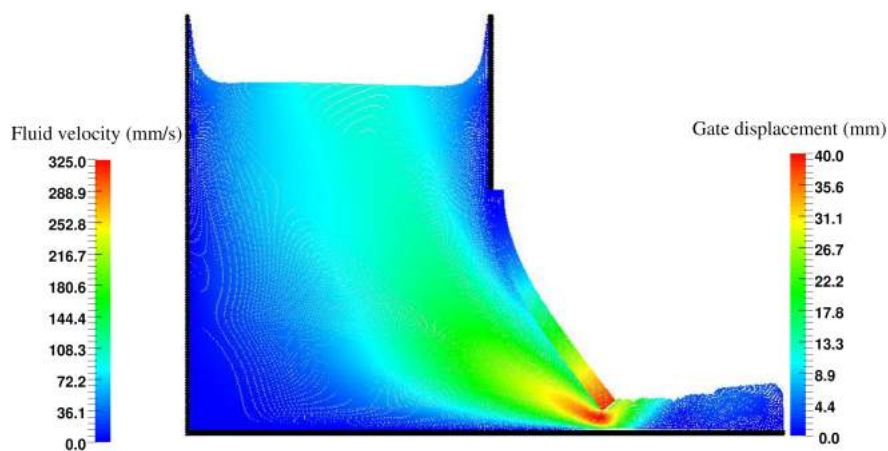


Figure 4.2. Fluid velocity and gate deformation

Figure (4.3) depicts the pressure in the fluid and the magnitude of the co-rotated Cauchy

stress in the elastic gate. The deformation with large displacement and large rotation in the elastic gate have been captured correctly. Furthermore, the vertical and horizontal displacement of a point at elastic gate tip has been plotted through time in figure (4.4). The results comply with the experimental and numerical data reported in ANTOCI ET AL. (2007).

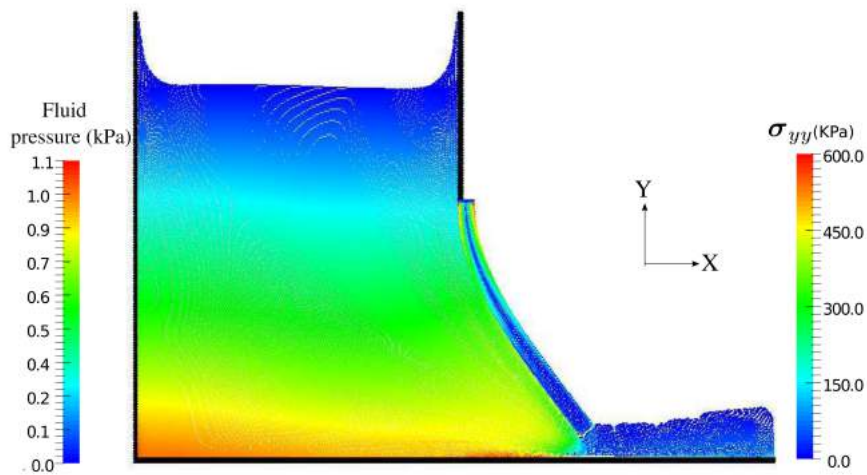


Figure 4.3. Fluid pressure and stress in elastic gate

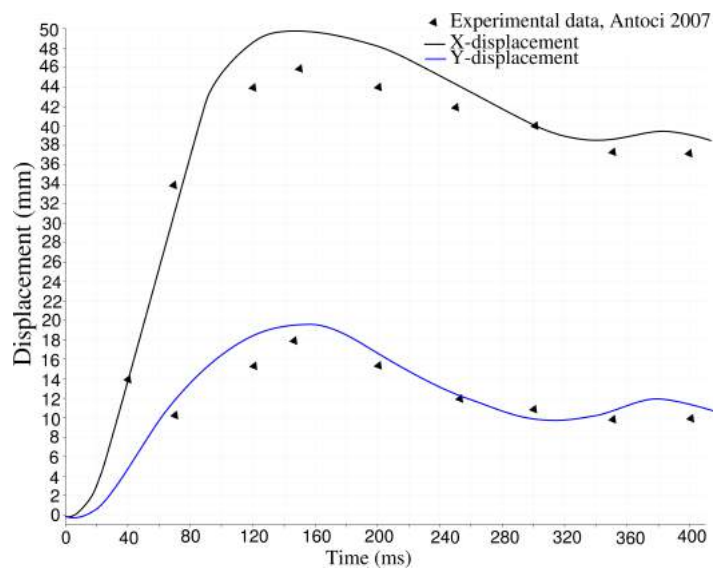


Figure 4.4. Horizontal and vertical displacement of the free end of elastic gate

Finally the time history of the water level in the tank has been plotted in figure (4.5). The results are in good agreement with the experimental data. As it is expected intuitively, the outlet flow rate is larger at the beginning because of the larger gate opening. The elastic gate returns back gradually once it reaches its maximum deformation. This is translated into a narrower slot at the tank bottom and lesser flow rate. Furthermore, the decrease in the water level results in a decrease in the pressure at the bottom of the tank. Consequently, the outlet velocity decreases. Theoretically, If the tank is drained completely the elastic gate should get back to its initial vertical position.

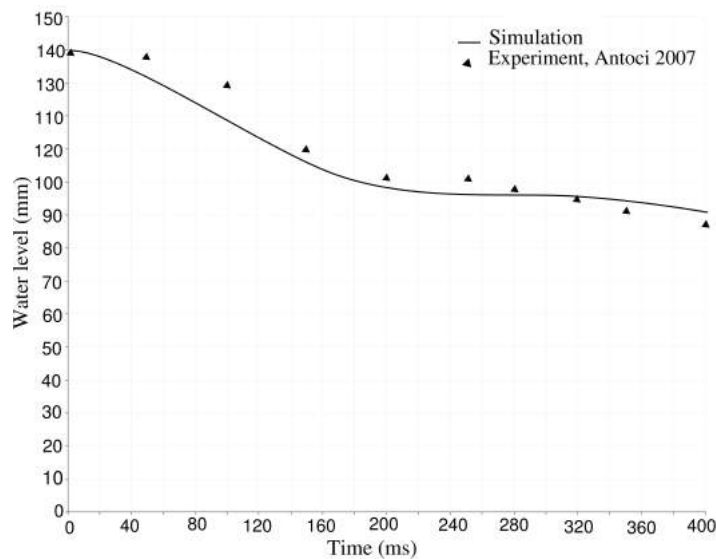


Figure 4.5. Water level in the tank at the center line

4.1.2 Test case 2: Rectangular biofilm deformation in fluid flow

This example has been taken from ALPKVIST & KLAPPER (2007) in which an artificially shaped 2D biofilm in the form of a rectangular block is deformed as a result of its interaction with the surrounding fluid. The fluid condition, material constants and geometric dimensions can be found in table (4.2). The upper plate velocity was set to V and its motion moves the bulk fluid around the biofilm. It exerts forces on the biofilm structure and finally causes it to deform until a final steady state is reached. Figure (4.6) depicts the normalized hydrostatic pressure profile prior to applying the horizontal velocity. The reference pressure for normalization is the one computed analytically at the bottom of the domain assuming a hydrostatic condition, namely $P_{ref} = \rho_f g H$.

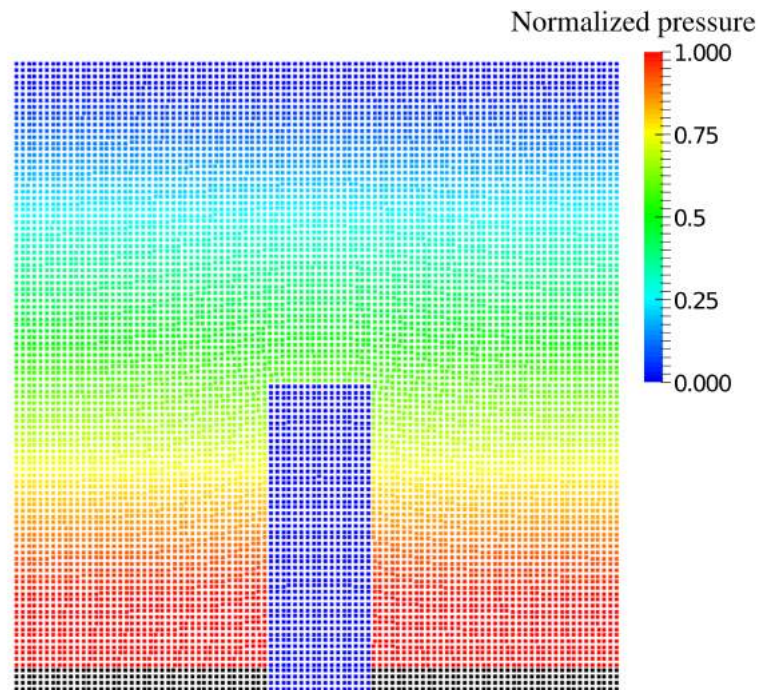


Figure 4.6. The initial configuration of a rectangular biofilm in fluid flow under the hydrostatic condition

Table 4.2. Model parameters and constants ALPKVIST & KLAPPER (2007)

Parameter	Symbol	Value	unit
Biofilm height	H	150	mm
Biofilm width	W	50	mm
Biofilm Poisson ratio	E	0.5	-
Biofilm shear modulus	μ	1	Pa
Fluid density	ρ	1000	kg/m ³
Fluid viscosity	μ	1.002E-3	Pa.s
Top plate velocity	V	1.00	mm/s
Particle size	Δ	3.0	mm

The results which are based on a fully continuum approach show good agreement with those achieved in ALPKVIST & KLAPPER (2007) in which discrete mass-spring elements have been used to model the biofilm deformation. Figure (4.7) illustrates the final (steady state) configuration of the deformable biofilm in the fluid flow as well as the flow streamlines. It should be noted that the real time having been simulated is much less than the characteristic growth time of the biofilm and that is why no growth occurs in this test case.

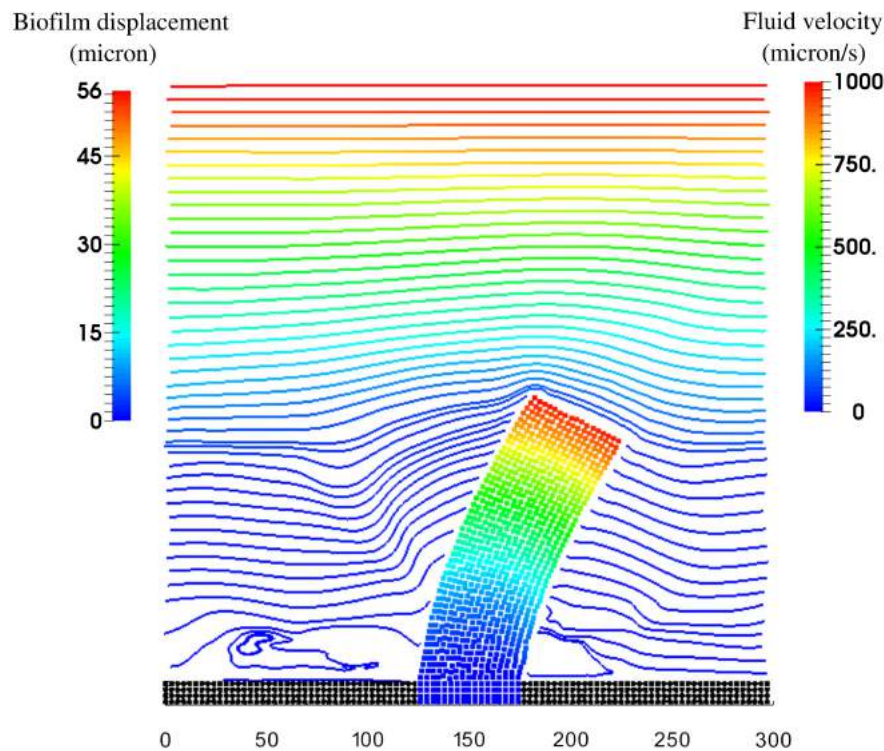


Figure 4.7. The steady state configuration of a rectangular biofilm in fluid flow

4.2 Biofilm deformation and erosion

Two and three dimensional simulations have been performed in this section to model the biofilm erosion due to the induced shear forces at the biofilm surface. Table (4.3) contains material properties, constants and parameters required for this case. For the sake of simplicity in visualization, the 2D results (plane stress assumption) are first presented and 3D results are provided afterwards.

4.2.1 Deformation and erosion 2D

In this exemplary case, an initial single biofilm hump is considered. It is located at the center of the flow chamber. It is exposed to the fluid flow which is driven by a top plate having the velocity V . The value to which the velocity of the top plate is prescribed, can be estimated using the flow rate in the experiments. This point needs to be explained further. In our experiment, the flow rate is controlled by a peristaltic pump. Knowing the flow rate (Q) and the cross-section of the flow chamber A , one can find an average velocity in the flow chamber ($Q = \rho AV$). This bulk velocity V is assumed to be equal to the stream velocity far from the boundary layer within the RVE. It means that the effect of the fluid velocity is transferred to the RVE by prescribing the velocity of the top plate to V . The reason behind such a boundary condition is that the size of the RVE is limited to several tens of microns due to the computational cost, while the real height of the fluid in the flow chamber is about

500 microns. The RVE has a periodic boundary condition at the lateral sides. The bottom side is attached to a fixed substratum over which the biofilm forms. The boundary condition at the top side of the RVE needs to be defined properly. Undoubtedly it can not be regarded as a periodic one. Free boundary (Neumann boundary condition) is not correct, since in reality there is a column of water over that. If it is considered to be fixed (zero Dirichlet boundary condition), it results in non-physical excessive dissipation due to the formation of a boundary layer near the top fixed boundary. So the best boundary condition for the top side of the RVE which ensures the most physically correct velocity profile within the RVE, is prescribing it using the macro scale averaging. Figure (4.8) clarifies this argumentation. It should be admitted that this idea was taken from the homogenization theory which makes a bridge between the kinematic quantities at the micro and macro scales. In fact the velocity applied on the top side of the RVE is similar to prescribing linear displacement to an RVE in homogenization theory. The prescribed value comes from the upper scale and here it is equal to the average velocity in the flow chamber. The readers seeking more details on homogenization theory may refer to ZOHDI & WRIGGERS (2005).

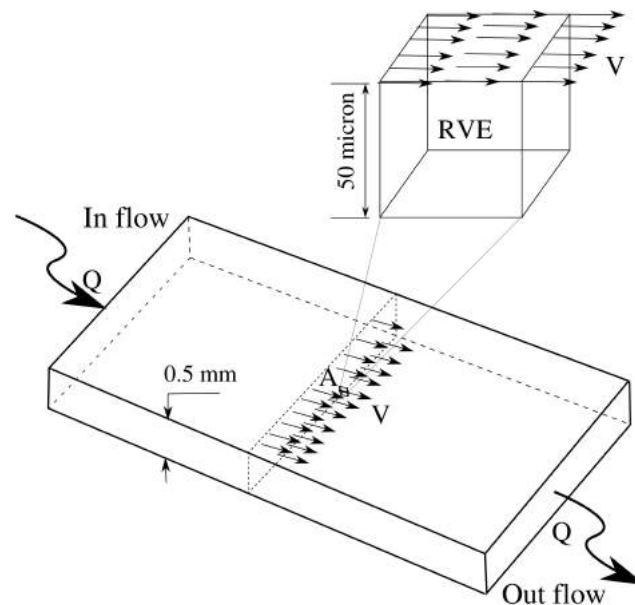


Figure 4.8. Prescribing the velocity of the RVE top side using average bulk velocity in the flow chamber

In figure (4.9), the biofilm structure has been depicted in two different time steps. It should be noted that the time has been non-dimensionalized using $t_{ref} = \frac{100h}{C_0}$. It is observed that the biofilm colony loses gradually some bacteria at the interface. Actually, the inter-facial shear stress therein exceeds the biofilm cohesion strength. The detached bacteria are washed away by the fluid forces and form a filamentous tale-like streamer floating in the fluid flow downstream. In some cases, especially when the biofilm is too soft, streamers formation may happen even prior to detachment and in fact the biofilm is highly deformed and elongated. Such phenomena have been repeatedly reported in the literature, see ALPKVISTA & KLAPPER (2007), XAVIER ET AL. (2005), STOODLEY ET AL. (1998) and STEWART (2012). An animation of this process can be viewed in the supplementary materials of this work.

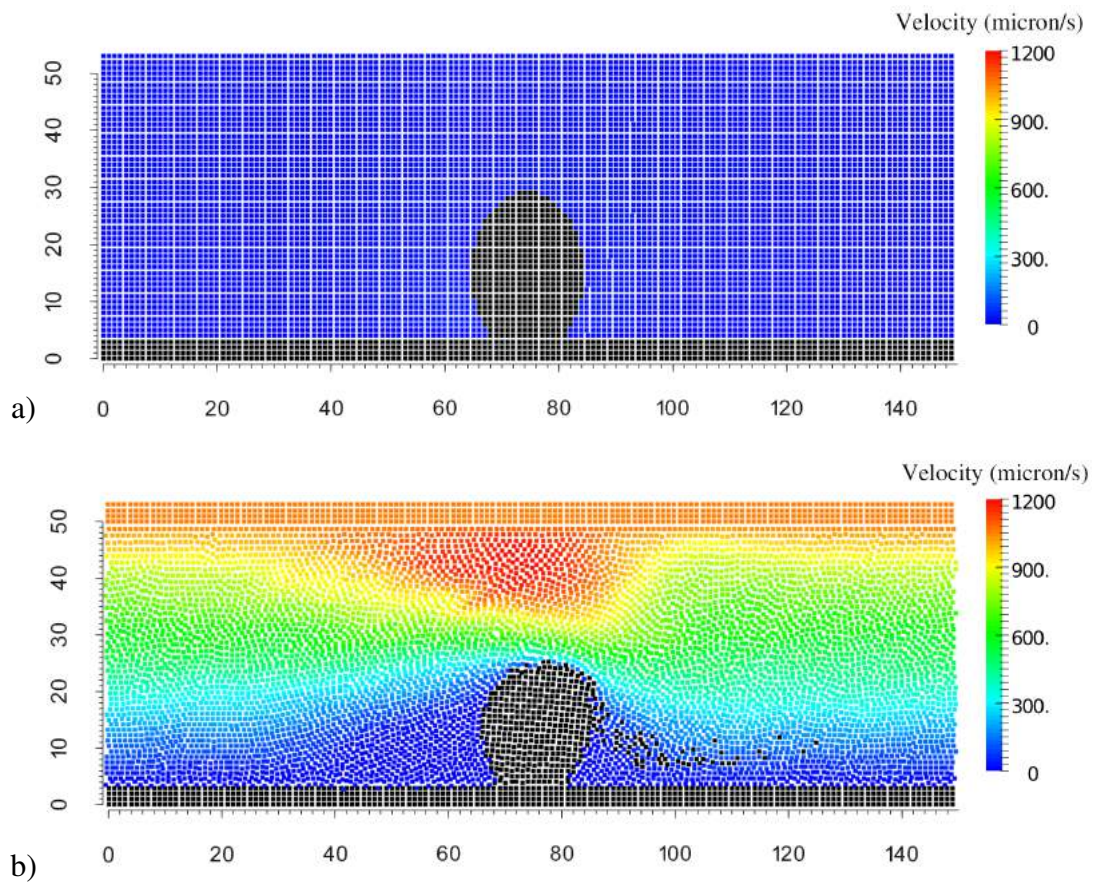


Figure 4.9. Biofilm erosion a) initial velocity profile b) velocity profile and eroded bacteria after $\tau = 1500$

Table 4.3. Model parameters and constants (material property from BÖL ET AL. (2009))

Parameter	Symbol	Value	unit
Biofilm initial height	H	30.0	μm
Biofilm initial maximum width	W	20.0	μm
Biofilm Young modulus	E	10	Pa
Biofilm Poisson ratio	ν	0.3	-
Biofilm interface strength	τ_y	0.1	Pa
Biofilm density	ρ_b	30.0	kg/m^3
Fluid density	ρ_f	1000	kg/m^3
Fluid viscosity	μ	1.002E-3	Pa.s
Top plate velocity	V	1.00	mm/s
Particle (bacteria) size	Δ	1.0	μm

Figure (4.10) shows the stress in the biofilm compartment which has not been eroded, yet. Two important points can be extracted from this figure. First, before the horizontal fluid

velocity is applied and consequently the erosion starts (at time $\tau = \frac{t}{t_{ref}} = 10$), the biofilm is in a tension state of stress. The reason is that in a hydrostatic equilibrium an effective upward buoyancy force, originating from the density difference between the fluid and biofilm, tends to lift up the biofilm. Second, once the fluid moves, the effective drag force on the biofilm bends it and changes the stress state. As expected, the mechanical stress has the maximum value at the lower part of the biofilm where it is anchored to the substratum. However the value of the stress is less than the biofilm strength in this region and hence no sloughing happens.

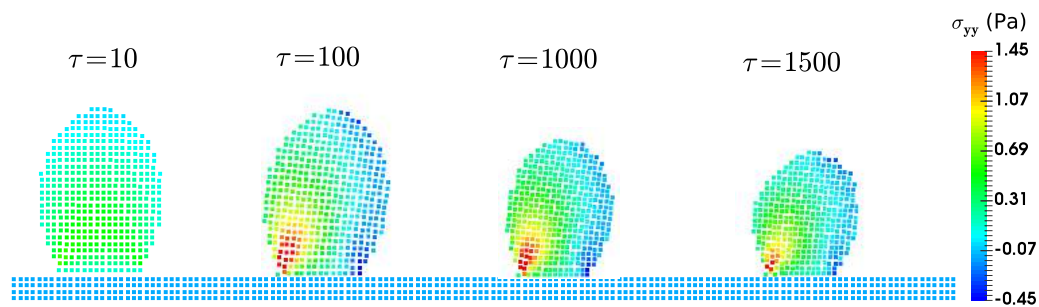


Figure 4.10. Mechanical stress development in not eroded biofilm during time

In figure (4.11) it can be seen that the biofilm experiences a vibrational micro-motion in the fluid flow direction. This is due to the continuous erosion which produces sequential impulses on the biofilm structure and triggers the first vibration mode of that. It means that the biofilm response to the fluid flow is dynamic during the erosion process. It is expected that such a movement is gradually suppressed when the erosion process stops due to the reduction of shear forces once enough material is washed out and the fluid velocity decreases in the vicinity of the biofilm.

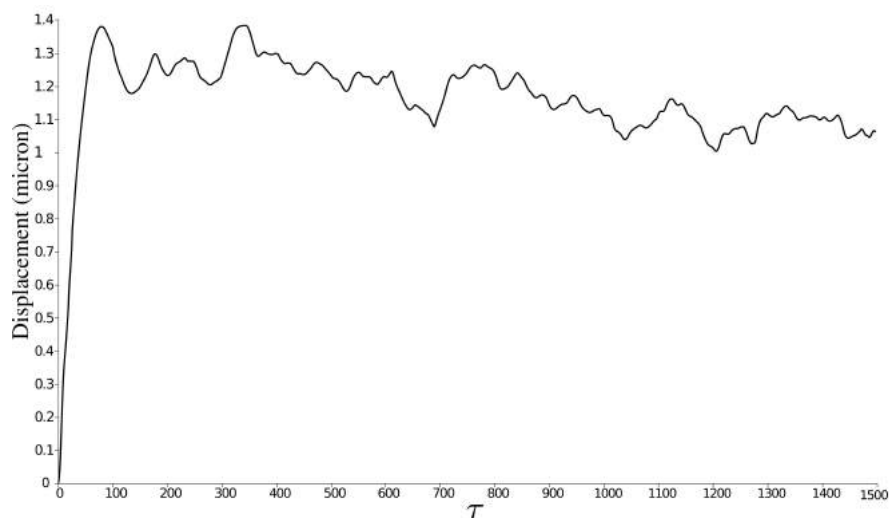


Figure 4.11. Displacement of the biofilm center in time during the erosion process

4.2.2 Deformation and erosion 3D

In the 3D case, a cubic region with an elliptically shaped biofilm attached to the center of the substratum is considered. This is in fact a generalization of the 2D case discussed in the previous subsection. The initial configuration of the particles is generated based on the Cubic Close Packing (CCP) lattice structure using the algorithm introduced in the section (3.2.1). Such a lattice structure is the mostly dense arrangement of particles which is possible in 3D. This gives the chance to reduce the smoothing length h in order to incur lesser computational cost. The smoothing length is taken to be $h = 1.3\Delta$ instead of $h = 1.5\Delta$ which was chosen for 2D cases. Nevertheless, the number of neighbors are still considerable (about 105 for a fully contained kernel). Comparing the number of neighbor particles in 3D, even using a reduced smoothing length, with that in 2D cases (about 37 for a fully contained kernel), one can easily realize that how enormously the computational cost grows. Furthermore, the presence of the third dimension increases the number of total particles drastically. That is why a serious jump in the computational cost is experienced when one goes from a 2D case to the corresponding 3D one. However, simulating a problem in 3D is inevitable, because some phenomena are degenerated or at least significantly influenced when one switches from 3D to 2D assumption.

In this section the flow condition is the same as the 2D case. It means that the flow is in the Y direction and the boundary condition is assumed to be periodic in both X and Y lateral sides, see figure (4.12).

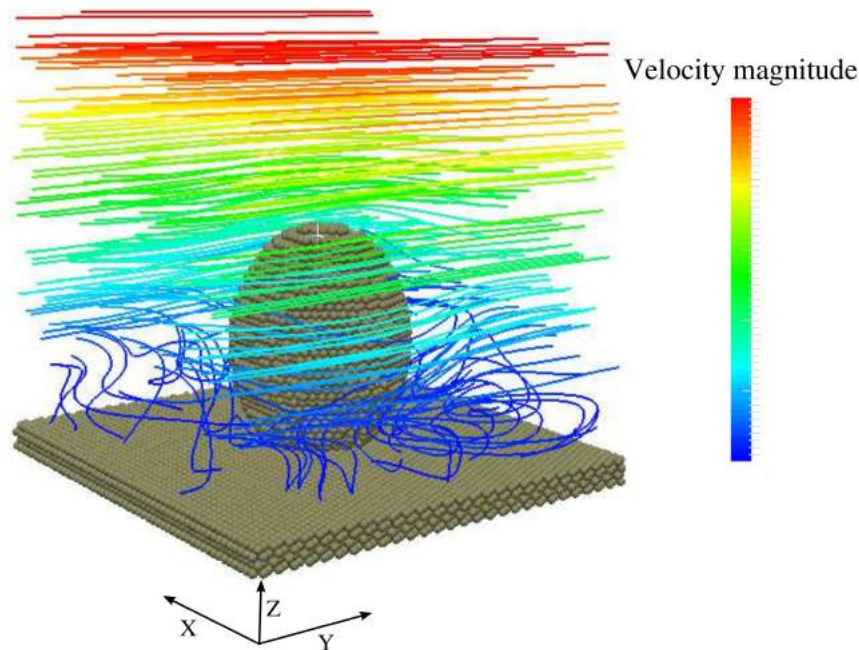


Figure 4.12. 3D biofilm in fluid flow

Figure (4.13) illustrates the stress analysis in the biofilm through time. The results are qualitatively similar to those obtained with 2D assumptions. However, the stress values are different. The reason is that in the 2D case, the assumption of plane stress implies that the geometry of the biofilm is a thin plate which can be generated by extruding the 2D geometry in the third dimension. This is totally different from the real 3D geometry in which the biofilm has an elliptical shape. For visualization purpose, a quarter of the biofilm is cut and removed, so that one can see the stress state in the bulk of the material.

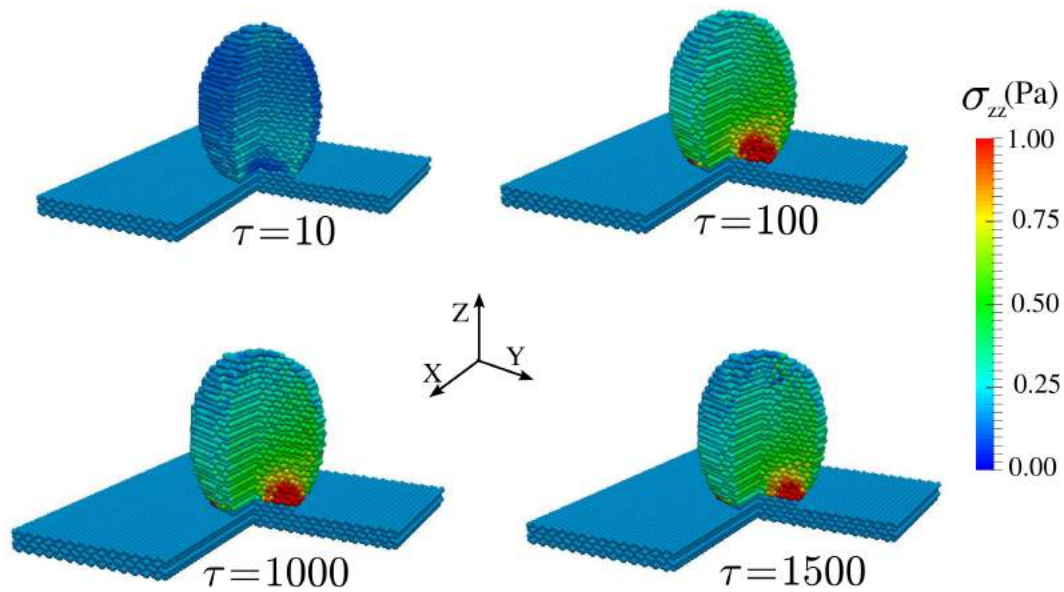


Figure 4.13. Mechanical stress in not eroded 3D biofilm during time

Figure (4.14) shows the tail formation for the eroded particle behind the biofilm. Similar to the 2D case, the eroded bacteria (particles) form a streamer in such a way that it conforms to the streamlines of the fluid flow. Furthermore, due to a very low Reynolds number (around 0.04) the pressure profile in the fluid is close to the hydrostatic pressure distribution and the flow regime is laminar in principal. Another important point can be realized about the erosion pattern from this figure. The biofilm is eroded dominantly from the biofilm front side which the fluid flow hits. The eroded particles are moved by the flow to the back of the biofilm and accumulate there. This accumulation of eroded particles shields the back side of the biofilm from being eroded. This leads to a non-symmetric pattern for the erosion. The last frame ($\tau = 1500$) in figure (4.13) illustrate this fact, clearly.

The movement of the eroded particles which have formed a streamer behind the biofilm can contribute to more mixing in the boundary layer and enhancing the nutrient up-take rate. This phenomenon has been studied comprehensively in TAHERZADEH ET AL. (2010). But in this work the effect of the streamers movement on the nutrient transport mechanisms has not been taken into account.

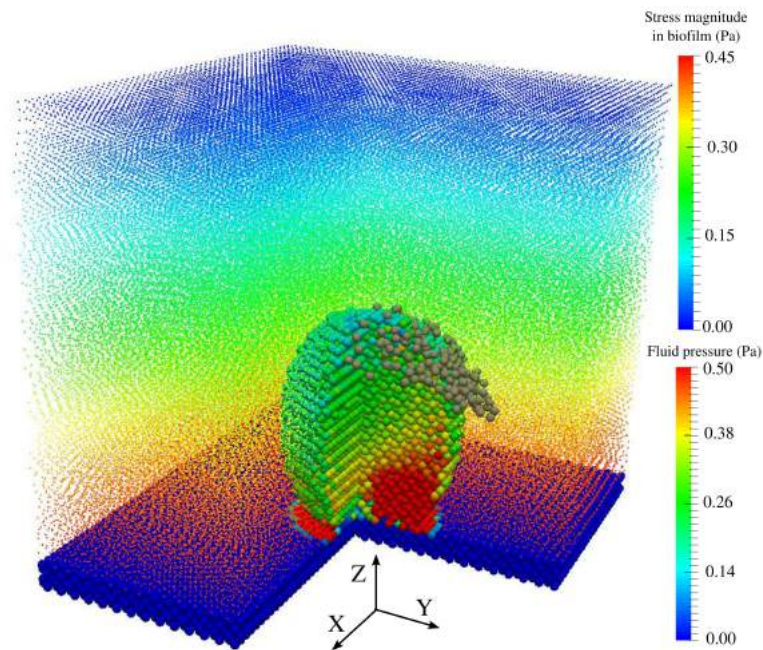


Figure 4.14. Streamer formation behind the 3D biofilm

Similar to the 2D case, the successive removal of particles results in an oscillatory response of the biofilm which seems to last as long as the erosion takes place. The movement of a point at the centroid of the biofilm has been plotted versus time in figure (4.15). It seems that such a micro motion facilitates the detachment process. An intuitive explanation along with an example can be presented about this effect. Such an effect is instinctively used even by animals when they want to get rid of the dust or debris which is in their furs. By shaking their skins or bodies, the dusts are thrown away.

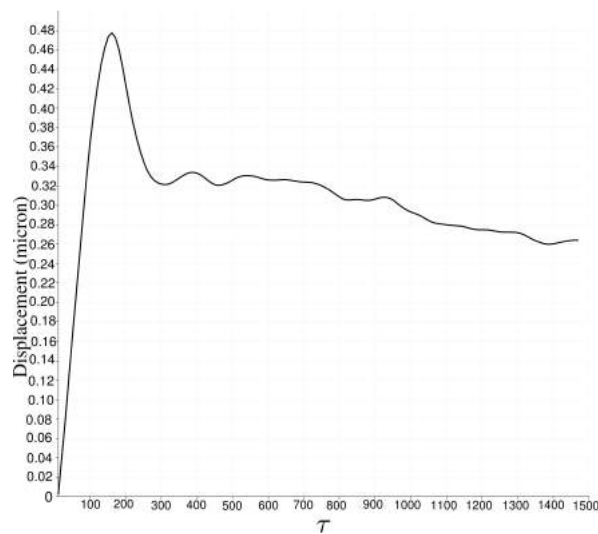


Figure 4.15. Displacement of the 3D biofilm center in time during erosion process

4.2.3 The impact of the fluid velocity on the erosion rate

It seems to be undeniable that the more the fluid velocity is, the faster the detachment process occurs. The reason is that the larger velocity means more induced shear on the biofilm and consequently a faster rate of material erosion. To investigate the effect of the velocity on the erosion rate, the erosion process was simulated using two different flow velocities. Looking at figure (4.16), it can be found that there is a logical relation between the flow velocity and the erosion rate. It should be stressed that the vertical axis corresponds to the mean value of the biofilm height \bar{h} being under erosion. It can be seen that \bar{h} decreases through time due to the erosion process. τ in the horizontal axis denotes the dimensionless time as in figure (4.11).

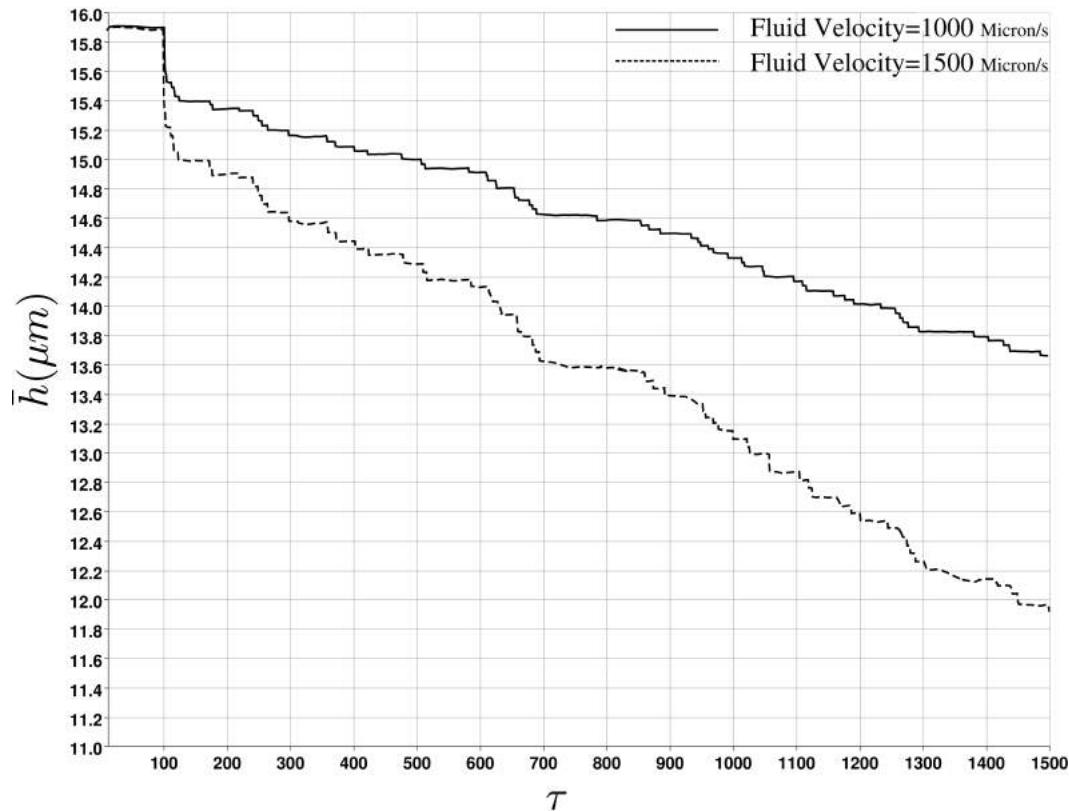


Figure 4.16. The effect of different fluid velocity on the erosion rate

Even though the argument made for figure (4.16) may be true, the story of erosion is not that simple. Comprehensive experiments conducted in HORN ET AL. (2003) revealed that surprisingly neither the flow velocity nor the shear stress does not correlate well with the detached biomass in long term, see figure (4.17). In this work an almost linear correlation was found between the mean value of the biofilm height before detachment and afterwards, see figure (4.16). This discrepancy can be explained as follows.

In the HORN ET AL. (2003), the experiments are conducted in time scales of order several days. It means that the growth process plays an important role, in fact an opposite role, besides the detachment process. Moreover, In the experiments the detachment process is

not limited to solely surface erosion. It means that other detachment mechanisms such as sloughing can happen, in reality. Our simulation is in a very short time scale (a fraction of a second) and hence almost no growth occurs during erosion process. On the other hand, our detachment mechanism is limited to erosion process which takes place at the interface.

Here, a question may arise. Considering that both erosion and growth have been modeled in this thesis, why not a combined growth-erosion simulation in long term is performed? The answer is that theoretically it is possible, because the developed tool in this work is capable of modeling both of these processes. However, in practice it is impossible. The reason is that the deformation and erosion process in the context of an FSI (Fluid-Solid Interaction) problem are computationally very costly, even if one wishes to simulate a couple of seconds of the physical process. For example it might take several days to simulate a few minutes of a dynamic FSI problem. One can not even imagine the required run time for simulating a long FSI problem (for example 1 day) coupled with growth. To circumvent such an issue, one can make suitable bridge between these two processes taking place in different time scales. In other words, in stead of solving these two process concurrently, they can be tackled in a hierarchical manner. Clearly speaking, one can find an effective rate of detachment from small time scale analysis and pass it to the analysis in the larger time scale. Developing such a multi-scale analysis remains as a further future task and here we just wanted to motivate the readers and ignite the basic idea behind that. The fact is that the results based on a short time simulation of erosion are practically useless, because there is no experiment having been conducted in such a short time scale.

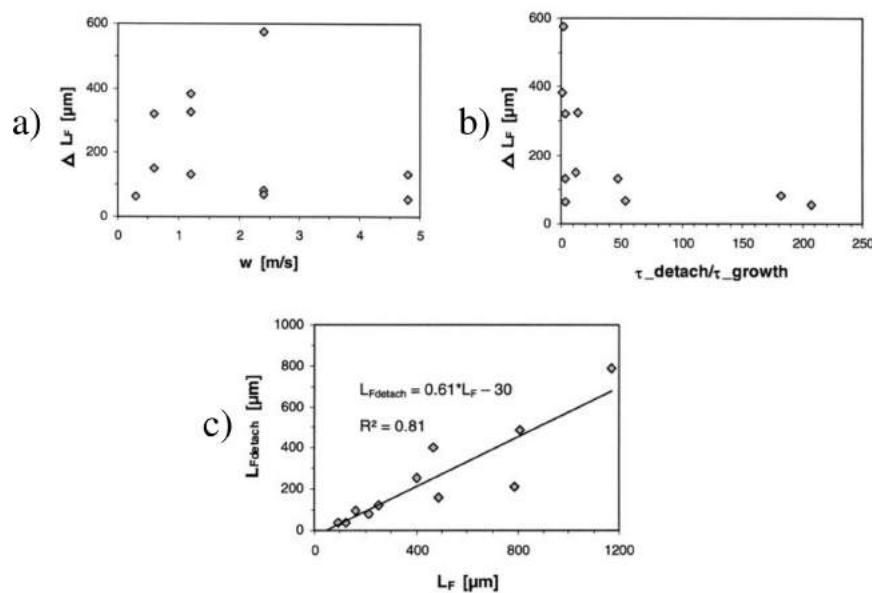


Figure 4.17. Dependency of detached biomass ΔL_F a) on the flow velocity w b) on shear stress ratio $\tau_{detach}/\tau_{growth}$ c) dependence of the mean biofilm thickness after detachment $L_{F,detach}$ on the biofilm thickness L_F before detachment. From HORN ET AL. (2003)

4.3 Biofilm growth

The biological growth process of a 2D and 3D biofilm is simulated in this subsection. It is assumed that an initial semi elliptical colony of bacteria exists on the surface and it starts to grow. In other words, the initial condition is assumed to be pre-known. As it was explained in the first chapter, the initial colonization of a surface is a complex process governed by electro-chemical phenomena in the molecular length scale. In practice, the initial condition of the biofilm in a computational model is taken in such a way that conforms to the experimental observation after a short exposure time such as a few hours. The material properties and parameters are listed in table (4.4) for this example.

Table 4.4. Model parameters and constants (material property from BÖL ET AL. (2009))

Parameter	Symbol	Value	unit
Biofilm initial height	H	30.0	μm
Biofilm initial maximum width	W	20.0	μm
Biofilm density	ρ_b	30.0	kg/m^3
Reaction Constant in Monod law	K_1	0.12	1/hour
Reaction Constant in Monod law	K_2	4.0E-18	$gr/\mu m^3$
Nutrient Concentration in Bulk fluid	C_f	3.0E-18	$gr/\mu m^3$
Yield Constant in Monod law	Y	1.0	gr/gr
Particle (bacteria) size	Δ	1.0	μm

4.3.1 Biofilm growth 2D

Figure (4.18) depicts the spatial evolution of a 2D biofilm as a result of the biological growth and nutrient consumption in a 24 hours period. It can be seen that how the nutrient distribution changes with the evolution of the biofilm. It should be notified that the concentration field has been non-dimesionalized using a reference value. The reference value is equal to that of the nutrient concentration in the bulk fluid (C_f). It is in fact the maximum available nutrient concentration in the whole system. It is a common assumption that the fluid is well mixed due to the dominancy of the convection transport mechanism and the nutrient concentration is a prescribed variable in the bulk fluid. However, it is computed in the biofilm using the diffusion-consumption equation.

Figure (4.18) reveals that the more the biofilm grows, the less nutrient is available inside. Of course, there is always a nutrient flux from fluid to the biofilm through the interface via the diffusion mechanism. Although this makes up for the consumed nutrient by the bacteria, as the biofilm expands spatially, the overall nutrient amount in the lower region

of the biofilm decreases. It means that the biofilm has a larger growth rate in the regions near the interface and a slower rate in the interior regions. In some cases the shortage of the nutrient in the interior regions may result in death of the bacteria. They form an inactive region in the biofilm which even shrinks because of the chemical decay (instead of growth). The presence of the inactive biomass has been reported in the biological observations and was detected by our experimental colleagues as well. In this research the effect of the inert biomass shrinkage was neglected, because it was experimentally found that the portion of the inactive biomass is much less than the total active biomass, especially in small time periods (for example 1 day). Some researchers who use individual based methods, have introduced this consolidation effect in their biomass modeling, see LARDON ET AL. (2011). But it is much more challenging to incorporate this phenomenon in a continuum based framework.

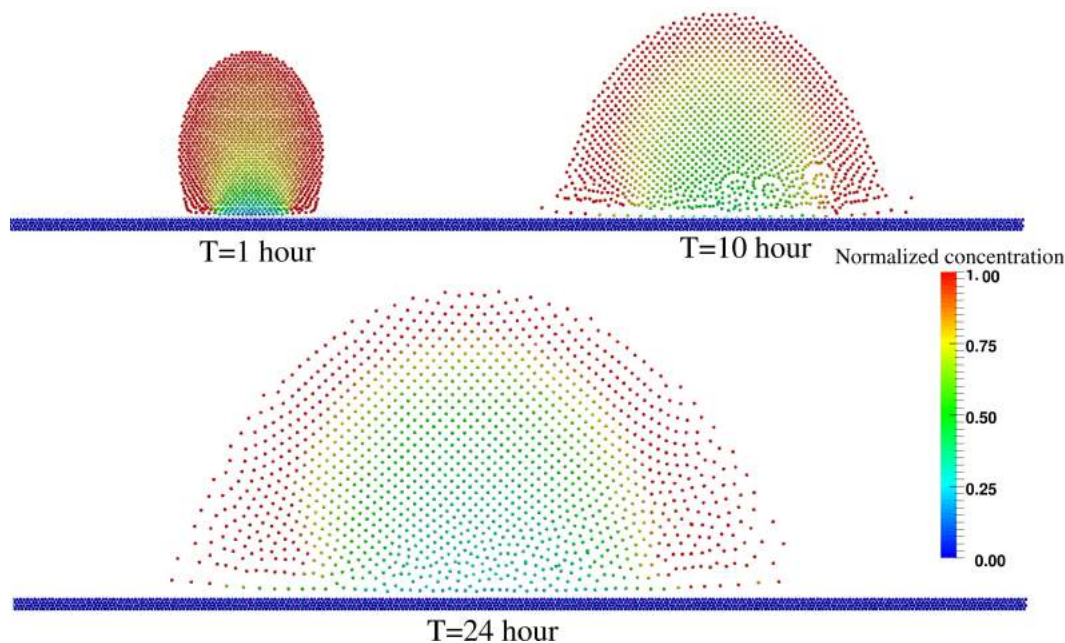


Figure 4.18. 2D Biofilm growth and nutrient concentration

Figure (4.19), is exactly similar to figure (4.18) at the time $T = 24$ hours with the difference that the refinement technique introduced in section (3.5) has been activated, when the average particles distance is doubled as the result of the biofilm expansion (growth). This simulation has been done to understand how the refinement procedure affects the overall growth phenomenon. As discussed in section (3.5), this re-meshing procedure introduces some perturbation into the model due to the inevitable error in density estimation. However, it recovers the accuracy of the interpolation. It means that one should use it, in the cases that the particles distance increases too much as a result of the growth process.

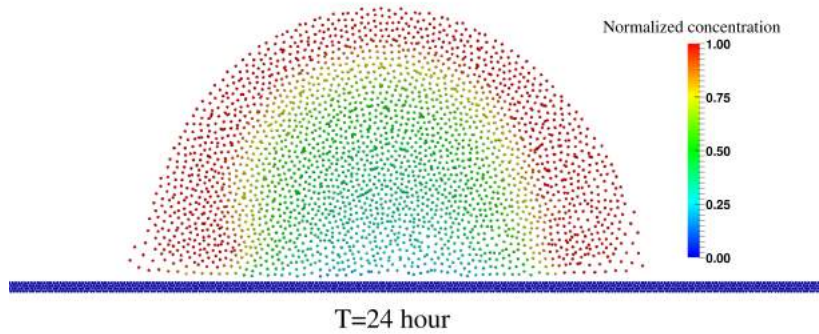


Figure 4.19. Particle splitting (mesh refinement)

The average height of the biofilm has been plotted versus time in figure (4.20). The volume of the generated biomass is a measurable quantity indicating the growth rate. In practice, the total volume of the biofilm is calculated using laser scanning microscopy. If this value is divided to the area of interest, it gives the average height of the biofilm. In our experiments, this value is carefully measured regularly during a period of 1 day. The experimental results are compared with those obtained from a 3D simulation.

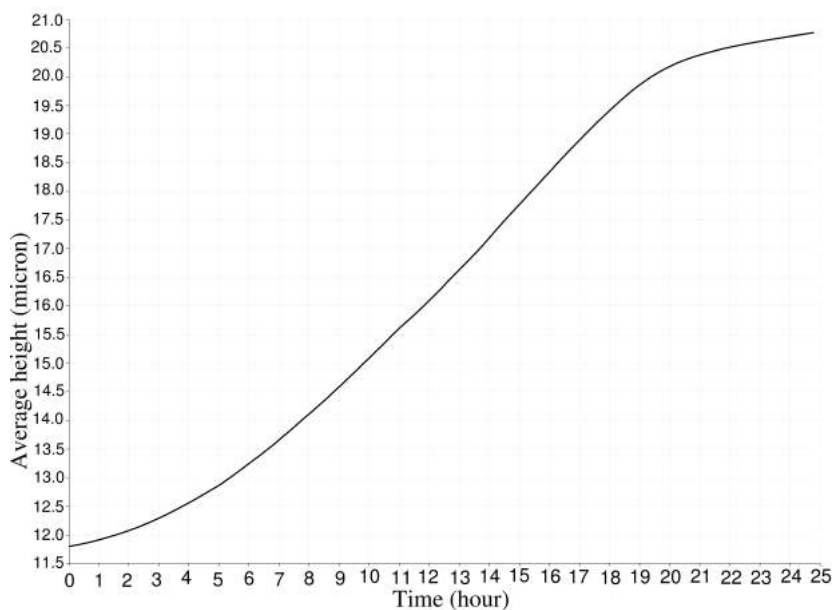


Figure 4.20. Average height of the 2D biofilm in time

4.3.2 Biofilm growth 3D

Figure (4.21) illustrates the growth of a 3D biofilm and the normalized (non-dimensionalized) nutrient concentration during 24 hours. It can be seen that the results are qualitatively similar to those obtained using 2D assumptions. It should be noted that the 3D RVE has periodic boundary conditions at all lateral sides and that is why the biofilm can take the whole space around itself as it grows up.

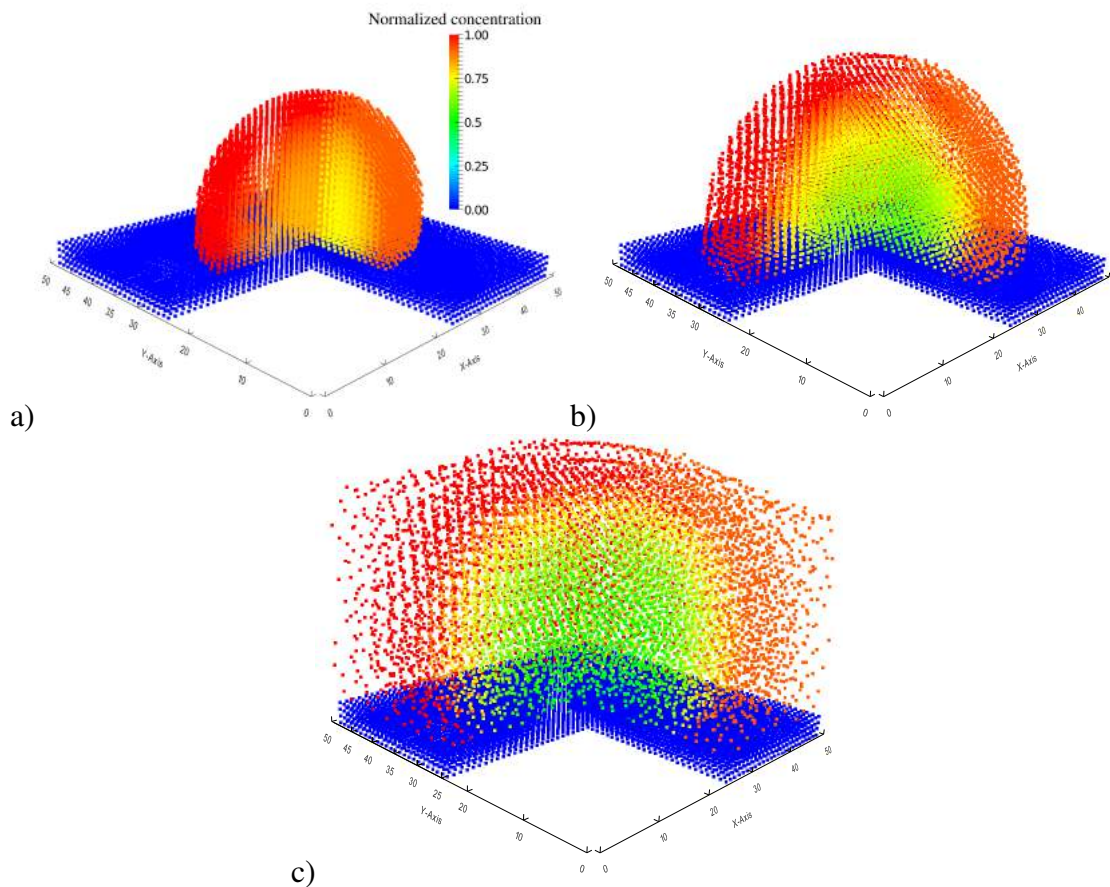


Figure 4.21. Biofilm growth and nutrient concentration a) after $T=6$ hours b) after $T=12$ hours c) after $T=24$ hours

It should be stressed out that the induced fluid velocity from the biofilm growth is so small (of order one micron per hour, see figure (4.22)) that the fluid flow is not disturbed in practice. From the computational point of view, it means that it is not required to explicitly resolve the fluid flow governing equation as a function of the growth. In other words, capturing the interface is sufficient to update the geometrical domain of the fluid flow. That is why some researchers who focus just on the biofilm growth, never deal with the Navier-Stokes equations at all, see LARDON ET AL. (2011), and they assume to have a pre-known boundary layer as the fluid-biofilm interface whose thickness is constant.

In figure (4.23) the average height of the biofilm has been plotted after 24 hours which reflects the biofilm growth. The experiments were repeated 3 times and the data were collected

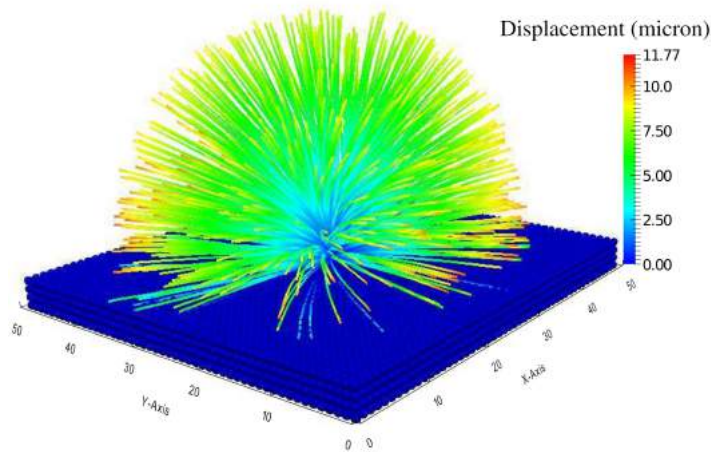


Figure 4.22. Streamline of biofilm growth after $T=12$ hour

from several points of interest. The relatively large standard deviation in the experimental data implies how non-deterministic the process is. The computational results are satisfactory in comparison with those measured in experiments. It is obvious that the parameters of the problem could be calibrated using the experimental results in such a way that the experimental and numerical results fit better. However it does not necessarily mean that such calibrated parameters can be applicable to different environmental conditions other than those of this experiment, because the process has an intrinsic stochasticity. Additionally, the experimental data show that the portion of the inert (dead) biofilm is so small that it could be neglected at least in small time period simulations such as 1 day. In this work the inert biofilm was neglected for the numerical modeling.

Finally it is quite interesting to have a look on an image of a real biofilm under the microscope. Figure (4.24) shows a close-up of a region on the titan plate surface in the flow chamber covered by the biofilm. It is observed that how complex is the morphology and spatial pattern of the real biofilm under the microscope. One can notice an unbelievable similarity between this image and that of the earth vegetation taken by a satellite! It is fascinating that the appearance of the tiny beings world resembles the worlds of large beings, provided that one looks at the former closely and observes the latter from far away. This image has been recorded by our partners in the medical school of Hannover who conducted the experimental part of this work. It should be stressed that the dimension of the region being simulated is much less than the dimension of this image. In fact, one can take just a few tens of microns as the RVE with periodic boundary conditions in its lateral side. Such an RVE represents the real whole domain and all the numerical analyses are confined to that. So, it can be seen that how limited is our capability in simulating the real world of the tiny beings. This holds true for the world of large things as well. Developing efficient multi-scale computational methods can be a solution to analyze a physical phenomenon in different scales and consequently obtain more realistic results.

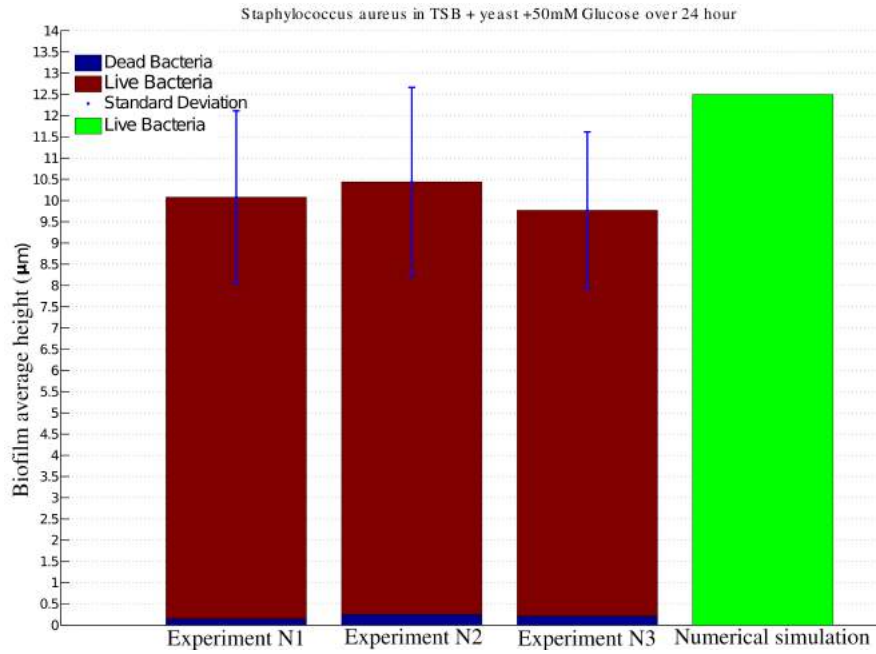


Figure 4.23. Experimental results vs. numerical simulation of the 3D biofilm growth

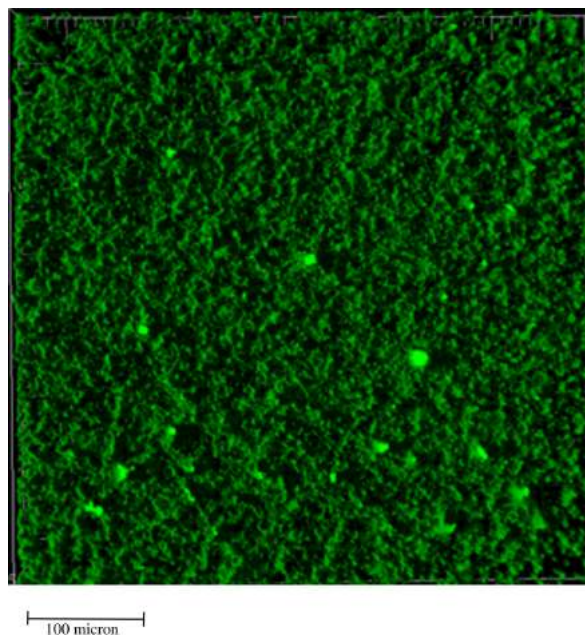


Figure 4.24. A close-up of a real biofilm in the flow chamber under the microscope (by Henryke Rath)

Chapter 5

Conclusions

Biofilm formation is a complex process in the sense that several physical phenomena are involved therein. This makes the problem of the the type so-called "multi-physics". Fluid flow, solid deformation, nutrient transportation, biological growth and erosion are of the most influential phenomena in the biofilm formation. In addition to the physical complexity, there is serious geometrical challenges due to the presence of moving and changing boundaries.

In this thesis, a fully continuum based numerical scheme for the biofilm formation was presented in the SPH framework. The method was motivated by the goal to benefit from the Lagrangian and mesh-less features of SPH in order to handle several complexities in the problem due to the geometrical and physical coupling between the biofilm and the surrounding fluid. Hopefully one can benefit from separation of the different time scales pertaining to the different physical processes, in the sense that establishing a staggered and hierarchical numerical scheme is possible. In other words, all the fast processes are treated within the slow processes in a nested fashion. The biofilm was modeled in small time scales as a deformable solid submerged in the fluid flow. In such a time scale, it experiences mechanical deformations and surface erosion due to the forces from the fluid side. Furthermore, assuming a viscous fluid, biofilm growth was simulated in large time scales while the nutrient transportation was assumed to reach its steady state in each increment of the growth process. The results were verified by the available data in the literature and also the experiments conducted by our partners in the medical school of Hanover. It was found that the hydrodynamical conditions of the fluid flow have a significant impact on how biofilm grows and its geometry changes. Moreover, the numerical simulation of the growth process was in a good agreement with the experimental observations. The authors believe that the developed computational tool is novel and robust. The novelty is due to the fact that utilizing the SPH method is quite new in the field of biofilm modeling to the best of author's knowledge. Besides, its robustness originates from the fact that it is a continuum based method and hence it does not suffer from stochasticity inherent to the individual (particle) based methods. Nevertheless, it enjoys the mesh-less and Lagrangian features which are two advantages for the particle based methods.

In summary, the capabilities of the developed code in this thesis are highlighted as follows:

- 2D and 3D simulation of the biofilm deformation using a hypo-elastic approach in the presence of the surrounding fluid in the context of fluid-solid interaction.

- 2D and 3D simulation of the biofilm growth in the frame work of continuum growth theory and also nutrient transportation.
- 2D and 3D simulation of the surface erosion in the biofilm which accounts for the material removal from the biofilm at the fluid-biofilm interface.

Biofilm world is still of virgin ones with lots of unanswered questions. One can say that all the researches in this area are still in their infancy. In the framework of this work, there are some possible extensions in order to incorporate other aspects and determinant factors of the biofilm formation. Here some directions for further future researches are suggested by the authors:

- To consider a multi-species colony of bacteria.
- To incorporate the shrinkage of biofilm due to bacteria decay in the long term. This is a phenomenon exactly in an opposite direction of the growth process.
- To model other detachment processes such as sloughing by means of either introducing a new field variable for damage or handling directly the crack propagation.
- To develop a hierarchical multi-scale method for bridging the erosion at a short time scale and the total detachment rate in long term.
- To introduce different non-linearity in the material behavior so that the constitutive equations of the biofilm be close to the real material response.
- To analyze the fluid flow assuming a turbulent regime around the biofilm.
- To investigate the effect of fluid induced movement in the biofilm on the nutrient transportation and up-take rate.
- To benefit from the GPU implementation and more efficient parallelization concepts like MPI instead of existing OpenMP implementation.

Bibliography

- ADAMI S., HU X. & ADAMS N. A generalized wall boundary condition for smoothed particle hydrodynamics. *Journal of Computational Physics*, 231 (2012) (21): 7057 – 7075.
- ALPKVIST E. & KLAPPER I. Description of mechanical response including detachment using a novel particle model of biofilm/flow interaction. *Water Science and Technology*, 55 (2007) (8-9): 265 – 273.
- ALPKVISTA E. & KLAPPER I. A multidimensional multispecies continuum model for heterogeneous biofilm development. *Bulletin of Mathematical Biology*, 69 (2007) (2): 765 – 789.
- AMBROSI D., ATESHIAN G., ARRUDA E., COWIN S. ET AL. Perspectives on biological growth and remodeling. *Journal of the Mechanics and Physics of Solids*, 59 (2011) (4): 863 – 883.
- ANTOCI C., GALLATI M. & SIBILLA S. Numerical simulation of fluidstructure interaction by sph. *Computers and Structures*, 85 (2007) (1114): 879 – 890.
- ARISTODEMO F., FEDERICO I., VELTRI P. & PANIZZO A. Two-phase sph modelling of advective diffusion processes. *Environmental Fluid Mechanics*, 10 (2010) (4): 451 – 470.
- ARISTODEMO F., MARRONE S. & FEDERICO I. Sph modelling of plane jets into water bodies through an inflow/outflow algorithm. *Ocean Engineering*, 105 (2015): 160 – 175.
- BALSARA D.S. von neumann stability analysis of smoothed particle hydrodynamicssuggestions for optimal algorithms. *Journal of Computational Physics*, 121 (1995) (2): 357 – 372.
- BAZILEVS Y., CALO V.M., HUGHES T.J.R. & ZHANG Y. Isogeometric fluid-structure interaction: theory, algorithms, and computations. *Computational Mechanics*, 43 (2008) (1): 3 – 37.
- BEISSEL S. & BELYTSCHKO T. Nodal integration of the element-free galerkin method. *Computer Methods in Applied Mechanics and Engineering*, 139 (1996) (14): 49 – 74.

- BELYTSCHKO T. Methods and programs for analysis of fluid-structure systems. *Nuclear Engineering and Design*, 42 (1977) (1): 41 – 52.
- BELYTSCHKO T., BAANT Z.P., YUL-WOONG H. & TA-PENG C. Strain-softening materials and finite-element solutions. *Computers and Structures*, 23 (1986) (2): 163 – 180.
- BELYTSCHKO T., GUO Y., KAM LIU W. & PING XIAO S. A unified stability analysis of meshless particle methods. *International Journal for Numerical Methods in Engineering*, 48 (2000) (9): 1359 – 1400.
- BELYTSCHKO T., KRONGAUZ Y., DOLBOW J. & GERLACH C. On the completeness of meshfree particle methods. *International Journal for Numerical Methods in Engineering*, 43 (1998) (5): 785 – 819.
- BELYTSCHKO T., LIU W.K., MORAN B. & ELKHODARY K. *Nonlinear finite element for continua and structures*. John Wiley and Sons, 2002.
- BENZ W. *The Numerical Modelling of Nonlinear Stellar Pulsations: Problems and Prospects*, chapter Smooth Particle Hydrodynamics: A Review, pages 269 – 288. Springer Netherlands, Dordrecht, 1990.
- BERNSTEIN B. Hypo-elasticity and elasticity. *Archive for Rational Mechanics and Analysis*, 6 (1960): 89 – 104.
- BOFFIN H.M.J. & ANZER U. Numerical studies of wind accretion using SPH. 1: 2D simulations. *Astronomy and Astrophysics*, 284 (1994): 1026–1036.
- BÖL M., MHLE R.B., HAESNER M., NEU T.R. ET AL. 3d finite element model of biofilm detachment using real biofilm structures from clsm data. *Biotechnology and Bioengineering*, 103 (2009) (1): 177 – 186.
- BONET J. Variational and momentum preservation aspects of Smooth Particle Hydrodynamic formulations. *Computer Methods in Applied Mechanics and Engineering*, 180 (1999): 97–115.
- BOYLE J. Structure and function of biofilms edited by w. g. characklis and p. a. wilderer. *Journal of Chemical Technology and Biotechnology*, 50 (1991) (3): 436 – 436.
- VAN BRUMMELEN E., HULSHOFF S. & DE BORST R. Energy conservation under incompressibility for fluidstructure interaction problems. *Computer Methods in Applied Mechanics and Engineering*, 192 (2003) (25): 2727 – 2748.
- BRYERS J. *Physiological models in microbiology*, chapter Modeling biofilm accumulation, pages 109 – 144. CRC Press, Boca Raton, FL, 1988.
- CAUSIN P., GERBEAU J. & NOBILE F. Added-mass effect in the design of partitioned algorithms for fluidstructure problems. *Computer Methods in Applied Mechanics and Engineering*, 194 (2005) (4244): 4506 – 4527.

- CHARACKLIS W., MCFETERS G. & MARSHALL K. *Biofilms*, chapter Physiological ecology of biofilm systems, pages 341 – 393. Wiley-Interscience, New York, 1999a.
- CHARACKLIS W., MCFETERS G. & MARSHALL K. *Biofilms*, chapter Transfer and interfacial transport phenomena, pages 265 – 340. Wiley-Interscience, New York, 1999b.
- CHEN K.J., BERAUN E.J. & JIH J.C. An improvement for tensile instability in smoothed particle hydrodynamics. *Computational Mechanics*, 23 (1999) (4): 279 – 287.
- CHEN Y.C. & HOGER A. *Advances in Continuum Mechanics and Thermodynamics of Material Behavior: In Recognition of the 60th Birthday of Roger L. Fosdick*, chapter Constitutive Functions of Elastic Materials in Finite Growth and Deformation, pages 175 – 193. Springer Netherlands, Dordrecht, 2000.
- CHOPP L.D., KIRISITS J.M., MORAN B. & PARSEK R.M. A mathematical model of quorum sensing in a growing bacterial biofilm. *Journal of Industrial Microbiology and Biotechnology*, 29 (2002) (6): 339 – 346.
- CLEARY P.W. & MONAGHAN J.J. Conduction modelling using smoothed particle hydrodynamics. *Journal of Computational Physics*, 148 (1999) (1): 227 – 264.
- COGAN N.G. Two-fluid model of biofilm disinfection. *Bulletin of Mathematical Biology*, 70 (2007) (3): 800 – 819.
- COGHLAN A. Slime city. *New Scientists*, 2045 (1996): 32–36.
- CUMSILLE P., ASENJO J.A. & CONCA C. A novel model for biofilm growth and its resolution by using the hybrid immersed interface-level set method. *Computers and Mathematics with Applications*, 67 (2014) (1): 34 – 51.
- DALRYMPLE R.A. & KNIO O. *SPH Modelling of Water Waves*, chapter 79, pages 779–787.
- DIEHL S., ROCKEFELLER G.M. & FRYER C.L. Generating optimal initial conditions for smooth particle hydrodynamics simulations. *Monthly Notices of the Royal Astronomical Society*, (2008).
- DILLON R., FAUCI L., FOGELSON A. & III D.G. Modeling biofilm processes using the immersed boundary method. *Journal of Computational Physics*, 129 (1996) (1): 57 – 73.
- DOCKERY J. & KLAPPER I. Finger formation in biofilm layers. *SIAM J. Appl. Math*, 62 (2001): 853 – 869.
- DONLAN R.M. Biofilms: Microbiolife on surfaces. *emerging infectious diseases*, 8 (2002) (9): 881–890.
- DUDDU R., BORDAS S., CHOPP D. & MORAN B. A combined extended finite element and level set method for biofilm growth. *International Journal for Numerical Methods in Engineering*, 74 (2008) (5): 848 – 870.

- DUDDU R., CHOPP D.L. & MORAN B. A two-dimensional continuum model of biofilm growth incorporating fluid flow and shear stress based detachment. *Biotechnology and Bioengineering*, 103 (2009) (1): 92 – 104.
- DUNNE W.M. Bacterial adhesion: Seen any good biofilms lately? *Clinical Microbiology Reviews*, 15 (2002) (2): 155–166.
- DYKA C. & INGEL R. An approach for tension instability in smoothed particle hydrodynamics (sph). *Computers and Structures*, 57 (1995) (4): 573 – 580.
- EBERL H., PICIOREANU C., HEIJNEN J. & VAN LOOSDRECHT M. A three-dimensional numerical study on the correlation of spatial structure, hydrodynamic conditions, and mass transfer and conversion in biofilms. *Chemical Engineering Science*, 55 (2000) (24): 6209 – 6222.
- EBERL H.J., PARKER D.F. & VAN LOOSDRECHT M.C. A new deterministic spatio-temporal continuum model for biofilm development. *Journal of Theoretical Medicine*, 3 (2001) (3): 161–175.
- EPSTEIN M. & MAUGIN G.A. Thermomechanics of volumetric growth in uniform bodies. *International Journal of Plasticity*, 16 (2000) (78): 951 – 978.
- FATEHI R. & MANZARI M. Error estimation in smoothed particle hydrodynamics and a new scheme for second derivatives. *Computers and Mathematics with Applications*, 61 (2011) (2): 482 – 498.
- FELDMAN J. *Dynamic refinement and boundary contact forces in Smoothed Particle Hydrodynamics with applications in fluid flow problems*. Ph.D. thesis, University of Wales Swansea (2006).
- FELIPPA C.A., PARK K. & FARHAT C. Partitioned analysis of coupled mechanical systems. *Computer Methods in Applied Mechanics and Engineering*, 190 (2001) (2425): 3247 – 3270.
- FLEMMING H.C., WINGENDER J., GRIEBE T. & MAYER C. Physico-chemical properties of biofilms. *Biofilms: Recent Advances in Their Study and Control*, (2000): 19 – 34.
- FLETCHER M. & LOEB G.I. Influence of substratum characteristics on the attachment of a marine pseudomonad to solid surfaces. *Applied and Environmental Microbiology*, 37 (1979) (1): 67–72.
- FLORA J.R.V., SUIDAN M.T., BISWAS P. & SAYLES G.D. modeling substrate transport into biofilms, role of multiple ions and ph effects. *Journal of Environmental Engineering*, 119 (1993) (5): 908 – 930.
- FUJIKAWA H. & MATSUSHITA M. Fractal growth of bacillus subtilis on agar plates. *Journal of the Physical Society of Japan*, 58 (1989) (11): 3875–3878.

- GANZENMLLER G.C. An hourglass control algorithm for lagrangian smooth particle hydrodynamics. *Computer Methods in Applied Mechanics and Engineering*, 286 (2015): 87 – 106.
- GARRETT T.R., BHAKOO M. & ZHANG Z. Bacterial adhesion and biofilms on surfaces. *Progress in Natural Science*, 18 (2008) (9): 1049 – 1056.
- GERABEK E.W. The tooth-worm: historical aspects of a popular medical belief. *Clinical Oral Investigations*, 3 (1999) (1): 1 – 6.
- GESTEIRA M., ROGERS B., DALRYMPLE R., CRESPO A. ET AL. *User guide for the SPHysics code*. SPHysics (2010).
- GINGOLD R.A. & MONAGHAN J.J. Smoothed particle hydrodynamics: theory and application to non-spherical stars. *Monthly Notices of the Royal Astronomical Society*, 181 (1977) (3): 375–389.
- GOMEZ-GESTEIRA M., ROGERS B.D., DALRYMPLE R.A. & CRESPO A.J. State-of-the-art of classical sph for free-surface flows. *Journal of Hydraulic Research*, 48 (2010) (sup1): 6–27.
- GORIELY A., ROBERTSON-TESSI M., TABOR M. & VANDIVER R. *Mathematical Modelling of Biosystems*, chapter Elastic Growth Models, pages 1 – 44. Springer Berlin Heidelberg, Berlin, Heidelberg, 2008.
- GRAY J. SPH elastic dynamics. *Computer Methods in Applied Mechanics and Engineering*, 190 (2001): 6641–6662.
- HAUSER M. & VAFAI K. Analysis of the multidimensional effects in biofilms. *International Journal of Heat and Mass Transfer*, 56 (2013) (12): 340 – 349.
- HERMANN S. *Parallel Programming in Fortran 95 using OpenMP*, pages 1 – 75. OpenMP.org 2002, 2002.
- HERMANSSON M. The dlvo theory in microbial adhesion. *Colloids and Surfaces B: Biointerfaces*, 14 (1999) (14): 105 – 119.
- HILL R. Some basic principles in the mechanics of solids without a natural time. *Journal of the Mechanics and Physics of Solids*, 7 (1959) (3): 209 – 225.
- HIMPEL G., KUHL E., MENZEL A. & STEINMANN P. Computational modelling of isotropic multiplicative growth. *Computer Modeling in Engineering and Sciences*, 4 (2005) (2): 119 – 134.
- HOLZAPFEL G.A. *Nonlinear Solid Mechanics: A Continuum Approach for Enineering*. john wiley and sons, 2000.
- HORN H., REIFF H. & MORGENROTH E. Simulation of growth and detachment in biofilm systems under defined hydrodynamic conditions. *Biotechnology and Bioengineering*, 81 (2003) (5): 607 – 617.

- HOŠTACKÁ A., ČIŽNÁR I. & ŠTEFKOVIČOVÁ M. Temperature and ph affect the production of bacterial biofilm. *Folia Microbiologica*, 55 (2010) (1): 75 – 78.
- HUGHES T.J., LIU W.K. & ZIMMERMANN T.K. Lagrangian-eulerian finite element formulation for incompressible viscous flows. *Computer Methods in Applied Mechanics and Engineering*, 29 (1981) (3): 329 – 349.
- JONES G.W. & CHAPMAN S.J. Modeling growth in biological materials. *SIAM Review*, 54 (2012) (1): 52–118.
- KIM H.G. A comparative study of hyperelastic and hypoelastic material models with constant elastic moduli for large deformation problems. *Acta Mechanica*, (2016): 1 – 12.
- KLAPPER I. & DOCKERY J. Mathematical description of microbial biofilms. *SIAM Review*, 52 (2010) (2): 221–265.
- KOLENBRANDER P.E. Oral microbial communities: Biofilms, interactions, and genetic systems. *Annual Review of Microbiology*, 54 (2000) (1): 413–437.
- KREFT J.U. Conflicts of interest in biofilms. *Biofilms*, 1 (2004): 265 – 276.
- KREFT J.U., BOOTH G. & WIMPENNY J.W.T. Bacsim, a simulator for individual-based modelling of bacterial colony growth. *Microbiology*, 144 (1998) (12): 3275–3287.
- KREFT J.U., PICIOREANU C., WIMPENNY J.W.T. & VAN LOOSDRECHT M.C.M. Individual-based modelling of biofilms. *Microbiology*, 147 (2001) (11): 2897–2912.
- KRIŠTOF P., BENEŠ B., KŘIVÁNEK J. & ŠT'AVA O. Hydraulic erosion using smoothed particle hydrodynamics. *Computer Graphics Forum*, 28 (2009) (2): 219 – 228.
- KROON W., DELHAAS T., ARTS T. & BOVENDEERD P. Computational modeling of volumetric soft tissue growth: application to the cardiac left ventricle. *Biomechanics and Modeling in Mechanobiology*, 8 (2008) (4): 301 – 309.
- KUHL E. & HOLZAPFEL G.A. A continuum model for remodeling in living structures. *Journal of Materials Science*, 42 (2007) (21): 8811 – 8823.
- LARDON L.A., MERKEY B.V., MARTINS S., DTSCH A. ET AL. idynamics: next-generation individual-based modelling of biofilms. *Environmental Microbiology*, 13 (2011) (9): 2416 – 2434.
- LATTANZIO J.C., MONAGHAN J.J., PONGRACIC H. & SCHWARZ M.P. Controlling penetration. *SIAM Journal on Scientific and Statistical Computing*, 7 (1986) (2): 591–598.
- LEIMKUHNER B.J., REICH S. & SKEEL R.D. *Mathematical Approaches to Biomolecular Structure and Dynamics*, chapter Integration Methods for Molecular Dynamics, pages 161 – 185. Springer New York, New York, NY, 1996.
- LI S. & LIU W.K. Meshfree and particle methods and their applications. *Applied Mechanics Reviews*, 55 (2002) (1): 1 – 34.

- LIBERSKY L.D., PETSCHKE A.G., CARNEY T.C., HIPPI J.R. ET AL. High strain lagrangian hydrodynamics. *Journal of Computational Physics*, 109 (1993) (1): 67 – 75.
- LIU G.R. *Mesh Free methods: Moving beyond the finite element method*, chapter Mesh free method for engineering problems, pages 25 – 43. CRC press, 2003.
- LIU G.R. & LIU M.B. *Smoothed Particle Hydrodynamics: a meshfree particle method*, chapter introduction, pages 1 – 32. World Scientific Publishing, 2003.
- LIU M.B. & LIU G.R. Smoothed particle hydrodynamics (sph): an overview and recent developments. *Archives of Computational Methods in Engineering*, 17 (2010) (1): 25 – 76.
- LOMBARDI J.C., SILLS A., RASIO F.A. & SHAPIRO S.L. Tests of spurious transport in smoothed particle hydrodynamics. *Journal of Computational Physics*, 152 (1999) (2): 687 – 735.
- LUCY L.B. A numerical approach to the testing of the fission hypothesis. *Astronomical Journal*, 82 (1977): 1013 – 1024.
- MARSHALL K.C., STOUT R. & MITCHELL R. Mechanism of the initial events in the sorption of marine bacteria to surfaces. *Microbiology*, 68 (1971) (3): 337–348.
- MONAGHAN J. On the problem of penetration in particle methods. *Journal of Computational Physics*, 82 (1989) (1): 1 – 15.
- MONAGHAN J. Simulating free surface flows with sph. *Journal of Computational Physics*, 110 (1994) (2): 399 – 406.
- MONAGHAN J. Sph without a tensile instability. *Journal of Computational Physics*, 159 (2000) (2): 290 – 311.
- MONAGHAN J. Smoothed particle hydrodynamics. *Reports on Progress in Physics*, 68 (2005): 1703–1759.
- MONAGHAN J. & GINGOLD R. Shock simulation by the particle method sph. *Journal of Computational Physics*, 52 (1983) (2): 374 – 389.
- MONAGHAN J. & KAJTAR J. Sph particle boundary forces for arbitrary boundaries. *Computer Physics Communications*, 180 (2009) (10): 1811 – 1820.
- MONAGHAN J. & PONGRACIC H. Artificial viscosity for particle methods. *Applied Numerical Mathematics*, 1 (1985) (3): 187 – 194.
- MONAGHAN J.J. Why particle methods work. *SIAM Journal on Scientific and Statistical Computing*, 3 (1982) (4): 422–433.
- MONAGHAN J.J. & LATTANZIO J.C. A refined particle method for astrophysical problems. *Astronomy and Astrophysics*, 149 (1985): 135–143.

- MORRIS J.P. A study of the stability properties of smooth particle hydrodynamics. *Publications Astronomical Society of Australia*, 13 (1996): 97–102.
- MORRIS J.P., FOX P.J. & ZHU Y. Modeling low reynolds number incompressible flows using sph. *Journal of Computational Physics*, 136 (1997) (1): 214 – 226.
- NEWBRUN E. Sugar and dental caries: a review of human studies. *Science*, 217 (1982) (4558): 418 – 423.
- NOGUERA D.R., PIZARFO G., STAHL D.A. & RITTMANN B.E. Simulation of multispecies biofilm development in three dimensions. *Water Science and Technology*, 39 (1999) (7): 123 – 130.
- NOLL W. On the conlinuily of the solid and fluid states. *journal of rational mechanics and analysis*, 4 (1955): 3 – 81.
- O'TOOLE G., KAPLAN H.B. & KOLTER R. Biofilm formation as microbial development. *Annual Review of Microbiology*, 54 (2000) (1): 49 – 79.
- PALMER J., FLINT S. & BROOKS J. Bacterial cell attachment, the beginning of a biofilm. *Journal of Industrial Microbiology and Biotechnology*, 34 (2007) (9): 577 – 588.
- PALMER R.J. & WHITE D.C. Developmental biology of biofilms: implications for treatment and control. *Trends in Microbiology*, 5 (1997) (11): 435 – 440.
- PERCIVAL S.L., MALIC S., CRUZ H. & WILLIAMS D.W. *Biofilms and Veterinary Medicine*, chapter Introduction to Biofilms, pages 41 – 68. Springer Berlin Heidelberg, Berlin, Heidelberg, 2011.
- PICIOREANU C., KREFT J.U. & VAN LOOSDRECHT M.C.M. Particle-Based Multidimensional Multispecies Biofilm Model. *Appl. Environ. Microbiol.*, 70 (2004a) (5): 3024 – 3040.
- PICIOREANU C., KREFT J.U. & VAN LOOSDRECHT M.C.M. Particle-based multidimensional multispecies biofilm model. *Applied and Environmental Microbiology*, 70 (2004b) (5): 3024–3040.
- PICIOREANU C., VAN LOOSDRECHT M. & HEIJNEN J. Discrete-differential modelling of biofilm structure. *Water Science and Technology*, 39 (1999) (7): 115 – 122.
- PICIOREANU C., VAN LOOSDRECHT M.C.M. & HEIJNEN J.J. A new combined differential-discrete cellular automaton approach for biofilm modeling: Application for growth in gel beads. *Biotechnology and Bioengineering*, 57 (1998) (6): 718 – 731.
- PICIOREANU C., VAN LOOSDRECHT M.C.M. & HEIJNEN J.J. Two-dimensional model of biofilm detachment caused by internal stress from liquid flow. *Biotechnology and Bioengineering*, 72 (2001a) (2): 205 – 218.

- PICIOREANU C., VAN LOOSDRECHT M.C.M. & HEIJNEN J.J. Two-dimensional model of biofilm detachment caused by internal stress from liquid flow. *Biotechnology and Bioengineering*, 72 (2001b) (2): 205 – 218.
- PICIOREANU C., VAN LOOSDRECHT M.C.M. & HEIJNEN J.J. Effect of diffusive and convective substrate transport on biofilm structure formation: A two-dimensional modeling study. *Biotechnology and Bioengineering*, 69 (2000) (5): 504 – 515.
- PIPERNO S. & FARHAT C. Partitioned procedures for the transient solution of coupled aeroelastic problems part ii: energy transfer analysis and three-dimensional applications. *Computer Methods in Applied Mechanics and Engineering*, 190 (2001) (2425): 3147 – 3170.
- PIPERNO S., FARHAT C. & LARROUTUROU B. Partitioned procedures for the transient solution of coupled aeroelastic problems part i: Model problem, theory and two-dimensional application. *Computer Methods in Applied Mechanics and Engineering*, 124 (1995) (12): 79 – 112.
- PIZARRO G., GRIFFEATH D. & NOGUERA D. Quantitative cellular automaton model for biofilms. *Journal of Environmental Engineering*, 127 (2001) (9): 782–789.
- PRICE D.J. Smoothed Particle Hydrodynamics: Things I Wish My Mother Taught Me. In CAPUZZO-DOLCETTA R., LIMONGI M. & TORNAMBÈ A., eds., *Advances in Computational Astrophysics: Methods, Tools, and Outcome*, volume 453 of *Astronomical Society of the Pacific Conference Series*, page 249. 2012.
- PRINGLE J.H. & FLETCHER M. Influence of substratum wettability on attachment of freshwater bacteria to solid surfaces. *Applied and Environmental Microbiology*, 45 (1983) (3): 811–817.
- RANDLES P. & LIBERSKY L. Smoothed particle hydrodynamics: Some recent improvements and applications. *Computer Methods in Applied Mechanics and Engineering*, 139 (1996) (14): 375 – 408.
- RANDLES P.W. & LIBERSKY L.D. Normalized sph with stress points. *International Journal for Numerical Methods in Engineering*, 48 (2000) (10): 1445 – 1462.
- RITTMANN B.E. & MCCARTY P.L. Model of steady-state-biofilm kinetics. *Biotechnology and Bioengineering*, 24 (1982) (10): 2291 – 2291.
- RODRIGUEZ E.K., HOGER A. & MCCULLOCH A.D. Stress-dependent finite growth in soft elastic tissues. *Journal of Biomechanics*, 27 (1994) (4): 455 – 467.
- ROSAN B. & LAMONT R.J. Dental plaque formation. *Microbes and Infection*, 2 (2000) (13): 1599 – 1607.
- SIMO J. & PISTER K. Remarks on rate constitutive equations for finite deformation problems: computational implications. *Computer Methods in Applied Mechanics and Engineering*, 46 (1984) (2): 201 – 215.

- STEWART P.S. Mini-review: Convection around biofilms. *Biofouling*, 28 (2012) (2): 187–198.
- STOODLEY P., LEWANDOWSKI Z., BOYLE J.D. & LAPPIN-SCOTT H.M. Oscillation characteristics of biofilm streamers in turbulent flowing water as related to drag and pressure drop. *Biotechnology and Bioengineering*, 57 (1998) (5): 536 – 544.
- STOODLEY P., LEWANDOWSKI Z., BOYLE J.D. & LAPPIN-SCOTT H.M. Structural deformation of bacterial biofilms caused by short-term fluctuations in fluid shear: An in situ investigation of biofilm rheology. *Biotechnology and Bioengineering*, 65 (1999) (1): 83 – 92.
- SWEGLE J., HICKS D. & ATTAWAY S. Smoothed particle hydrodynamics stability analysis. *Journal of Computational Physics*, 116 (1995) (1): 123 – 134.
- TABER L.A. A model for aortic growth based on fluid shear and fiber stresses. *Journal of Biomechanical Engineering*, 120 (1998) (3): 348 – 354.
- TAHERZADEH D., PICIOREANU C., KTTLER U., SIMONE A. ET AL. Computational study of the drag and oscillatory movement of biofilm streamers in fast flows. *Biotechnology and Bioengineering*, 105 (2010) (3): 600 – 610.
- TANG Y. & VALOCCHI A.J. An improved cellular automaton method to model multispecies biofilms. *Water Research*, 47 (2013) (15): 5729 – 5742.
- TARTAKOVSKY A.M., MEAKIN P., SCHEIBE T.D. & WEST R.M.E. Simulations of reactive transport and precipitation with smoothed particle hydrodynamics. *Journal of Computational Physics*, 222 (2007) (2): 654 – 672.
- TRUESDELL C. Hypo-elasticity. *Journal of Rational Mech*, 4 (1955): 83 – 133.
- TRUESDELL C. Remarks on hypo-elasticity. *Journal of Research of the National Bureau of Standards -B Mathematics and Mathematical Physics*, 67 (1963) (3): 141 – 143.
- VACONDIO R., ROGERS B., STANSBY P., MIGNOSA P. ET AL. Variable resolution for sph: A dynamic particle coalescing and splitting scheme. *Computer Methods in Applied Mechanics and Engineering*, 256 (2013): 132 – 148.
- VALIZADEH A. & MONAGHAN J.J. A study of solid wall models for weakly compressible sph. *Journal of Computational Physics*, 300 (2015): 5 – 19.
- VAUGHAN G.L., HEALY T.R., BRYAN K.R., SNEYD A.D. ET AL. Completeness, conservation and error in sph for fluids. *International Journal for Numerical Methods in Fluids*, 56 (2008) (1): 37 – 62.
- VIGNJEVIC R. & CAMPBELL J. *Predictive Modeling of Dynamic Processes: A Tribute to Professor Klaus Thoma*, chapter Review of Development of the Smooth Particle Hydrodynamics (SPH) Method, pages 367 – 396. Springer US, Boston, MA, 2009.

- VIGNJEVIC R., CAMPBELL J. & LIBERSKY L. A treatment of zero-energy modes in the smoothed particle hydrodynamics method. *Computer Methods in Applied Mechanics and Engineering*, 184 (2000) (1): 67 – 85.
- VOLOKH K. Stresses in growing soft tissues. *Acta Biomaterialia*, 2 (2006) (5): 493 – 504.
- WANG Q. & ZHANG T. Review of mathematical models for biofilms. *Solid State Communications*, 150 (2010) (2122): 1009 – 1022.
- WANNER O. & GUJER W. A multispecies biofilm model. *Biotechnology and Bioengineering*, 28 (1986) (3): 314 – 328.
- WATERS C.M. & BASSLER B.L. Quorum sensing: Cell-to-cell communication in bacteria. *Annual Review of Cell and Developmental Biology*, 21 (2005) (1): 319–346.
- WEN Y., HICKS D. & SWEGLE J. *Stabilizing SPH with conservative smoothing*. Sandia National Labs, 1994.
- WILLIAMSON K. & MCCARTY P.L. A model of substrate utilization by bacterial films. *Journal of Water Pollution Control Federation*, 48 (1976) (1): 9–24.
- WRIGGERS P. *Nonlinear Finite Element Methods*. Springer, 2008.
- XAVIER J.D.B., PICIOREANU C. & VAN LOOSDRECHT M.C. A general description of detachment for multidimensional modelling of biofilms. *Biotechnology and Bioengineering*, 91 (2005) (6): 651 – 669.
- XU Z., MEAKIN P., TARTAKOVSKY A. & SCHEIBE T.D. Dissipative-particle-dynamics model of biofilm growth. *Phys. Rev. E*, 83 (2011): 0667 021 – 29.
- YU Q. & FISH J. Multiscale asymptotic homogenization for multiphysics problems with multiple spatial and temporal scales: a coupled thermo-viscoelastic example problem. *International Journal of Solids and Structures*, 39 (2002) (26): 6429 – 6452.
- ZHU Y. & FOX P.J. Smoothed particle hydrodynamics model for diffusion through porous media. *Transport in Porous Media*, 43 (2001) (3): 441 – 471.
- ZOHDI T. & WRIGGERS P. *An Introduction to Computational Micromechanics*. Springer, 2005.

Curriculum vitae

Meisam Soleimani

born December 31, 1984 in Bojnourd, Iran

Professional Experience

since 09.2013

Research assistant at the Institute of Continuum Mechanics,
Leibniz Universität Hannover

Education

10.2007 - 03.2010

University of Tehran
Mechanical Engineering
Focus: Solid Mechanics
Degree: M. Sc.

10.2003 - 09.2007

Sharif University of Technology
Mechanical Engineering
Degree: B. Sc.

1999 - 2003

Nemooneh Shahid Beheshti Bojnourd High School,

